

Transformation Strain and Crystallographic Texture in Steels

By
Saurabh Kundu
Darwin College, Cambridge

University of Cambridge
Department of Materials Science and Metallurgy
Pembroke Street, Cambridge CB2 3QZ

*A dissertation submitted for the degree of
Doctor of Philosophy
at the University of Cambridge
March 2007*

None there be, can rehearse the whole tale ...

*To my parents **Mrityunjoy** and **Anima**, wife **Itishree** and son **Rishiraj**.*

Preface

This dissertation is submitted for the degree of Doctor of Philosophy at the University of Cambridge. The work reported herein was carried out under the supervision of Professor H. K. D. H. Bhadeshia in the Department of Materials Science and Metallurgy, University of Cambridge between June 2004 and March 2007.

To the best of my knowledge, this work is original, except where suitable references are made to previous work. Neither this, nor any substantially similar dissertation has been submitted for any degree, diploma or qualification at any other university or institution. This dissertation does not exceed 60,000 words in length.

Publications :

S. Kundu and H. K. D. H. Bhadeshia, Transformation texture in deformed stainless steel, *Scripta Materialia* **55** (2006) 779-781

S. Kundu, K. Hase and H. K. D. H. Bhadeshia, Crystallographic texture of stress-affected bainite, *Proceedings of the Royal Society of London A*, (*submitted*).

Saurabh Kundu

March, 2007

Acknowledgments

I am grateful to the EPSRC, UK and TATA STEEL, India for funding this project. I would also like to thank TATA STEEL for allowing me to take study leave for 3 years.

I would like to express my sincere gratitude to my supervisor, Prof. H. K. D. H. Bhadeshia, for his guidance and encouragement. I am grateful to Prof. A. L. Greer for the provision for laboratory facilities in the department and to Dr. D. Bhattacharjee for his encouragement and laboratory facilities in TATA STEEL.

Support from Mr Kazu Hase, JFE Steel, Japan is gratefully acknowledged – who helped with many experiments on bainite. I would like to express my sincere gratitude to Dr Howard Stone, Dr John Francis and Prof. P. J. Withers for their help with neutron diffraction and synchrotron studies. I am indebted to Dr Arunanshu Halder for his help and encouragement with the experiments conducted at TATA STEEL. I am immensely grateful to ESAB AB (Sweden) for preparing the welding alloys. I would like to express my sincere thanks to Mr Vikram Sharma, for his support with the EBSD work, and to Mr Raju Dasu and Mr Anup Sharma for their help with the FEM analysis. I am also grateful to Mr Kevin Roberts and Mr Brian Whitemore for their help with the experiments in Cambridge.

I have received technical help/suggestions from many other people during the course of this work. I want to specially mention Prof. S. R. Kalidindi, Prof. D. Raabe, Dr N. Gey, Prof. M. Humbert, Mr M. J. Peet, Dr T. Sourmail, Dr A. F. Gourgues and Dr M. Sherif for many helpful discussions.

I am greatly indebted to Darwin College, especially to the dean Dr Leo E. A. Howe, Mrs. S. James, head of accommodation and Mrs. S. Williams, accommodation secretary, for their unfailing support and assistance.

My family has sacrificed the most during my studies but they have always been with me and never lost faith in me. The support I have got from my wife Itishree and son Phomphai during the last three years cannot be expressed in words. My parents, Mrityunjoy and Anima always wanted me to become successful in all my endeavors and it is their blessings that took me this far. I am also grateful to my sister Rumi and brother-in-law Subhendu for their support. The help from my in-laws, Girish Chandra and Manjula Mohanty, has been outstanding and unforgettable.

I have got a lot of encouragement and support from my friends here in Cambridge. I am indebted to Sourabh (Chatterjee) for his friendship and support. I want to specially mention Mathew and Mohamed. I have always enjoyed their company. Many thanks to Stephane and Radu for their friendship, especially to Stephane for giving me the DVDs of “friends”. I would also like to thank Sourav, Subhankar, Richard, Amir, Thomas, Sophie, Audrey, Ueta, Yuko, Ganzalo, Andrew, Kang and Jiawen.

Abstract

The transformation strain associated with displacive phase transformations can be utilised to improve mechanical properties of structural components in steels. The advantages of the transformation plasticity can be fully utilised by allowing the transformation to occur under the influence of external stress or strain. In this thesis, mathematical models have been formulated to calculate the transformation strain and texture during martensitic and bainitic transformations. The models are able to deal with a variety of complexities including various starting austenite textures and different states of externally applied stress.

A variant selection model has been proposed based on Patel and Cohen's theory and the effect of variant selection on the transformation strain and texture has been discussed in detail. A new theory has been proposed to calculate the extent of variant selection. An attempt has been made to separate the effects of stress and strain on transformation plasticity and variant selection. It has been shown that Patel and Cohen's plastic strain theory is more suitable than the elastic infinitesimal strain deformation model to calculate the interaction energies between crystallographic variants and external load.

Using theoretical knowledge and with the help of a neural network model, new alloys have been prepared to be used as the welding filler metals to reduce the residual stress and to achieve higher toughness. Neutron diffraction studies have revealed that newly developed filler metals do indeed reduce the residual stress.

Synchrotron X-ray data have been utilised to determine the texture of austenite and martensite as transformation occurs under load. A mathematical model has been developed to predict the Debye diffraction patterns observed experimentally.

Contents

1	Introduction	1
2	Shape deformation in displacive transformations and properties	4
2.1	Shape deformation	4
2.2	Phenomenological theory of martensite crystallography	7
2.2.1	Definition of a basis	8
2.2.2	Outline of the theory	9
2.2.3	Factorisation of invariant-line strain	13
2.2.4	Other forms of phenomenological theory of martensite crystallography	15
2.3	Stress, strain and transformation texture	16
2.3.1	Texture from strained austenite	16
2.3.2	Comments on variant selection model	20
2.4	Microstructural and kinetics effect	23
2.4.1	Effect of stress	23
2.4.2	Effect of strain	23
2.5	Stress/strain-induced transformation and mechanical properties	29
2.5.1	Residual stress	29
2.5.2	Fatigue	31
2.6	Evolution of martensitic transformation	34

2.6.1	Koistinen-Marburger equation	34
2.6.2	Justification of Koistinen-Marburger equation	35
2.7	Summary	37
3	The transformation strain	39
3.1	Introduction	39
3.2	Crystallography	40
3.3	Variant Selection	42
3.4	Generation of random and bias texture data	44
3.5	Transformation strains	47
3.5.1	Uniaxial stresses	47
3.5.2	Multiaxial Stresses	53
3.6	Comparison with experiments: Transformation Strain	54
3.6.1	Extent of Variant Selection versus Stress	58
3.7	Stress-free Transformation from austenite	59
3.8	Summary	62
4	Transformation texture: Single crystal analysis	64
4.1	Introduction	64
4.2	Orientation relationship between martensite and austenite	65
4.3	Methodology for drawing pole figure	66
4.4	Determination of matrix (S J γ)	67
4.5	Data	68
4.6	Comparison with experiments: Variant selection	69
4.7	Observed variant intensities and relation to interaction energies	76
4.8	Sensitivity to Crystallographic Data	80
4.9	Summary	84
5	Texture of martensite formed from plastically deformed austenite	87

5.1	Introduction	87
5.2	Experimental Procedure	88
5.2.1	Tensile Tests	88
5.2.2	EBSD analysis	90
5.3	Pole figures from single crystals of γ	91
5.3.1	Analysis of “30Ni-Stress”	91
5.3.2	Analysis from alloy “30Ni-Strain”	95
5.4	Texture prediction in a 304 austenitic stainless steel	98
5.5	Texture in rolled steels	101
5.5.1	Modelling the TAR process	105
5.5.2	Modelling the TDR process	108
5.6	Severity of transformation texture	114
5.7	Summary	115
6	Texture and intervening transformations	118
6.1	Introduction	118
6.2	Interaction energy for $\gamma \rightarrow \epsilon$ transformation	119
6.2.1	Patel and Cohen approach	122
6.3	Texture prediction, single γ crystal	125
6.4	Summary	127
7	Alloy design	131
7.1	Introduction	131
7.2	Mechanical properties	132
7.3	Comparison of properties	143
7.4	Restriction on the lowering of M_S temperature	143
7.5	Alloy preparation and properties	146
7.6	Summary	150

8	Interpretation of Debye rings from synchrotron X-rays	154
8.1	Introduction	154
8.2	Generation of diffraction pattern	155
8.3	The Bragg law in reciprocal space	155
8.4	Construction of the model	157
8.5	Experimental procedure	158
8.6	Results and Discussion	161
8.7	Summary	169
9	Conclusions and future work	170
A	Residual stress measurement	173
A.1	Introduction	173
A.2	Experimental details	174
A.2.1	Filler metals	174
A.2.2	Manufacture of the welded plates	175
A.2.3	Neutron diffraction	176
A.2.4	Determination of stress-free lattice spacing	179
A.3	Results	179
A.3.1	Calculations of strains and stresses	179
A.3.2	Results and discussion	180
A.4	Summary and future work	185
B	Computer programs	187
B.1	Subroutine MAP_STEEL_BAIN_STRAIN	187
B.2	Subroutine MAP_STEEL_TRANS_PLAST	191
B.3	Subroutine MAP_STEEL_TEXTURE	195

Chapter 1

Introduction

Displacive transformations in steels such as bainite and martensite generate dilatational and shear strains of about 0.03 and 0.22-0.26 respectively [1]. However, the shear strains associated with the plates of transformed products tend to cancel when the plates are randomly oriented in the overall microstructure. There are ways, for instance using externally applied stress or strain, by which it is possible to bias the microstructure and exploit the full extent of the shear strain in particular technological applications.

Many major engineering failures occur due to fatigue exacerbated by residual stresses introduced during welding. The conventional way of coping with this is to reduce design stresses, conduct heat treatments to relieve residual stresses (although this is not always an option) or to avoid stress concentrations. An alternative approach in the case of steels, which avoids many of the difficulties of the usual methods, is to exploit solid-state phase transformations to control the development of stresses [2, 3]. Here the transformation plasticity during the cooling of weldments might be engineered to compensate for thermal contraction strains in constrained assemblies. To do this most effectively requires the shear strain of the transformation (by far the biggest component of the transformation strain) to be visible on a macroscopic scale. That is, there must be a bias in the microstructure as

described above.

That solid state transformations can be used to reduce weld stresses, has been demonstrated in some simple experiments on weld distortion [4]. Recent work in Japan [2] on similar lines, using welding consumables with very low transformation temperatures has shown that it is possible not only to reduce the residual tensile stresses but to introduce residual compression into the weld region, with consequential enhancement of fatigue life.

The non-random orientation in the microstructure arises due to two major factors, variant selection and the prior orientation of the austenite phase. But it is not clear how these factors influence the transformation strain and texture, which directly influence the material properties. A seminal part of the work presented in this thesis has been dedicated to create mathematical algorithms which can estimate the transformation strain and texture during displacive transformations. Most of the existing models [5–9] tend to ignore the totality of phenomenological theory of martensite crystallography [10, 11], which correctly describes the shape and crystallography of martensitic transformation and resort to unrealistic simplification or introduce undue complications. Many such models can estimate the transformation texture, but not the (anisotropic) strains due to transformation in a polycrystalline substance.

An effort has been made here to strictly comply with the theory of crystallography and the plastic work model of Patel and Cohen [12]. These are the two rigorous tenets of stress-affected transformation theory. There are also some unanswered questions about the exact role stress, as opposed to plastic strain in the austenite, plays during displacive transformations. An attempt has been made to separate out the effects of stress and strain on the transformation. Electron back scattered diffraction has been used in some cases to measure the microtexture, particularly from single crystals of the parent phase in order to validate variant selection criteria. In other cases,

data from the published literature have been exploited.

The external load is responsible for variant selection during displacive transformation, its effect manifesting as mechanical free energy whose magnitude depends on the orientation of the plate. Some plates will in this sense be favourably oriented, *i.e.*, their transformation strains comply with the imposed load. But the extent of variant selection is not explained with any existing theory. A theory has been introduced here to quantitatively express the extent of variant selection.

Synchrotron X-ray sources have also been used to study the orientation bias in the microstructure as a function of applied load.

Using the principles of physical metallurgy and a variety of models, new welding alloys have been designed which are tough and transform at low temperatures to take advantage of the transformation plasticity as a compensating mechanism for thermal strains in welded joints. The idea was to reduce residual stresses. Experimental joints were prepared using the new alloys and the residual stresses were measured using neutron diffraction.

To summarise, original theory has been formulated to deal with the development of texture and macroscopic strains during the course of displacive transformation in steels. This has then been exploited to design certain welding alloys which should have an advantage from the point of view of the mechanical behaviour of large, constrained assemblies fabricated using localised heat sources.

Chapter 2

Shape deformation in displacive transformations and properties

2.1 Shape deformation

An invariant-plane strain (IPS) occurs for example, when a dislocation shears a crystal plane in such a manner that the slip plane remains crystalline with no change in the relative positions of the atoms. A similar deformation occurs when phases like martensite or bainite grow in the form of thin plates. The difference is that the IPS associated with martensite or bainite has a dilatation in addition to the shear component as shown in Fig. 2.1.

The parameters δ , s and m represent the magnitudes of the dilatational strain, shear strain and total displacement respectively. If \mathbf{d} is a unit vector in the direction of the displacements involved, then $m\mathbf{d}$ represents the displacement vector, where m is the magnitude of the displacement. $m\mathbf{d}$ may be factorised as $m\mathbf{d} = s\mathbf{z}_1 + \delta\mathbf{z}_3$. Fig. 2.1c depicts the shape deformation accompanying the formation of martensite or bainite, with $s \simeq 0.22 - 0.26$ and $\delta \simeq 0.03$ [1]. Here \mathbf{z}_1 and \mathbf{z}_3 are unit vectors parallel to the shear component of the deformation and the unit normal to the invariant plane respectively.

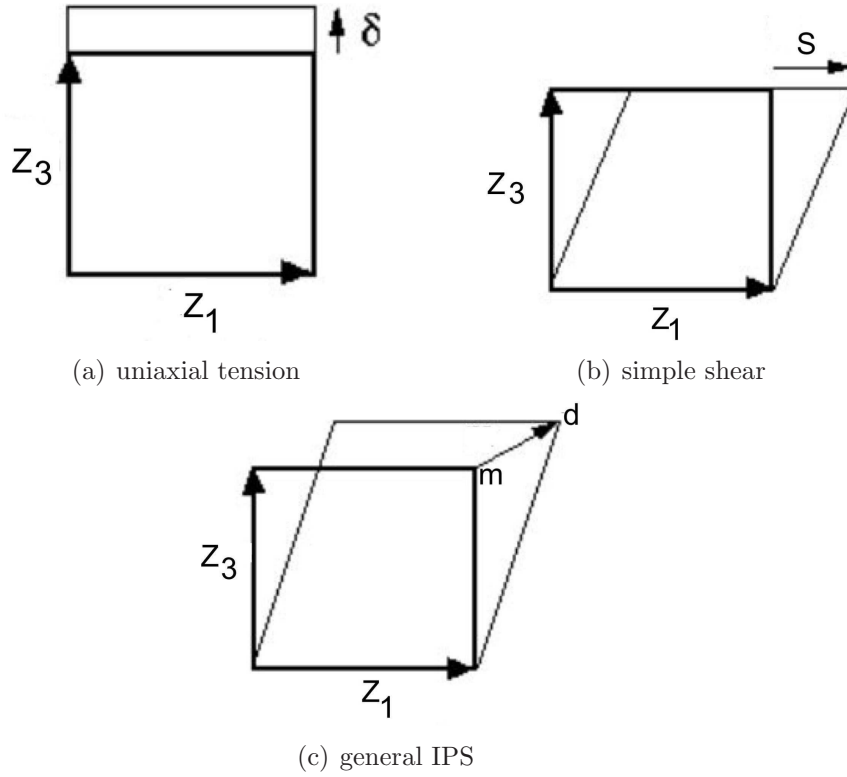


Figure 2.1: Three kinds of invariant plane strain. After Bhadeshia [13].

These deformations are much larger than elastic strains in a tensile test, which are of the order of 10^{-3} . The strains s and δ , therefore, have profound effects on microstructure and properties. The invariant plane is generally known as the habit plane.

As displacive transformations are deformations, externally applied stress will affect their progress [12, 14]. The work done by the external stress may be added to the chemical free energy change accompanying transformation. The mechanical driving force is therefore [12] :

$$\Delta G_{mech} = \sigma_N \delta + \tau s \quad (2.1)$$

where σ_N and τ are the normal and shear stress respectively on the habit plane, and δ and s are the normal and shear strains respectively, due to the

shape deformation (Fig. 2.2) [1].

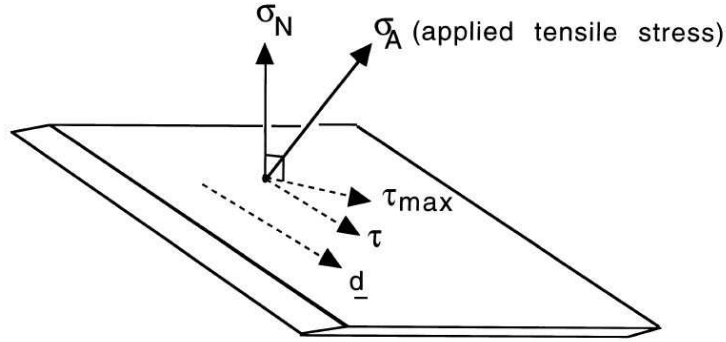


Figure 2.2: Resolution of the applied stress σ_A . The normal stress σ_N , and the shear stress τ , both act on the habit plane. The vector \mathbf{d} is the direction along which the shear displacement of the shape deformation lies. τ_{max} is the maximum shear stress on the habit plane, but τ is given by resolving τ_{max} along \mathbf{d} . Note that \mathbf{d} differs slightly from the displacement vector of the invariant-plane strain, which includes a dilatational component in addition to the shear [1].

There are in general 24 variants of martensite so it is likely that at least one of these variants will be favoured by the resolved shear stress. The term τs should therefore always be positive irrespective of the sign of the uniaxial stress. But the sign of $\sigma_N \delta$ depends on that of σ_N . For α' in steels the shear component is relatively large so a uniaxial stress always gives a positive ΔG_{mech} in a polycrystalline state, thus leading to an increase of the transformation temperature. A hydrostatic stress has no deviatoric component and thus only interacts with the dilatational component of the shape change. In steels, hydrostatic pressure on its own should therefore suppress transformation. Stress affected transformation will also bias the microstructure since certain variants are favoured over others [15, 16]. For example, with a uniaxial stress those variants with habit planes inclined at 45° to the stress axis are favoured. This factor may have practical consequences on the properties and will be discussed latter.

2.2 Phenomenological theory of martensite crystallography

The crystallography of the martensite transformation has been a story of exciting scientific development over the years. First, the austenite (γ) to martensite (α') transformation has been described with the help of Bain strain which on its own is proved to be insufficient to describe the crystallography of transformation and the observed shape change. The phenomenological theory of martensite crystallography (PTMC) [10, 11] resolves the problem. Martensitic transformation is associated with a dilatational and a shear strain. The latter is much bigger in magnitude (0.22) than the former (0.03) but generally gets cancelled on a macroscopic scale when many variants of martensite form.

However it has been observed that if the martensite is formed under the influence of external stress there is a preferred direction along which the plates tend to be aligned. Under this condition the martensite plates are not randomly oriented but a biased microstructure results. Some work has been published on the prediction of martensite pole figures formed with or without the influence of stress [5, 6, 8]. But the work is often based on assumptions which are inconsistent with the crystallographic theory of martensite. In many cases the model has been developed considering only the Bain strain, which is one component of the total deformation [9]. It is often assumed that the orientation relationship between the austenite and martensite is that due to Kurdjumov–Sachs or Nishiyama–Wasserman [17–20], but it has been known for some time that the true relation must be irrational [10, 11, 13, 21]. Although the difference between this irrational and assumed orientation may seem less than a few degrees, it is vital because the assumed orientations do not in general lead to an invariant–line between the parent and product lattices. The existence of an invariant line

is an essential requirement for martensitic transformation to occur. It is not surprising therefore, that Nolze [22] in his experimental study of several hundred thousand γ/α orientation relations, found detailed deviations from assumed Kurdjumov–Sachs *etc.* orientations.

2.2.1 Definition of a basis

The notations used in this thesis are due to Bowles and MacKenzie [10]. Fig. 2.3 shows a unit cell of austenite. To specify the direction and magnitude of a vector, for example \mathbf{u} shown in Fig. 2.3, it is necessary to have a reference set of coordinates. A convenient reference frame can be formed by the three right handed orthogonal vectors \mathbf{a}_1 , \mathbf{a}_2 and \mathbf{a}_3 which lie along the three sides of the unit cell. All these vectors have magnitude a_γ , lattice parameter of austenite. So \mathbf{a}_1 , \mathbf{a}_2 and \mathbf{a}_3 form a orthogonal basis. In the special case when all these vectors are mutually perpendicular and of unit length the basis is called orthonormal. ‘F’ represents a orthonormal basis where as corresponding reciprocal basis is expressed as ‘F*’. Any column vector $\mathbf{d} = [d_1 \ d_2 \ d_3]$ can be represented in a orthonormal basis as $[\mathbf{F}; \mathbf{d}]$ and any row vector $\mathbf{p} = (p_1 \ p_2 \ p_3)$ is expressed as $(\mathbf{p}; \mathbf{F})$.

Any coordinate transformation matrix is represented by a 3×3 matrix, which is written as $(\mathbf{B} \ \mathbf{J} \ \mathbf{A})$. It transforms the components of vectors referred to the A basis to those referred to the B basis. The matrix $(\mathbf{A} \ \mathbf{J} \ \mathbf{B})$ and $(\mathbf{B} \ \mathbf{J}' \ \mathbf{A})$ represent the inverse and transpose of the matrix $(\mathbf{B} \ \mathbf{J} \ \mathbf{A})$ respectively. The determinant of a matrix is represented by : $\det(\text{matrix})$.

Any deformation is represented as a 3×3 matrix, which in the austenite reference frame can be written as $(\mathbf{F} \ \mathbf{S} \ \mathbf{F})$. Deformation matrix does not involve in any change of basis and that’s why the basis symbol is the same (F, in this case) in the both sides of S. Similarly the matrix $(\mathbf{F} \ \mathbf{J} \ \mathbf{F})$ represents rotation. A detailed description of the notations can be obtained from [13].

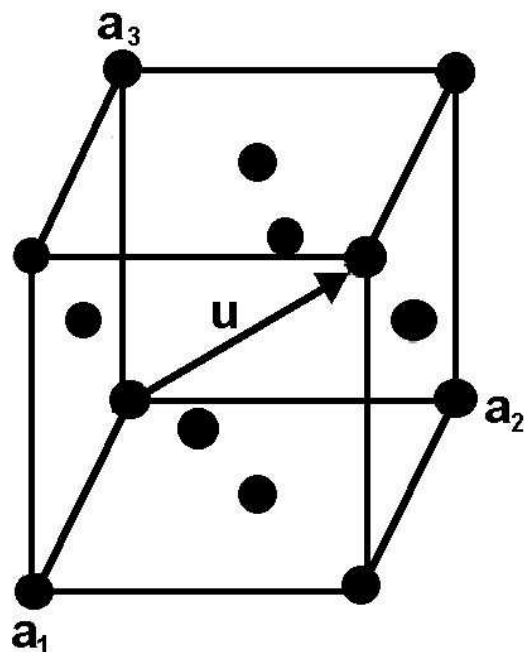


Figure 2.3: An unit cell of face-centred cubic (FCC) crystal.

2.2.2 Outline of the theory

For the α'/γ interface to be glissile, it must as a minimum contain an invariant line. Such a line is one, which is undistorted and unrotated by the invariant-line strain. Fig. 2.4 shows that the austenite unit cell can also be represented as a body-centred tetragonal (BCT) cell lattice. For martensite to be a body-centred cubic unit cell a compression is needed along the \mathbf{b}_3 axis and expansion along \mathbf{b}_1 and \mathbf{b}_2 . This is the Bain strain (F B F). However the Bain strain does not leave any line invariant as demonstrated in Fig. 2.5a,b.

A sphere of austenite is deformed into an ellipsoid by the Bain strain. It can be seen that the lines $a'b'$ and $c'd'$ remain unextended due to the deformation. In fact, the undistorted lines form a right circular cone along \mathbf{a}_3 . However, they are all rotated by an angle θ so they are not invariant. However if a rigid body rotation is now added to the Bain strain, then Fig. 2.5c

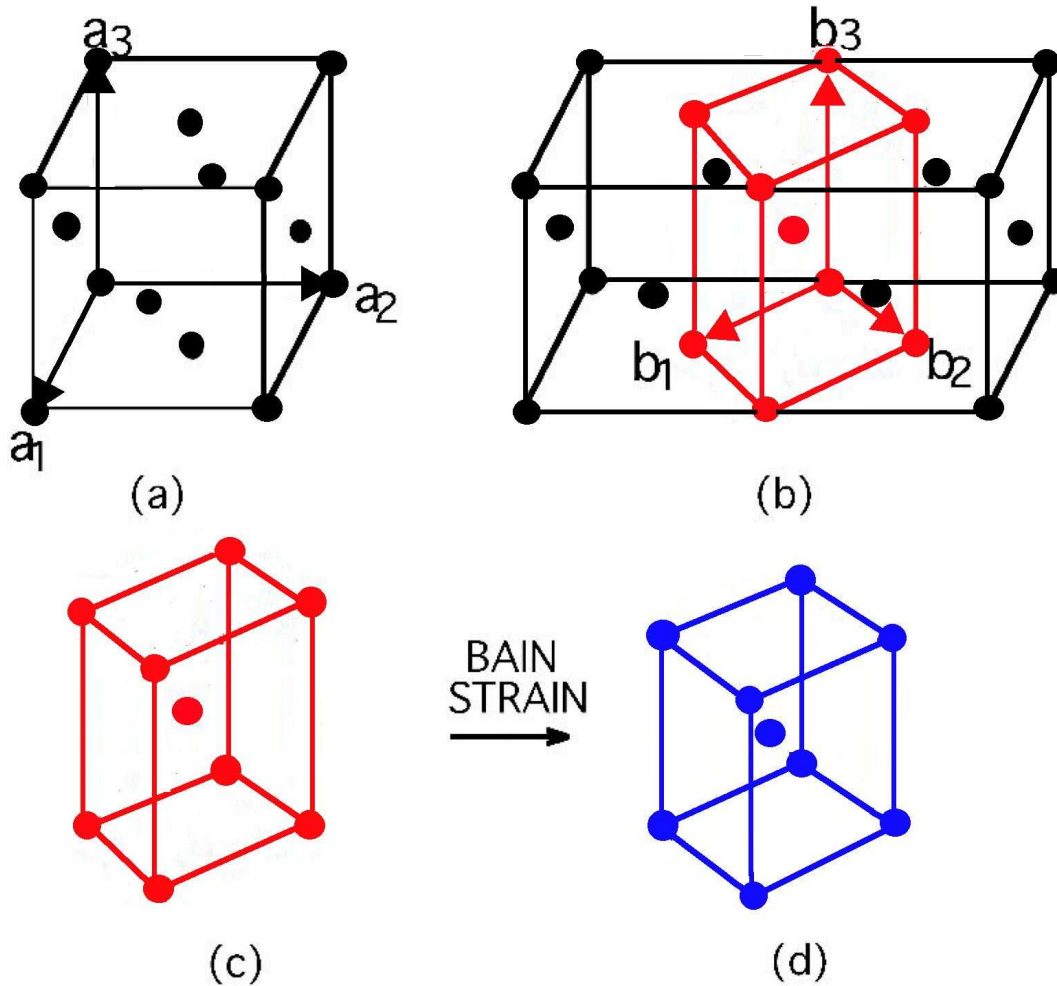


Figure 2.4: (a) FCC unit cell (b) Relations between FCC and BCT (body-centred tetragonal) cells of austenite (c) BCT cell of austenite (d) Deformation due to Bain strain which convert a BCT cell to body-centred cubic (BCC) cell.

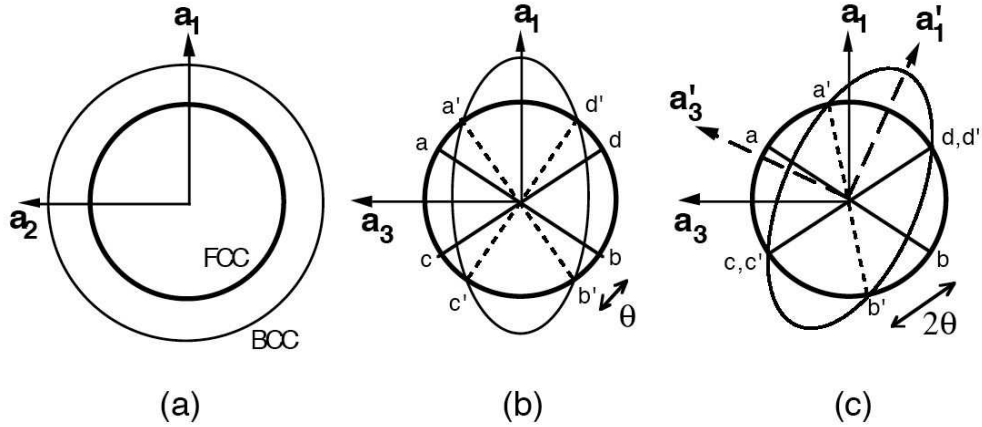


Figure 2.5: (a) and (b) represent the effect of the Bain strain on austenite, shown initially as a sphere of diameter ab . On deformation it takes the shape of an ellipsoid. (c) Shows the invariant-line strain obtained by a combined effect of Bain strain and the rigid body rotation [13].

illustrates that the rotation makes the initial and final cones of the unextended lines touch along the line $c'd'$. If the overall deformation is expressed as $(F S F) = (F B F)(F J F)$ which is a combination of the Bain strain and a rigid body rotation, then it leaves a line both unrotated and undeformed. However this strain is no longer a pure strain as the principal axes are rotated to new positions \mathbf{a}'_i .

The shape change due to martensite transformation has been characterised and found to be an invariant-plane strain $(F P F)$. This can be represented as:

$$(F P F) = I + m[F; \mathbf{d}](\mathbf{p}; F^*) \quad (2.2)$$

where the basis F is for convenience chosen to be orthonormal, although the general form of the equation is valid for any basis. $[F; \mathbf{d}]$ is an unit vector in the direction of shape deformation and $(\mathbf{p}; F^*)$ is an unit reciprocal lattice vector normal to the habit plane. However for $FCC \rightarrow BCC$ martensite

transformation lattice transformation strain (F S F), which is an invariant line strain, does not equal the observed shape deformation (F P F). (F S F) is therefore inconsistent with the observed deformation (F P F). This apparent anomaly has been resolved with the help of PTMC and is illustrated in Fig. 2.6. Fig. 2.6a shows the starting austenite crystal before transformation. Fig. 2.6b shows its shape after transformation, with the observed invariant-plane strain. However this intermediate state is not the required crystal structure as an IPS on its own can not transform austenite into BCC martensite [13]. But it has the correct shape as observed experimentally. To correct the crystal structure it is necessary to implement a second IPS, (F Q F) with magnitude n , on a plane with unit normal $(\mathbf{q}; \mathbf{F}^*)$ and in the unit direction $[\mathbf{F}; \mathbf{e}]$.

$$(\mathbf{F} \ \mathbf{Q} \ \mathbf{F}) = \mathbf{I} + n[\mathbf{F}; \mathbf{e}](\mathbf{q}; \mathbf{F}^*) \tag{2.3}$$

The combination of (F P F)(F Q F) is of course an invariant-line strain. It is recalled that for the austenite to martensite transformation the necessary crystallographic change requires an invariant-line strain (F S F) so this is consistent with (F P F)(F Q F). However the final shape is not that what is observed (Fig. 2.6c). To obtain the correct shape it is necessary to cancel the effect of (F Q F) without changing the crystal structure.

This is possible using a heterogeneous lattice-invariant deformation such as slip or twinning. The magnitude of this deformation must on average be equal and opposite to that of (F Q F). Fig. 2.6d shows the final martensite with the right crystal structure as well as the correct shape. There is one important characteristic of (F Q F), that it must not cause a volume change since it has to be cancelled by a lattice-invariant shear. Therefore, any dilatational strain is attributed entirely to (F P F), as observed experimentally. The determinant of a deformation matrix gives the ratio of

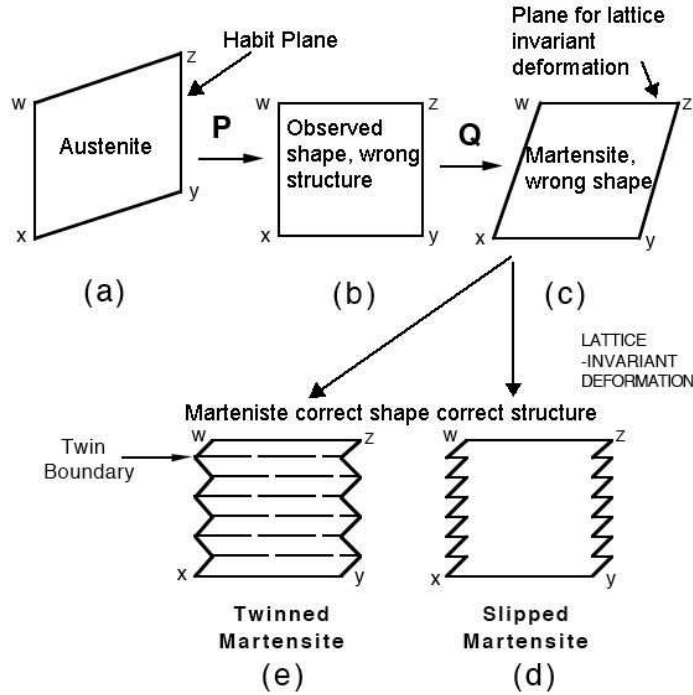


Figure 2.6: The IPS associated with the martensite transformation [13].

the volume after deformation to the entire volume so it follows that and $\det(F P F) = \det(F S F)$.

Hence, the theory of martensite can be summarised as follows:

$$(F S F) = (F J F)(F B F) = (F P F)(F Q F) \quad (2.4)$$

2.2.3 Factorisation of invariant-line strain

It seems obvious that a combination of two invariant-plane strains leaves a line invariant at the intersection of the two invariant planes. However it is important to get an insight into the problem from mathematical point of view. The derivation given by Bowles and MacKenzie [10, 11] will be described here. An invariant-line strain $(F S F)$ (S for convenience) is always characterised by the presence of an invariant line $[F; \mathbf{x}_i]$ and an invariant normal

$(\mathbf{n}_i; F^*)$ such that $(F S F)[F; \mathbf{x}_i] = [F; \mathbf{x}_i]$ and $(\mathbf{n}_i; F^*)(F S F)^{-1} = (\mathbf{n}_i; F^*)$. The first step of the factorisation of $(F S F)$ is to show that the displacement of all the vectors on a plane with plane normal $(\mathbf{p}_2; F^*)$ containing the line $[F; \mathbf{x}_i]$ can be achieved by an IPS on another plane having plane normal $(\mathbf{p}_1; F^*)$ which also contains the line $[F; \mathbf{x}_i]$. If we assume $[F; \mathbf{y}_2]$ to be a definite vector on the plane $(\mathbf{p}_2; F^*)$, then, $(\mathbf{p}_2; F^*)[F; \mathbf{y}_2] = (\mathbf{p}_2; F^*)[F; \mathbf{x}_i] = 0$. So any other vector on the plane $(\mathbf{p}_2; F^*)$ can be written as $\mathbf{x} = a\mathbf{y}_2 + b\mathbf{x}_i$, where $\mathbf{y}_2 = [F; \mathbf{y}_2]$ and $\mathbf{x}_i = [F; \mathbf{x}_i]$ and $\mathbf{x} = [F; \mathbf{x}]$. The displacement of any vector \mathbf{x} by the ILS is can be written as:

$$\mathbf{S}\mathbf{x} - \mathbf{x} = a[\mathbf{S}\mathbf{y}_2 - \mathbf{y}_2] + b[\mathbf{S}\mathbf{x}_i - \mathbf{x}_i] = a[\mathbf{S}\mathbf{y}_2 - \mathbf{y}_2] \quad (2.5)$$

which indicates that the displacement direction is same for all \mathbf{x} on the plane defined by the normal $(\mathbf{p}_2; F^*)$. It is also understood that since $(\mathbf{n}_i; F^*)[\mathbf{S}\mathbf{x} - \mathbf{x}] = 0$, all the vectors on the plane $(\mathbf{p}_2; F^*)$ are displaced in the same direction which lies in the plane with the invariant normal $(\mathbf{n}_i; F^*)$. An IPS on a plane $(\mathbf{p}_1; F^*)$, in the same direction of the displacement of all the vectors on plane $(\mathbf{p}_2; F^*)$ due to the ILS, $(F S F)$ can be expressed as:

$$(F P1 F) = I + k[\mathbf{S}\mathbf{y}_2 - \mathbf{y}_2](\mathbf{p}_1; F^*) \quad (2.6)$$

The displacement of the vectors $[F; \mathbf{x}]$ by the invariant line strain $(F S F)$ and the invariant plane strain $(F P1 F)$ are same provided: $a = k(\mathbf{p}_1; F^*)[a\mathbf{y}_2 + b\mathbf{x}_i] = ak(\mathbf{p}_1; F^*)\mathbf{y}_2$, because $(\mathbf{p}_1; F^*)[F; \mathbf{x}_i] = 0$. As the two planes $(\mathbf{p}_1; F^*)$ and $(\mathbf{p}_2; F^*)$ are distinct so $(\mathbf{p}_1; F^*)[F; \mathbf{y}_2] \neq 0$ and there exist a unique value for k for all possible \mathbf{x} . So the IPS on plane $(\mathbf{p}_1; F^*)$ can be written as:

$$(F P1 F) = I + [\mathbf{S}\mathbf{y}_2 - \mathbf{y}_2](\mathbf{p}_1; F^*)/((\mathbf{p}_1; F^*)\mathbf{y}_2) \quad (2.7)$$

The remaining part of the ILS $(F S F)$ is a strain which must leave invariant the plane generated from the plane $(\mathbf{p}_2; F^*)$ due to the ILS. That

invariant plane would be $(\mathbf{p}_2; \mathbf{F}^*)(\mathbf{F} \mathbf{S} \mathbf{F})^{-1}$. The strain on this plane must also displace all the vectors in the plane $(\mathbf{p}_1; \mathbf{F}^*)$ to their final positions. So if $[\mathbf{F}; \mathbf{y}_1]$ be any vector (also mentioned in some of the equations as \mathbf{y}_1) in the plane $(\mathbf{p}_1; \mathbf{F}^*)$ and distinct from $[\mathbf{F}; \mathbf{x}_i]$ then the second IPS can be written as:

$$(\mathbf{F} \mathbf{P} 2 \mathbf{F}) = \mathbf{I} + [\mathbf{S}\mathbf{y}_1 - \mathbf{y}_1](\mathbf{p}_2; \mathbf{F}^*) / ((\mathbf{p}_2; \mathbf{F}^*)\mathbf{S}^{-1}\mathbf{y}_1) \quad (2.8)$$

So the ILS can be factorised as:

$$\begin{aligned} (\mathbf{F} \mathbf{S} \mathbf{F}) = & \{ \mathbf{I} + [\mathbf{S}\mathbf{y}_2 - \mathbf{y}_2](\mathbf{p}_1; \mathbf{F}^*) / ((\mathbf{p}_1; \mathbf{F}^*)\mathbf{y}_2) \} \\ & \{ \mathbf{I} + [\mathbf{S}\mathbf{y}_1 - \mathbf{y}_1](\mathbf{p}_2; \mathbf{F}^*) / ((\mathbf{p}_2; \mathbf{F}^*)\mathbf{S}^{-1}\mathbf{y}_1) \} \end{aligned} \quad (2.9)$$

It is thus proven that it is possible mathematically to factorise one ILS into two IPSs.

2.2.4 Other forms of phenomenological theory of martensite crystallography

The other form of PTMC was proposed by Wechsler, Lieberman and Read [21] (WLR theory). The shape deformation is given by \mathbf{E} , which will not generate the product lattice from that of the parent. The matrix \mathbf{E} can be written as:

$$\mathbf{E} = \mathbf{R}\mathbf{B}\mathbf{G} \quad (2.10)$$

where \mathbf{R} is a rigid body rotation, \mathbf{B} the Bain deformation and \mathbf{G} is the second shear which is compensated for by the lattice invariant deformation. As demonstrated by Christian [23], the Bowles MacKenzie and the Wechsler, Lieberman and Read theories are identical.

2.3 Stress, strain and transformation texture

The crystallographic texture in materials can be described, using pole figures, by measuring the intensities of diffracted X-rays [24]. For example, texture in rolled sheets is often described as $\{hkl\}\langle uvw\rangle$, which means that for most of the crystals the $\{hkl\}$ planes lie parallel to the sheet surface and the rolling direction is roughly parallel to the $\langle uvw\rangle$ direction. The texture can be complex with many components, $\sum \lambda_i \{hkl\}\langle uvw\rangle$, where λ_i is a weighting factor describing the relative intensity of each component. The position of $\{200\}$ poles are useful in visualising texture components. Fig. 2.7a shows the $\{200\}$ pole figure of some well known deformation/recrystallisation components of austenite texture, and Fig. 2.7b martensite. Of the components of martensite, the $\{332\}_{\alpha'}\langle 113\rangle_{\alpha'}$ forms from austenite with $\{110\}_{\gamma}\langle 112\rangle_{\gamma}$ texture, the $\{113\}_{\alpha'}\langle 110\rangle_{\alpha'}$ component is similarly derived from $\{112\}_{\gamma}\langle 111\rangle_{\gamma}$. Furthermore $\{100\}_{\alpha'}\langle 011\rangle_{\alpha'}$ is produced from the major recrystallisation component of γ , *i.e.*, the Cube component $\{100\}_{\gamma}\langle 001\rangle_{\gamma}$ [25].

2.3.1 Texture from strained austenite

The term “variant selection” must be discussed in detail now as it plays a crucial role in the formation of transformation texture. It is well known that there are 24 variants of martensite in steels, for example according to the Kurdjumov-Sachs orientation relationship. The chemical driving force for transformation is the same for all, a function of temperature and composition. In general, each variant has an equal chance of existence. Since martensitic transformation is a deformation, an applied stress will favour those variants that comply with the stress, *i.e.*, variant selection occurs. It has been shown, for example, by Gey *et al.* [8] that different deformation textures in austenite result in different orientations of martensite. Figs 2.8a and 2.9a show the experimentally determined Cube and Goss components of austenite and the

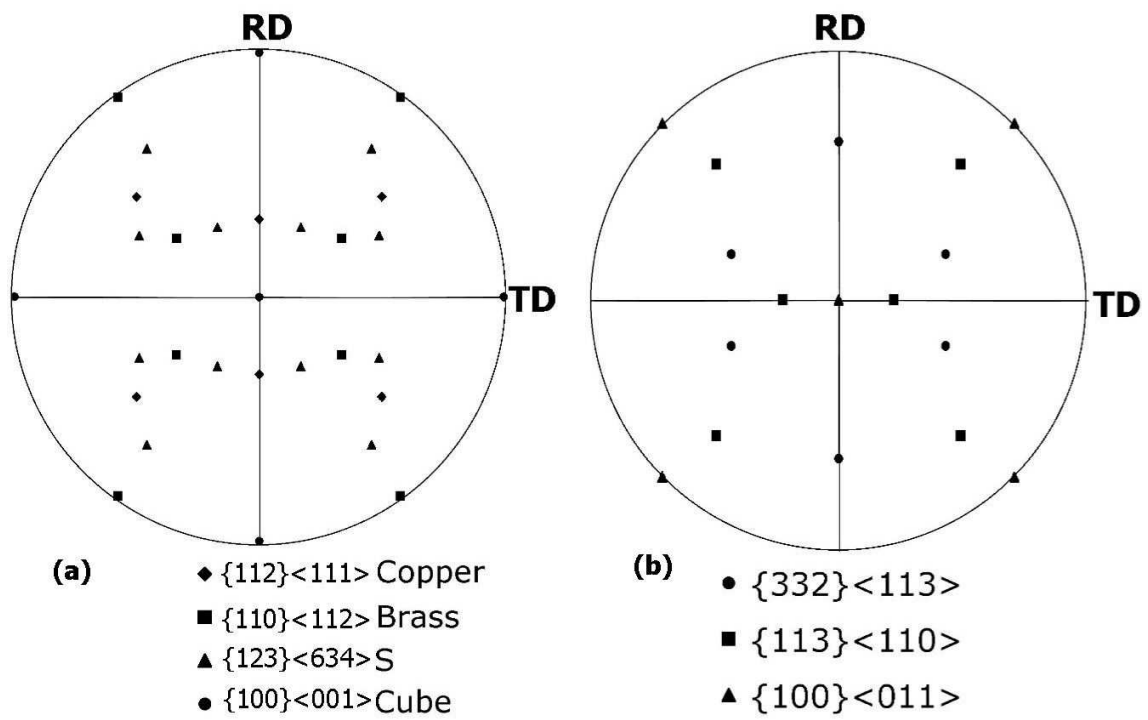


Figure 2.7: 2 0 0 pole figures relative to the rolling (RD) and transverse (TD) directions (a) austenite and (b) martensite [25].

subsequent transformation textures due to these components (Fig. 2.8b,c and Fig. 2.9b,c). Fig. 2.8b and Fig. 2.9b show the experimentally determined martensite texture, where there is variant selection as transformation occurs under stress. On the other hand Fig. 2.8c and Fig. 2.9c show the pole figure of martensite calculated without any variant selection criteria. This clearly shows that variant selection leads to a stronger texture.

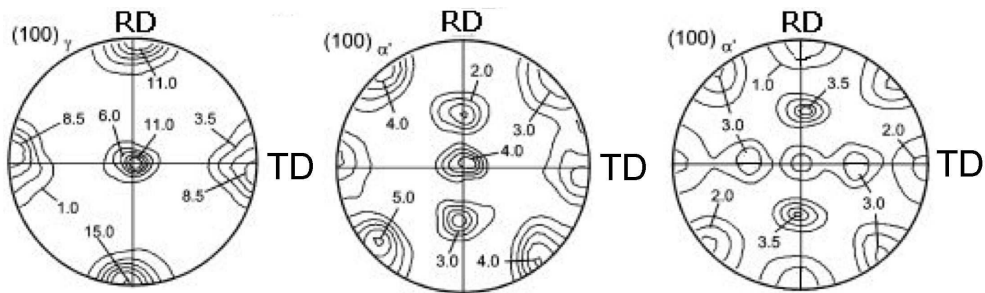


Figure 2.8: (a) Cube type deformation texture in austenite (experimental). (b) Transformation texture of martensite formed from Cube textured austenite with variant selection (experimental). (c) Calculated martensite texture from Cube type austenite texture (without imposing variant selection) [8].

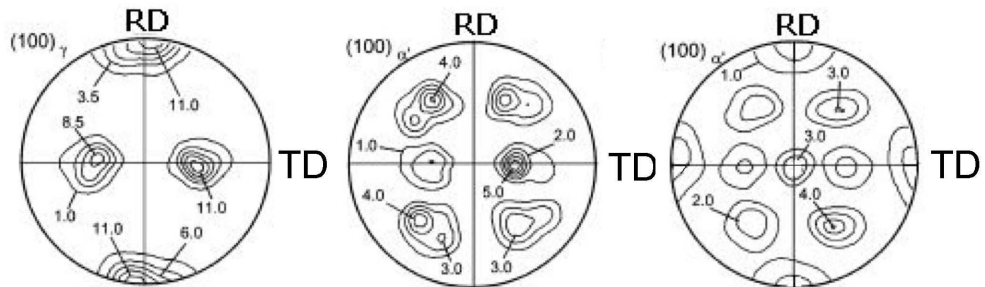


Figure 2.9: (a) Goss type deformation texture in austenite (experimental). (b) Transformation texture of martensite formed from Goss textured austenite with variant selection (experimental). (c) Calculated martensite texture from Goss type austenite texture (without imposing variant selection) [8].

A variety of variant-selection models have been proposed, each of which is now discussed.

Shape deformation model: Following Patel and Cohen [12], the interaction energy between a plate of martensite and the applied stress is given by Eq. 2.1. The angle between the direction of applied stress acting on the habit plane with the plane normal is different for each variant. For this reason the value of σ_N and τ are also different for different variants of martensite and so is the value of ΔG_{mech} or U . A greater value of ΔG_{mech} increases the possibility of that variant forming. This model is appropriate when martensite forms under stress below the yield strength of the austenite. However it will later be shown that it can also be used in the plastic region.

Bokros-Parker (BP) Model: It was first proposed by Bokros and Parker [26] and later supported by Durlu *et al.* [27], that there is an interaction between slip systems and habit plane variants. In a study of plastically deformed single crystals of Fe-Ni, variants with habit planes nearly perpendicular to the active slip plane were found to be favoured. This behaviour is attributed to the formation of anisotropic dislocation substructures during deformation, which interferes with the growth of α' plates, the exact growth direction being normal to the sub-boundaries. Such effects become prominent at large strains [28] but might otherwise be neglected. For example, it has been shown in the present work that when an austenitic stainless steel is elongated by 10% and then transformed to martensite, the resulting crystallographic texture can be calculated using the Patel and Cohen criterion alone. This is described in detail in Chapter 5.

Twinning-Shear (TS) Model: This was proposed by Higo *et al.* [29], based on the double shear mechanism of martensite crystallography. It is argued that the first shear for FCC to BCC transformation is that which gets affected by the applied stress. The critical atomic movement to initiate martensite formation is said to be the first shear along $\{111\}_\gamma \langle \bar{2}11 \rangle_\gamma$ direction. This is consistent with Bogers and Burger's [30] mechanism for martensitic transformation, which described the orientation relationship be-

tween the product and the parent phase by the movement of dislocations on suitable slip systems. The other variety of this theory which has been developed by Kato and Mori [31, 32] relies upon the concept proposed by Bogers and Burger's [30] which was based on a dislocation movement mechanism during martensitic transformation. Although the orientation relationship between parent and the product phase could be described correctly by this theory, it failed to predict the habit plane and the shape deformation matrix necessary for the martensite transformation.

Bain-Strain (BS) Model: Proposed by Furubayashi *et al.* [9, 33] is based on the interaction of the applied stress with the Bain strain alone. There are three Bain variants in martensite with $[100]_\gamma$, $[010]_\gamma$ and $[001]_\gamma$ as their compression axes respectively. A compressive stress is applied along $[100]_\gamma$ direction stimulates only those variants that originate from that Bain distribution. This model also demarcates between texture formation when transformation takes place during rolling and after rolling.

2.3.2 Comments on variant selection model

Furubayashi *et al.* carried out computer simulations of the various models discussed so far and compared then with experimental results [9]. The simulation was carried out for martensite transformed from austenite having a Cu-type rolling texture with 360 or 720 initial orientations representing the initial texture of austenite. Fig. 2.10 shows the comparison between experimental and model-predicted texture development in a Fe-Ni steel. Fig. 2.10a shows the experimental texture generated from austenite having Cu-type texture, Fig. 2.10b and Fig. 2.10c show respectively the model prediction following the Bokros-Parker and Twinning-Shear theory. It can be said that in TS theory texture prediction is much better than that obtained following the BP theory.

However the prediction from the Bain strain model looks to be the

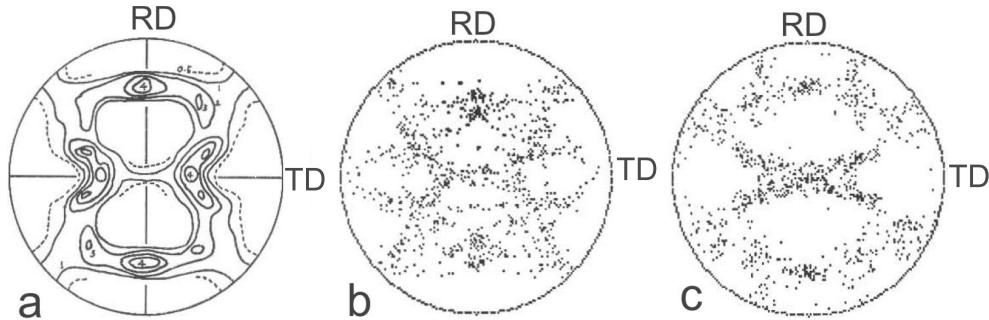


Figure 2.10: 100 pole figure of martensite (a) Experimental texture developed from austenite with Cu-type texture. (b) Model prediction following the Bokros-Parker model. (c) model prediction following the TS model. [25].

most promising one amongst all the models described so far. A comparison between the predicted result and the experimental one is shown in the Fig. 2.11. Nonetheless the justification of using the Bain orientation as the orientation relationship between martensite and austenite can be questioned. It is well known that Bain orientation deviates by 11.06° and 9.7° from the well known Kurdjumov-Sachs or Nishiyama-Wasserman relationships. The twinning-shear model is based on the double shear theory of martensite crystallography, which for the sake of brevity has not been explained here, is in fact inconsistent with the existence of a glissile interface. So the applicability of twinning-shear model is also not beyond question. Both the Bain-strain model and the twinning-shear model neglect the total deformation due to martensite transformation. As a result these models would fail when the transformation strain is also needed.

The Patel-Cohen theory is the only one that uses the total deformation of α' and thus can be incorporated into a model for predicting the transformation strain in a polycrystalline system. In Furubayashi's work [9] no systematic comparison was made between the Patel-Cohen model and the other theories.

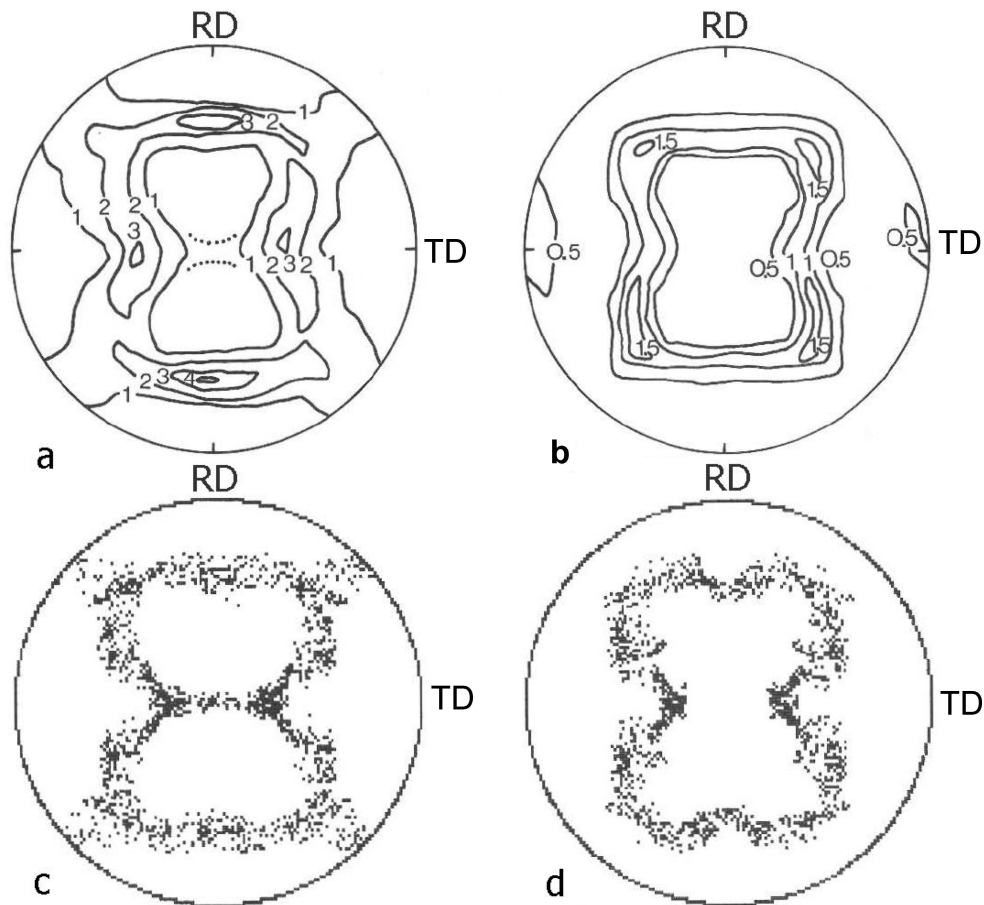


Figure 2.11: 100 pole figure of martensite obtained experimentally from austenite with Cu-type orientation (a) transformation after rolling, (b) transformation during rolling. Model prediction using Bain strain model, (c) transformation after rolling simulation, (d) transformation during rolling simulation. [25].

2.4 Microstructural and kinetics effect

2.4.1 Effect of stress

In an Fe-Ni alloy martensite can form 70°C above the ordinary M_S (martensite start temperature) temperature under stress (known as M_σ) [34]. Maxwell *et al.* [34] found that the shape of the martensite formed under the influence of stress depends on the temperature at which it forms. Plates formed just above M_S are similar to ordinary martensite but become irregular and smaller in size at higher temperatures (Fig. 2.12). On the other hand, others [35, 36] have reported that martensite formed under stress is completely different, and suggested a change in the nucleation or the growth process.

The effect of stress on variant selection during the bainite transformation has been studied in detail by Shipway *et al.* [16] and Hase *et al.* [37].

Fig. 2.13 shows bainite transformed isothermally at 300°C under uniaxial compression (4 MPa and 200 MPa) in Fe-0.79C-1.56Si-1.98Mn-0.002P-1.01Al-0.24Mo-1.01Cr-1.51Co (wt%) alloy. There is a clear tendency for the bainite to align roughly parallel to the planes of maximum shear stress. The sheaves tend to be flatter in the stressed samples, as there is less interference from other variants. The transformation rate also changes as ΔG_{mech} contributes to the overall free energy change (Fig. 2.14). The effect is smaller at larger under cooling below bainite start temperature (B_S) since the chemical driving force then dominates.

2.4.2 Effect of strain

Strain significantly influences the morphology of martensite [34, 35, 38]. Fine laths form along slip bands or twin boundaries in the austenite, as much as 200°C above the M_σ temperature [34].

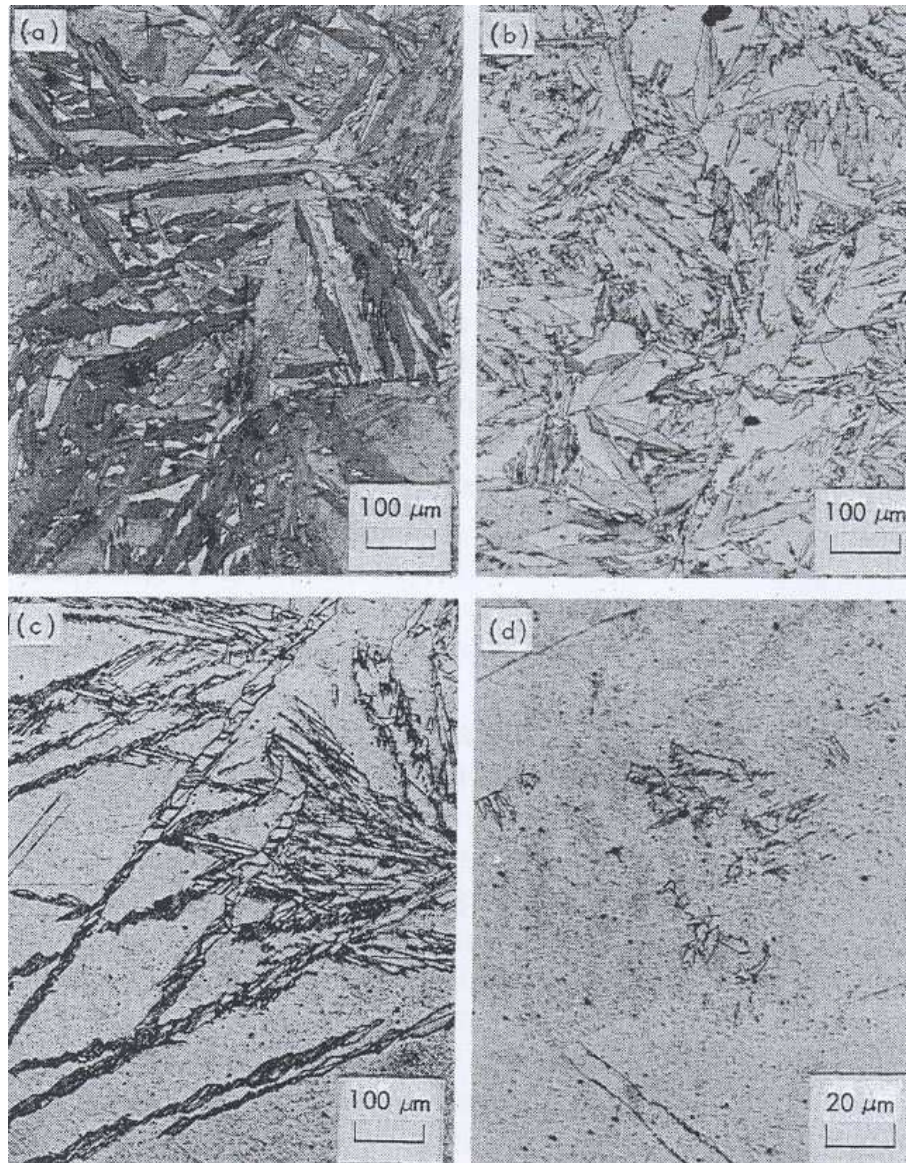


Figure 2.12: Microstructure of a Fe-32Ni-0.017C (wt%) alloy ($M_S = -72^\circ\text{C}$) tested in tension to failure at (a) -70°C (b) -50°C (c) -30°C (d) 0°C . After Maxwell *et al.* [34].

Figs. 2.15 and 2.16 show strain-induced martensite on a twin boundary and along slip bands in austenite respectively.

Fig. 2.17 shows that stress accelerates transformation kinetics in a Fe-

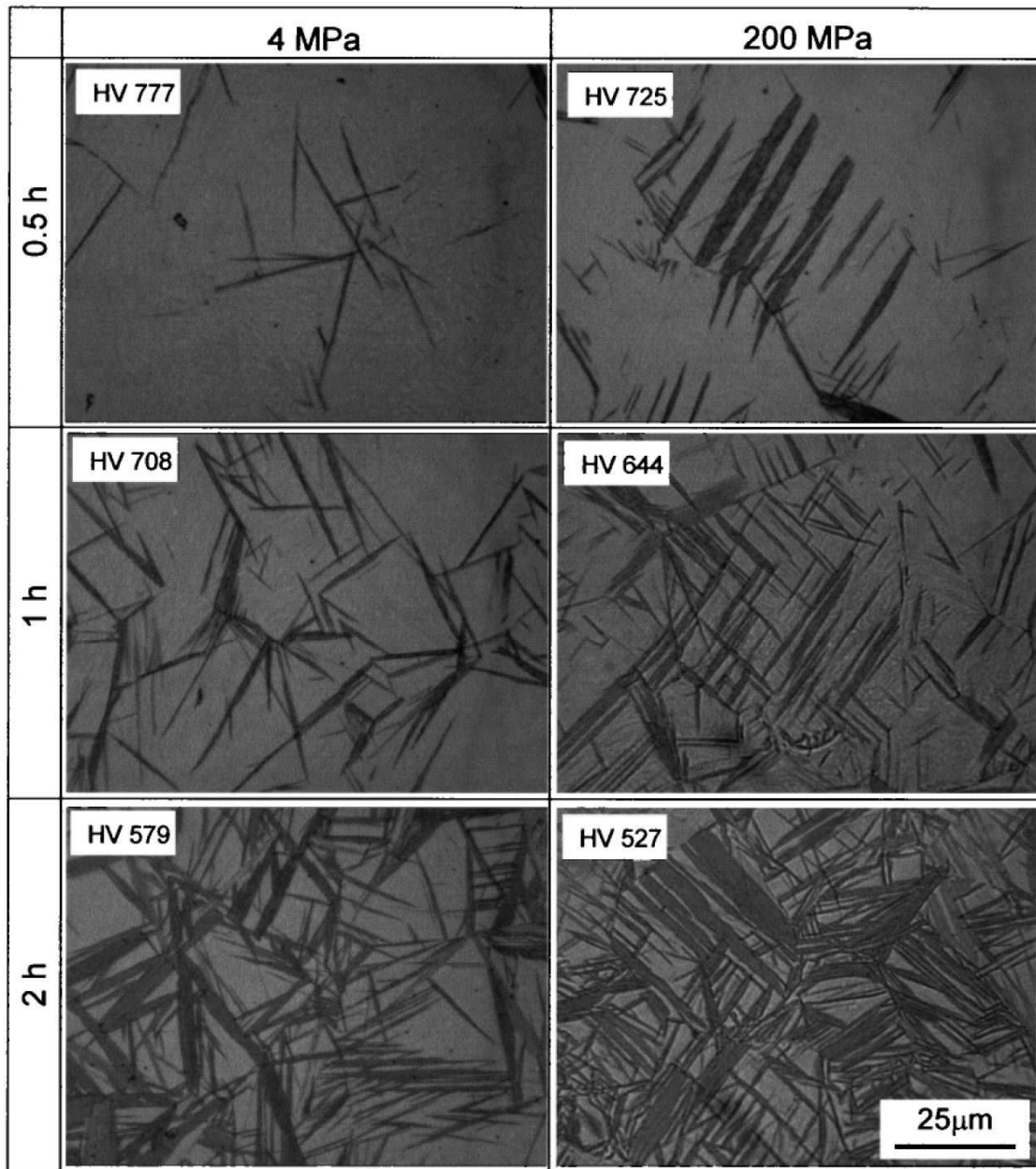


Figure 2.13: Optical micrographs of bainite transformed at 300°C under compressive stress. Stress axis is vertical in each case [37]. HV represents hardness in Vicker's scale.

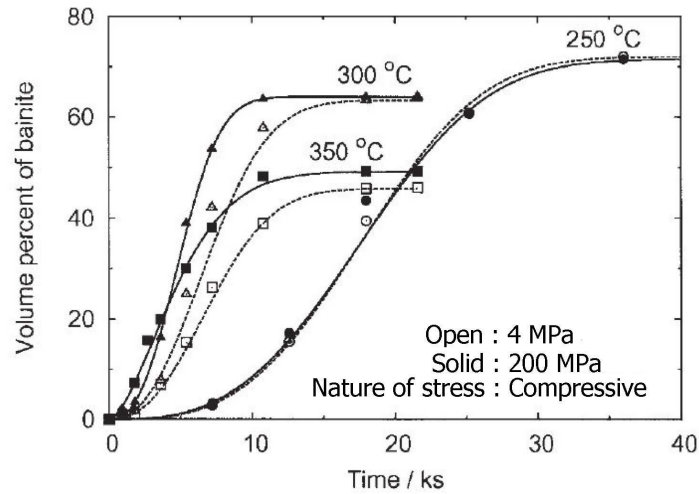


Figure 2.14: Isothermal transformation kinetics of bainite at various temperatures and stress. Composition : Fe-0.79C-1.56Si-1.98Mn-0.002P-1.01Al-0.24Mo-1.01Cr-1.51Co (wt%). After Hase *et al.* [37].

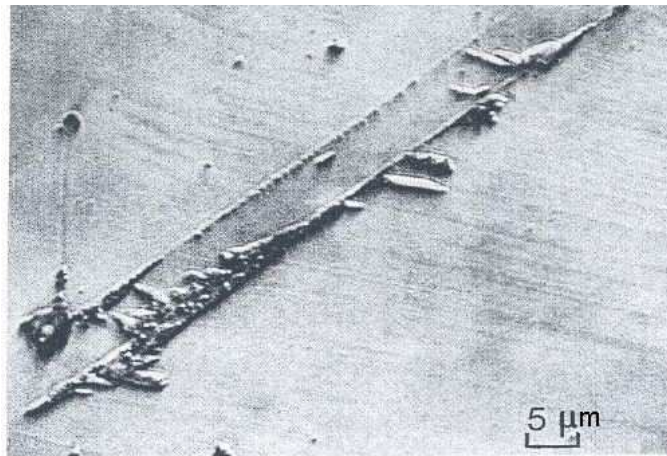


Figure 2.15: Preferential nucleation of martensite at twin boundary in a Fe-30Ni-0.02C (wt%) ($M_S = -25^\circ\text{C}$) alloy strained 20 % at -20°C [35].

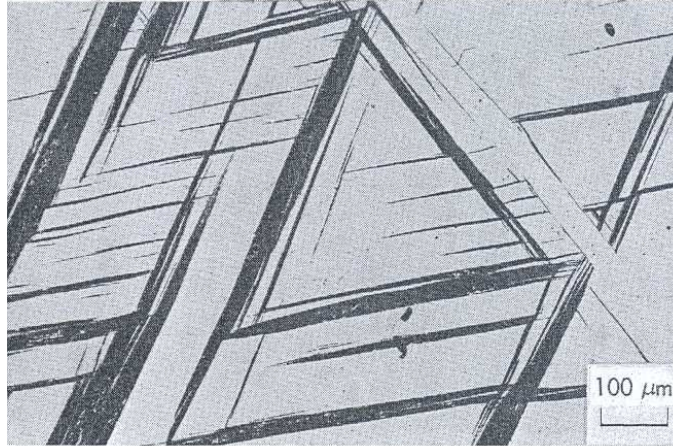


Figure 2.16: Morphology of strain-induced martensite formed along the $\{111\}\langle 1\bar{1}0\rangle$ slip system of austenite in a Fe-20Ni-0.6C (wt%) alloy ($M_S = -36^\circ\text{C}$). Specimen is tensile tested to failure at 106°C [35].

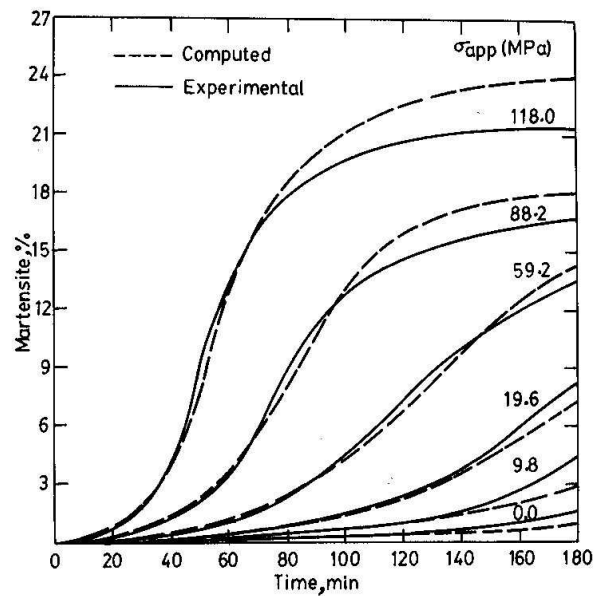


Figure 2.17: Effect of stress on the isothermal transformation kinetics of martensite at 173 K [39].

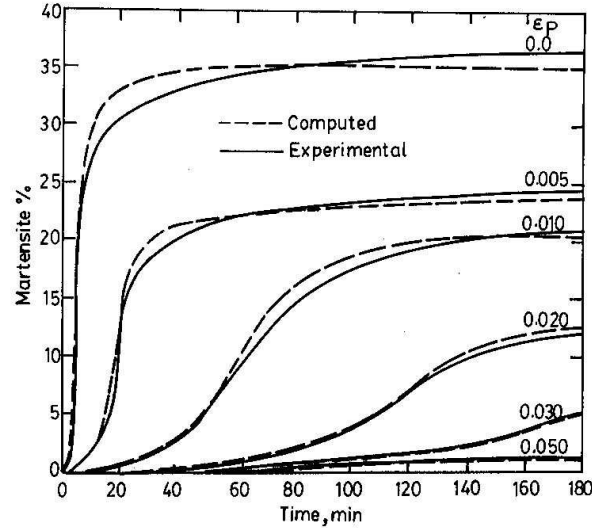


Figure 2.18: Effect of strain on the isothermal transformation kinetics of martensite at 77 K. After Ghosh [39].

23.2Ni-2.8Mn-0.009C (wt%) alloy [39] by increasing the nucleation rate. The effect of the stress progressively decreases as the transformation temperature is reduced. In contrast, transformation from plastically strained γ is retarded when the strain is large (Fig. 2.18). ϵ_P in Fig. 2.18 denotes the plastic strain that the specimen is subjected to before transformation. This phenomenon is known as mechanical stabilisation. Plastic deformation hardens the austenite and hinders the growth of martensite or bainite, which requires the movement of interfacial dislocations. The initial increase in rate (as shown in Fig. 2.19 for bainitic transformation from strained austenite) is associated with a greater number density of nucleation sites.

Durlu [41] pointed out that in a Fe-Ni-C alloy, martensite forms in parallel packets in an austenite grain, the number of parallel groups, increasing with plastic strain. This can be taken as indirect evidence of the variant selection for martensite in plastically strained austenite and such evidence has been shown for bainite by Umemoto *et al.* [42].

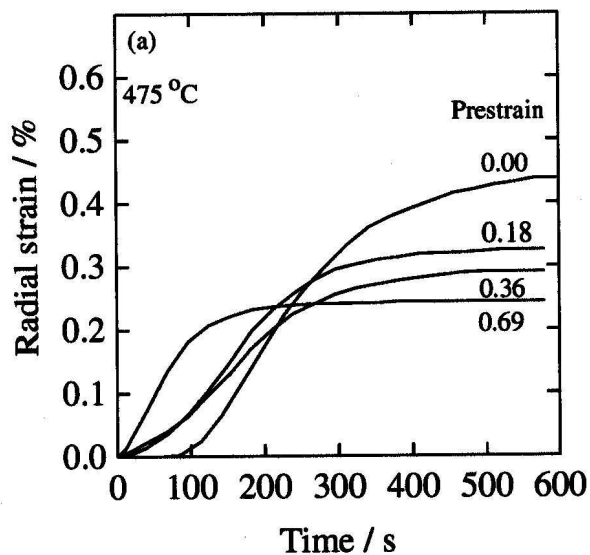


Figure 2.19: Effect of pre-strain on the bainite transformation at 475°C in a Fe-0.12C-2.03Si-2.96Mn (wt%) alloy. After Singh [40].

2.5 Stress/strain-induced transformation and mechanical properties

The shape deformation during certain phase transformations may have a significant impact on the properties of engineering alloys. It is possible to exploit these in order to design better engineering alloys.

2.5.1 Residual stress

Manufacturing processes frequently introduce unwanted residual stresses in mechanical assemblies [43]. This affects the fatigue life of the engineering structure. There are various material properties like heat capacity, thermal expansion coefficient, density and strength which significantly affect the development of residual stress [44, 45]. However, in steel the phase transformation itself can affect the development of residual stress. The work done by Albery and Jones [3] showed how transformation temperature influences

the evolution of stress in materials when a constrained tensile specimen is cooled from the austenite phase.

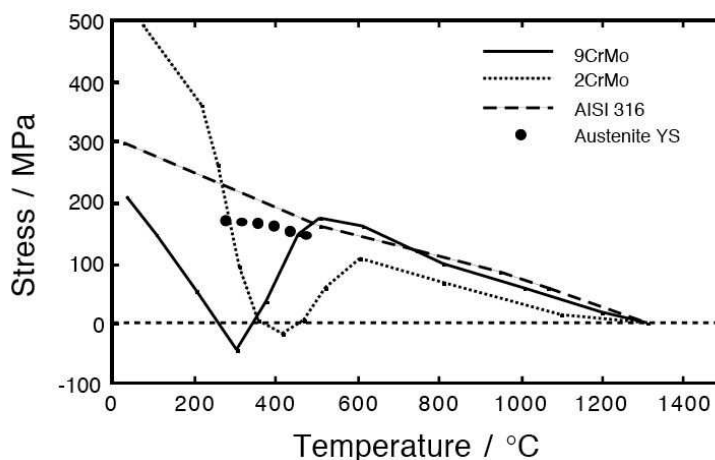


Figure 2.20: Axial stress in uniaxially constrained samples during cooling of a martensitic (9Cr1Mo), bainitic (2.5Cr1Mo) and austenitic steel (AISI 316) [3]. Also plotted is the yield strength of austenite [15].

Fig. 2.20 shows the evolution of stress with temperature for alloys with a variety of transformation temperatures. If the thermal expansion coefficients of ferrite and austenite (e_α and e_γ) are taken to be $13 \times 10^{-6} \text{K}^{-1}$ and $21 \times 10^{-6} \text{K}^{-1}$ respectively the amount of stress generated due to thermal contraction would be 4 MPa per 1 K cooling in the austenite phase (given a Young's modulus of 210 GPa). However the accumulated stress due to this is larger than the yield strength of austenite which therefore released by plastic relaxation. This is why the stress in the austenite roughly follows its yield strength. The 2.5Cr1Mo sample begins to transform to bainite at $\sim 600^\circ\text{C}$; when this happens, the transformation strain associated with the transformation partly compensates for the thermal contraction stress. It is also clear from Fig. 2.20 that lowering the transformation temperature (9Cr1Mo) of the alloy leaves a lower stress at ambient temperature, *i.e.* an alloy with lower transformation temperature is a better choice for combating the development

of stress. The reasons for this are as follows:

1. If transformation is exhausted much before ambient temperature is reached, it is ferrite that contracts on cooling. Ferrite has a higher yield strength at low temperatures and thus better resists thermal contraction, allowing the stress to accumulate.
2. Displacive transformation at lower temperatures should give rise to a greater bias in the microstructure because of the larger stress reached. Thus the macroscopic shear strain generated during transformation would be much higher. This is more effective in countering the thermal contraction strain.

2.5.2 Fatigue

Many engineering components are fatigue limited. Cracks are initiated and grow slowly under the influence of an oscillatory stress whose magnitude is below the yield stress. The failure in the component occurs when the crack size reaches a critical value. Residual stress reduces the allowable externally applied stress. A secondary effect is that the shape strain due to martensite or bainite may be partially plastically accommodated. The resulting dislocations help in increasing the fatigue strength. Dislocations can increase the fatigue strength by increasing the resistance to the plastic flow. This conclusion follows from the fact that pre-straining a component prior to fatigue loading can increase its life [4] especially during low-strain fatigue [46]. The defects introduced by phase transformation have a similar effect to the “pre-straining” and thus are believed to be helpful in resisting fatigue crack growth [47].

In recent years, attempts have been made to make use of transformation plasticity in welded joints [2, 48, 49] in order to increase fatigue life.

Fig. 2.21 illustrates distortion caused by welding. The angle θ is a

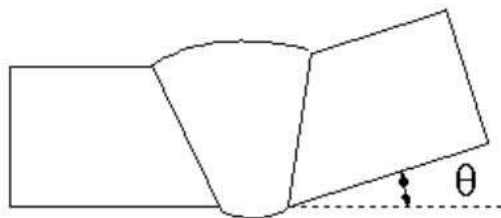


Figure 2.21: Distortion caused by welding two plates which were originally flat [4].

Table 2.1: The chemical compositions (wt%), calculated transformation temperature range (ΔT) and measured distortion θ for two manual metal arc multipass weld deposits [4].

C wt%	Si	Mn	Ni	Mo	Cr	$\Delta T/^\circ\text{C}$	$\theta/^\circ$
0.06	0.5	0.9	-	-	-	802-400	14.5
0.06	0.3	1.6	1.7	0.4	0.35	422-350	8

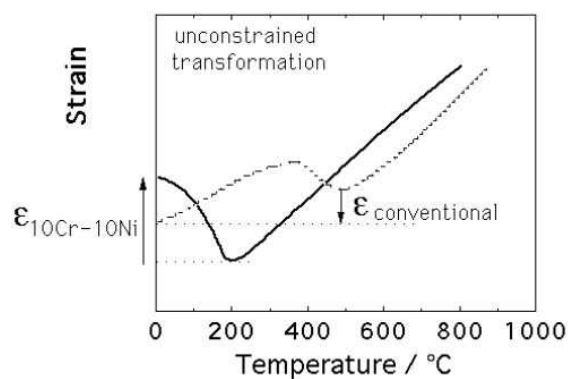
measure of the distortion caused by the rotation of the unconstrained plate during cooling after the solidification. Table 2.1 shows θ as a function of the transformation temperature range, for two welding alloys deposited within a 60° V-joint. The distortion is clearly larger for the case where the transformation is exhausted at a higher temperature.

Ohta *et al.* [2, 48, 49] designed an alloy with a low M_S temperature of $\sim 180^\circ\text{C}$ in comparison to conventional alloys with M_S , $400 - 500^\circ\text{C}$ (Table 2.2). Fig. 2.22a shows that the net strain due to cooling from M_S to the ambient temperature is a contraction for the conventional alloy, whereas a net expansion results for the low M_S alloy while cooling. This cancels the contraction stress in the latter case (Fig. 2.22b).

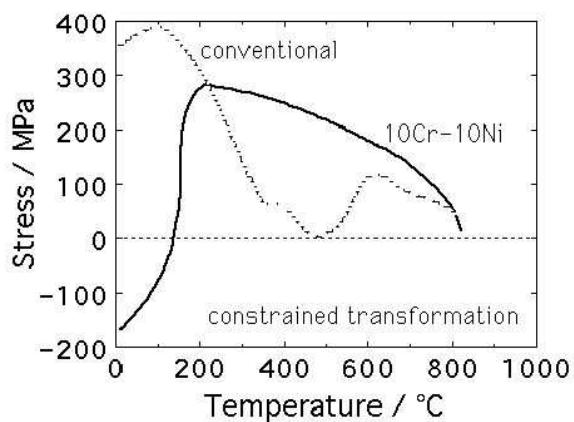
When fatigue tests are done on welded sections, low- M_S weld metal gave much higher fatigue strength than conventional weld metal, as shown

Table 2.2: The chemical compositions (wt%), and measured M_S temperatures of conventional and novel welding alloys [2].

Alloy	C wt%	Si	Mn	Ni	Mo	Cr	$M_S/^\circ\text{C}$
conventional	0.10	0.39	0.90	-	-	-	590
10Cr10Ni	0.025	0.32	0.70	10.0	0.13	10.0	180



(a)



(b)

Figure 2.22: (a) Transformation of weld metal during unconstrained cooling; (b) development of stress during constrained cooling. The chemical compositions of the alloys are given in Table 2.2. The low- M_S alloy is designated 10Cr10Ni in Table 2.2 [2].

in the Fig. 2.23. This is because of the compressive residual stress due to the suppressed transformation. This development may radically change the design and lifting philosophies for structural components. This result has been recently confirmed by Ekerlid *et al.* [50] using a different alloy.

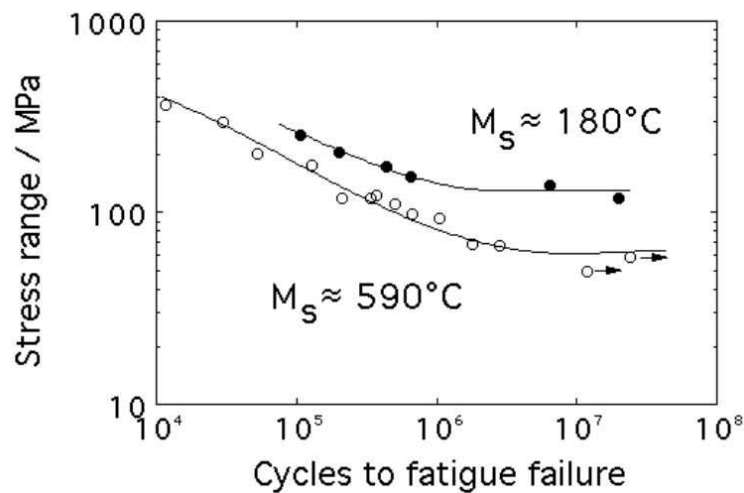


Figure 2.23: Improvement in the fatigue performance of welded structure using a low transformation temperature welding alloy [4].

2.6 Evolution of martensitic transformation

2.6.1 Koistinen-Marburger equation

This is the most widely used empirical equation for estimating the fraction of martensite below M_S [51]. Iron carbon alloys were prepared by vacuum melting and the M_S temperatures were determined following the technique of Digges [52] and Greninger [53]. The alloys were then austenitised and quenched to various known temperatures. The amount of retained austenite was measured using X-ray diffraction. Then results for a variety of steels were plotted logarithmically against $(M_S - T_q)$, where T_q is the quenching

temperature. A straight line was fitted to the data points,

$$V_\gamma = \exp[-b(M_S - T_q)] \quad (2.11)$$

where the value of b is $1.10 \times 10^{-2} \text{ K}^{-1}$, V_γ is the volume fraction of austenite and T_q is the quenching temperature.

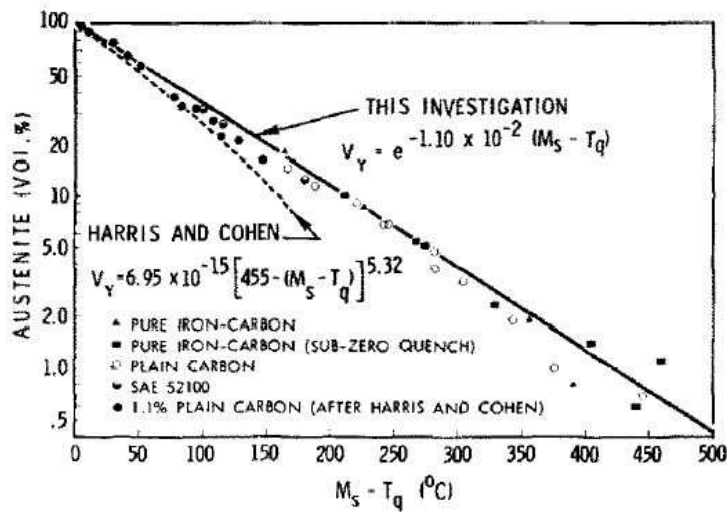


Figure 2.24: Experimental data plotted on semi-logarithmic coordinates and the empirical equation derived by fitting a straight line. The data obtained by Harris and Cohen [54] are shown together with the equation they have proposed [51].

It has been shown by Magee [55] that an equation of the form Eq. 2.11 can be derived based on martensite nucleation theory.

2.6.2 Justification of Koistinen-Marburger equation

The amount of martensite that forms at any temperature increases with the under cooling below M_S . The difference in free energy per unit volume between austenite and martensite can be written as $\Delta G_V^{\gamma-\alpha'}$, which is negative below M_S . If it is assumed that the number of new plates of martensite dN

(per unit volume) at any temperature T_q is proportional to the driving force we get:

$$dN = -\varphi d(\Delta G^{\gamma-\alpha'}) \quad (2.12)$$

where φ is an empirical proportionality constant. The change in the volume fraction martensite, df , and the change in the number of new plates per unit volume is related:

$$df = \bar{V} dN_v \quad (2.13)$$

where \bar{V} is the average volume of the plate formed. Since $dN_v = (1 - f)dN$ and $d\Delta G_v^{\gamma-\alpha'} = \frac{d\Delta G_v^{\gamma-\alpha'}}{dT}dT$, on rearranging equation 2.12 we get:

$$\ln(1 - f) = \bar{V} \varphi \left(\frac{d\Delta G_v^{\gamma-\alpha'}}{dT} \right) (M_S - T_q) \quad (2.14)$$

or

$$f = 1 - \exp \left[\bar{V} \varphi \left(\frac{d\Delta G_v^{\gamma-\alpha'}}{dT} \right) (M_S - T_q) \right] \quad (2.15)$$

On comparing with Eq. 2.15 it is clear that b in the Koistinen-Marburger equation is equivalent to the term

$$\bar{V} \varphi \frac{\partial \Delta G_v^{\gamma-\alpha'}}{dT} \quad (2.16)$$

of Magee's equation. It is often assumed that \bar{V} remains more or less constant during the course of transformation. Brook *et al.* [56] have shown that b can be correlated directly with $\partial \Delta G_v^{\gamma-\alpha'} / dT$. Bohemen *et al.* [57] demonstrated for steels of different carbon content, that b does not change much with $\partial \Delta G_v^{\gamma-\alpha'} / dT$ or \bar{V} but a larger effect comes from φ . They have attributed this effect to the varying dislocation densities in the microstructure. A higher dislocation density would effectively increase the number of potential embryos in the material apart from those present in the austenite initially. They have argued that the dislocation density in the steel would increase until 0.6

wt% C because with the increase in carbon content in steel more dislocation will be involved in slipping caused by the shear stress associated with the transformation. For steels containing more than 0.6 wt% carbon, Brook *et al.* argued that the transformation strain would be partially accommodated by twinning which leads to fewer dislocations in the microstructure. The evolution of martensite fraction should be different from that described above if transformation occurs from a plastically deformed austenite [58].

2.7 Summary

The importance of the shape deformation during martensitic or bainitic transformation is clear. The crystallographic theory of martensitic transformation is elegant in that it rigidly links all its features in a mathematical framework. There is clear evidence that the theory may be extrapolated in understanding the evolution of transformation texture. The importance of variant selection and its effect on the transformation texture has been given. Various mathematical models developed by different scientists to predict the variant selection from stressed and strained austenite have been presented and a critical assessment of these models has been made. The effect of stress and strain on the kinetics and morphology of martensite and bainite transformation has been discussed in detail. It has been shown that the stress and strain affect the transformation texture, microstructural features and the kinetics of martensite transformation to a high degree and this might influence the important properties like residual stress and fatigue.

The topics discussed in this chapter provide the background of the present study. The importance of the shape deformation in determining the transformation texture and the transformation strain will be discussed in detail in latter chapters. Mathematical models will be presented based on the phenomenological theory of martensite crystallography to predict the

texture and strain during martensite or bainite transformation.

Chapter 3

The transformation strain

3.1 Introduction

When displacive transformations such as bainite or martensite occur the strain consists of a volume and a shear component. The latter is generally invisible when all the possible variants form. They then tend to cancel their shear components. However, when transformation occurs under the influence of stress, some of the variants have a larger probability of formation and this generates a texture allowing the shear strain to make a greater contribution to the macroscopic shape. A model has been developed here to predict both the change in macroscopic strain and the texture.

Crystallographic data justified by the theory of martensite [10, 11, 21]. are used to calculate the interaction between the transformation product and the applied system of stresses. It is this interaction which leads to the bias in the microstructure since compliant variants are favoured [12].

The work to create a model for these phenomena is inspired by attempts to design welding alloys which counter the build up of residual stresses in welded joints [2, 4, 48, 50, 59]. The strains caused by displacive phase transformations can in principle be manipulated to counter those due to thermal

contraction in constrained welded joints. The technological benefit of doing this is to dramatically improve the fatigue performance of the joints [59]. It would be useful therefore to be able not only to estimate the development of transformation texture, but also the anisotropic transformation strains caused by the biased microstructure that develops under the influence of stress.

This chapter begins with a self-consistent crystallographic description of the transformation strain in a polycrystalline aggregate of austenite and then shows the model predicted results along with those from experiments. An interesting theory is proposed to predict the extent of variant selection from the knowledge of mechanical and chemical free energy available for the transformation.

3.2 Crystallography

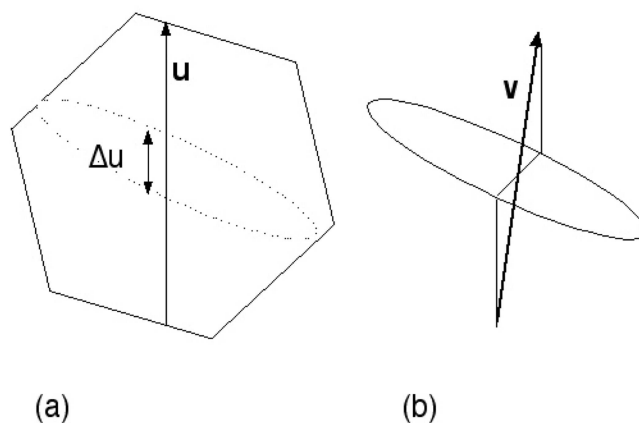


Figure 3.1: The deformation of an initial vector \mathbf{u} by the formation of bainite or martensite. (a) An austenite grain prior to transformation, with the ultimate location of a plate of bainite/martensite marked. (b) Following bainitic/martensitic transformation.

Throughout this work, the vector and matrix notation due to Bowles and MacKenzie is used because it is particularly good at avoiding confusion between frames of reference [10, 13]. Consider a polycrystalline sample of austenite which is subjected to external stress. The sample axes are defined by an orthonormal set of basis vectors $[\mathbf{F}; \mathbf{a}_1]$, $[\mathbf{F}; \mathbf{a}_2]$ and $[\mathbf{F}; \mathbf{a}_3]$, collectively identified using a basis symbol ‘F’. The term “orthonormal” implies that the basis vectors are of unit magnitude and mutually perpendicular. The crystallographic axes of the i th austenite grain are similarly identified using the basis symbol F_i and its corresponding reciprocal basis by the symbol F_i^* .

When austenite transforms into martensite or bainite, there is a shape deformation which is an invariant–plane strain [1, 60, 61]. This change in shape can be represented by a 3×3 deformation matrix \mathbf{P} such that:

$$(\mathbf{F} \mathbf{P} \mathbf{F}) = \mathbf{I} + m[\mathbf{F}; \mathbf{d}](\mathbf{p}; \mathbf{F}^*) \quad (3.1)$$

where m is the magnitude of the shape deformation, $[\mathbf{F}; \mathbf{d}]$ is a unit vector in the direction of displacement and $(\mathbf{p}; \mathbf{F}^*)$ is the unit normal to the invariant–plane (i.e., the habit plane). There will in general exist 24 crystallographic variants of bainite or martensite in any given austenite grain, *i.e.*, 24 different invariant–plane strains.

Consider an arbitrary vector \mathbf{u} traversing a grain of austenite prior to transformation, as illustrated in Fig. 3.1a. This vector makes an intercept $\Delta\mathbf{u}$ with a domain of austenite that eventually ends up as a plate of bainite or martensite. As a consequence of the transformation, the vector \mathbf{u} becomes a new vector \mathbf{v} given by:

$$\mathbf{v} = \mathbf{P}\Delta\mathbf{u} + (\mathbf{u} - \Delta\mathbf{u}) \quad (3.2)$$

When considering the formation of large number of bainite/martensite plates in many austenite grains, \mathbf{u} traverses a polycrystalline sample of austenite

so this equation must be generalised as follows:

$$\mathbf{v} = \sum_{k=1}^n \sum_{j=1}^{24} \mathbf{P}_j^k \Delta \mathbf{u}_j^k + \left(\mathbf{u} - \sum_{k=1}^n \sum_{j=1}^{24} \Delta \mathbf{u}_j^k \right) \quad (3.3)$$

where $j = 1 \dots 24$ represents the 24 crystallographic variants possible in each austenite grain, and $k = 1 \dots n$ represents the n austenite grains traversed by the vector \mathbf{u} . In this scenario of a large number of bainite or martensite plates, it is assumed that the intercepts $\Delta \mathbf{u}_j^k$ can be approximated by $f_j^k \mathbf{u}$ where f_j^k is the fraction of sample transformed by variant j in austenite grain k .

The deformation caused by a particular plate j in austenite grain k , *i.e.*, $(\mathbf{F}_k \mathbf{P}_j \mathbf{F}_k) \equiv \mathbf{P}_j^k$ is known from the crystallographic theory originally developed for martensite [10, 21]. The remaining 23 such matrices for grain 1 of austenite can be deduced from this using symmetry operations. They can then be expressed in the reference frame of the sample using a similarity transformation as follows:

$$(\mathbf{S} \mathbf{P}_j^k \mathbf{S}) = (\mathbf{S} \mathbf{R} \mathbf{F}_k)(\mathbf{F}_k \mathbf{P}_j \mathbf{F}_k)(\mathbf{F}_k \mathbf{R} \mathbf{S}) \quad (3.4)$$

where $(\mathbf{S} \mathbf{R} \mathbf{F}_k)$ is the rotation matrix relating the basis vectors of the k th austenite grain to the sample axes, and $(\mathbf{F}_k \mathbf{R} \mathbf{S})$ is the inverse of that rotation matrix. In this way, the calculation described in equation 3.2 can be conducted in the sample frame of reference.

3.3 Variant Selection

Variant selection occurs because the shape deformation of a martensite or bainite plate may or may not comply with an external stress. Following [12], the compliance of a particular variant with the applied stress can be

expressed in terms of an interaction energy:

$$U = \sigma_N \delta + \tau s \quad (3.5)$$

where σ_N is the stress component normal to the habit plane, τ is the shear stress resolved on the habit plane in the direction of shear and δ and s are the respective normal and shear strains associated with transformation.

The applied system of stresses can be described by a 3×3 stress tensor σ_{lm} which when multiplied by the unit normal to the bainite/martensite habit plane gives the traction \mathbf{t} describing the state of stress on that plane. The traction can then be resolved into σ_N and τ in the normal manner [62]:

$$\begin{aligned} \sigma_N &= |\mathbf{t}| \cos\{\theta\} \\ \tau &= |\mathbf{t}| \cos\{\beta\} \cos\{\phi\} \end{aligned} \quad (3.6)$$

where $|\mathbf{t}|$ is the magnitude of \mathbf{t} , θ is the angle between the habit plane normal and \mathbf{t} , β the angle between \mathbf{t} and the direction of the maximum resolved shear stress, and ϕ the angle between the latter and the direction of shear for the bainite/martensite plate concerned. A positive U means that the bainite/martensite variant is favoured by the applied stress and *vice versa*.

The experiments reported here are based on stress-affected transformation, *i.e.*, the external stress was kept below the yield strength of the austenite at the temperature concerned. Plastic strain in the austenite can have other effects, for example the favouring of variants which grow across slip-planes and hence avoid mechanical stabilisation [26, 27]. However, it is not clear how these modes of variant selection would affect the transformation strain.

3.4 Generation of random and bias texture data

The relationship between the sample and crystal frames of reference can be described using Euler angles ϕ_1 , ϕ and ϕ_2 . These are the three angles by which the sample reference frame must be rotated in order to coincide with that of the crystal. The rotation matrix relating the frames is given by:

$$\begin{pmatrix} \cos\phi_1\cos\phi_2 - \sin\phi_1\cos\phi\sin\phi_2 & \sin\phi_1\cos\phi_2 + \cos\phi_1\cos\phi\sin\phi_2 & \sin\phi\sin\phi_2 \\ -\cos\phi_1\sin\phi_2 - \sin\phi_1\cos\phi\cos\phi_2 & -\sin\phi_1\sin\phi_2 + \cos\phi_1\cos\phi\cos\phi_2 & \sin\phi\cos\phi_2 \\ \sin\phi_1\sin\phi & -\cos\phi_1\sin\phi & \cos\phi \end{pmatrix} \quad (3.7)$$

To generate a random set of austenite grains, the angles ϕ_1 and ϕ_2 (ranging from 0 to 2π) and the value of $\cos\phi$ (between ± 1) are selected using a random number generator [63]. To simulate a polycrystalline state, a set of 500 austenite grains was assembled, each identified by a rotation matrix relating it to the sample frame. Fig. 3.2 shows the model generated $1\ 0\ 0_\gamma$ pole figure. The increase in the density at the middle of the pole figure is expected in a stereographic projection due to the angular distortion. The distribution of poles is otherwise random. This contrasts with the work of Han *et al.* [5, 6] where large regions of the stereogram were inexplicably left blank.

It is interesting to notice how the model fails to generate a random texture if the random rotation matrix is calculated for a polycrystalline specimen by using random numbers to generate a random rotation axis and a random rotation angle. The equation for generating rotation matrix using

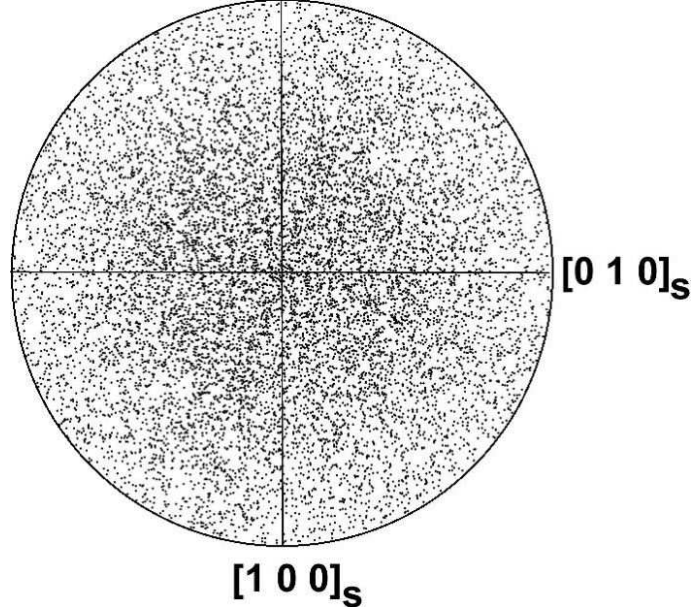


Figure 3.2: Model generated $1\ 0\ 0_\gamma$ pole figure for 1000 randomly orientated austenite grains.

this method is given below:

$$\begin{pmatrix} u_1u_1(1-m) + m & u_1u_2(1-m) + u_3n & u_1u_3(1-m) - u_1n \\ u_1u_2(1-m) - u_3n & u_2u_2(1-m) + m & u_2u_3(1-m) + u_1n \\ u_1u_3(1-m) + u_2n & u_2u_3(1-m) - u_1n & u_3u_3(1-m) + m \end{pmatrix} \quad (3.8)$$

where $\mathbf{u} = [u_1\ u_2\ u_3]$ is the rotation axis, θ is the rotation angle and $m = \cos\theta$ and $n = \sin\theta$. If \mathbf{u} and θ are generated using random numbers and it is used to generate $1\ 0\ 0_\gamma$ pole figure, it does not give a random texture (Fig. 3.3). The matrix described in Equation 3.7 will also not give a random texture (Fig. 3.4) unless $\cos\phi$ is generated randomly as described earlier.

Gamma textures are the Goss $\{1\ 1\ 0\}_\gamma\langle 0\ 0\ 1\rangle_\gamma$, Cube $\{1\ 0\ 0\}_\gamma\langle 0\ 0\ 1\rangle_\gamma$ and Copper $\{1\ 1\ 2\}_\gamma\langle 1\ 1\ \bar{1}\rangle_\gamma$ varieties [64–66]. These biased orientations were also generated in the austenite microstructure using a model. First, one austenite grain in an aggregate of 500 grains is introduced in such a

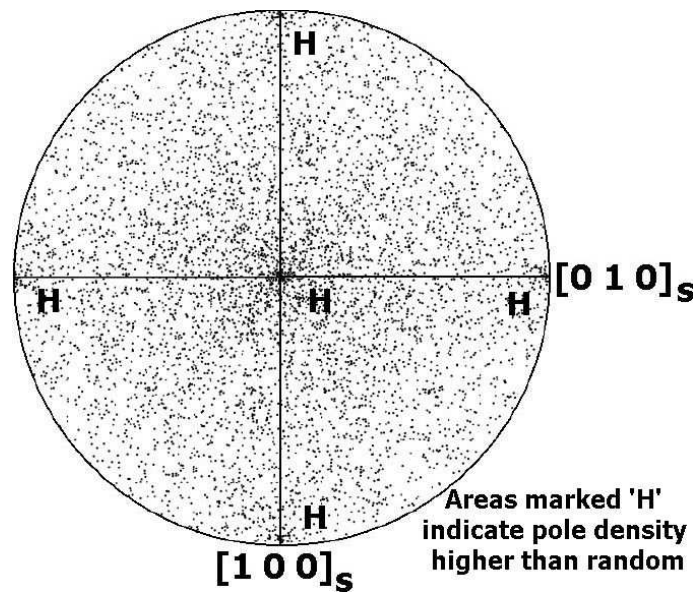


Figure 3.3: Model generated $1\ 0\ 0_\gamma$ pole figure for 1000 randomly orientated austenite grains generating orientation relationship following equation 3.8.

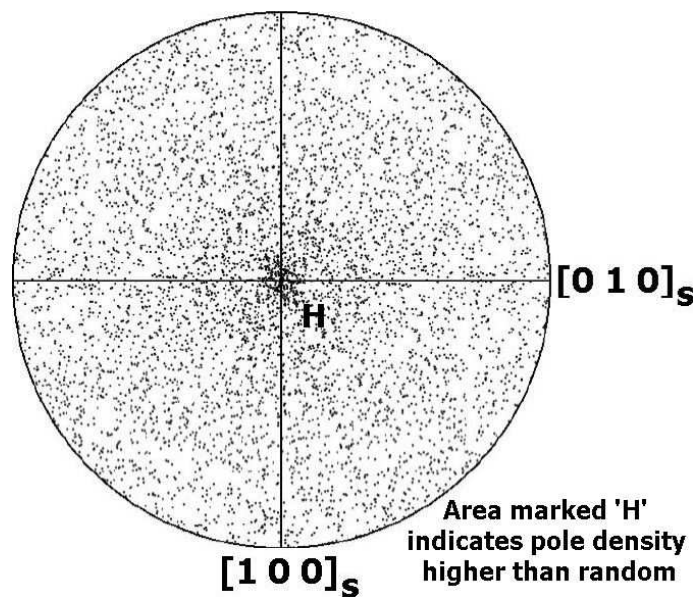


Figure 3.4: Model generated $1\ 0\ 0_\gamma$ pole figure for 1000 randomly orientated austenite grains after obtaining orientation relationship following equation 3.7 without generating $\cos\phi$ randomly.

manner that it exactly corresponds to one of the textures described above. For example in the Goss scenario:

$$[1\ 1\ 0]_{\gamma} \parallel [0\ 0\ 1]_S \quad [0\ 0\ 1]_{\gamma} \parallel [1\ 0\ 0]_S$$

Another 499 grains are then generated by randomly choosing rotation axes, but limiting the right-handed angle of rotation to the range 0–45° to avoid a random distribution. The model generated biased textures are shown in the form of $1\ 0\ 0_{\gamma}$ pole figures in Fig. 3.5.

3.5 Transformation strains

3.5.1 Uniaxial stresses

Although the method described in the preceding sections can be applied to calculate the transformation strain in both martensite and bainite, the results of the models are given for bainitic steels. In the following sections of this chapter the influence of various systems of stress and the nature of transformation strains in a polycrystalline sample of austenite is discussed.

The three sample axes are henceforth referred to as $[1\ 0\ 0]_S$, $[0\ 1\ 0]_S$ and $[0\ 0\ 1]_S$, where “S” is the basis symbol and it may be assumed that the stress is applied along $[1\ 0\ 0]_S$. The true strains are then calculated by examining how unit vectors along the sample basis vectors are stretched due to transformation. The true strain in each case is $\ln\{|\mathbf{v}|/|\mathbf{u}|\}$, where \mathbf{v} is the final and \mathbf{u} is the initial vector. This neglects rotation of vectors but in a polycrystalline sample the effect is negligible on average. Furthermore, the method is rigorously correct when the sample is constrained by a grip of a tensile testing machine, in which \mathbf{v} rotates to become parallel to \mathbf{u} . It is clear from Table 3.1 that the vectors \mathbf{u} and \mathbf{v} are always parallel if all the possible 24 variants are forming, but not so if only the most favoured variant forms.

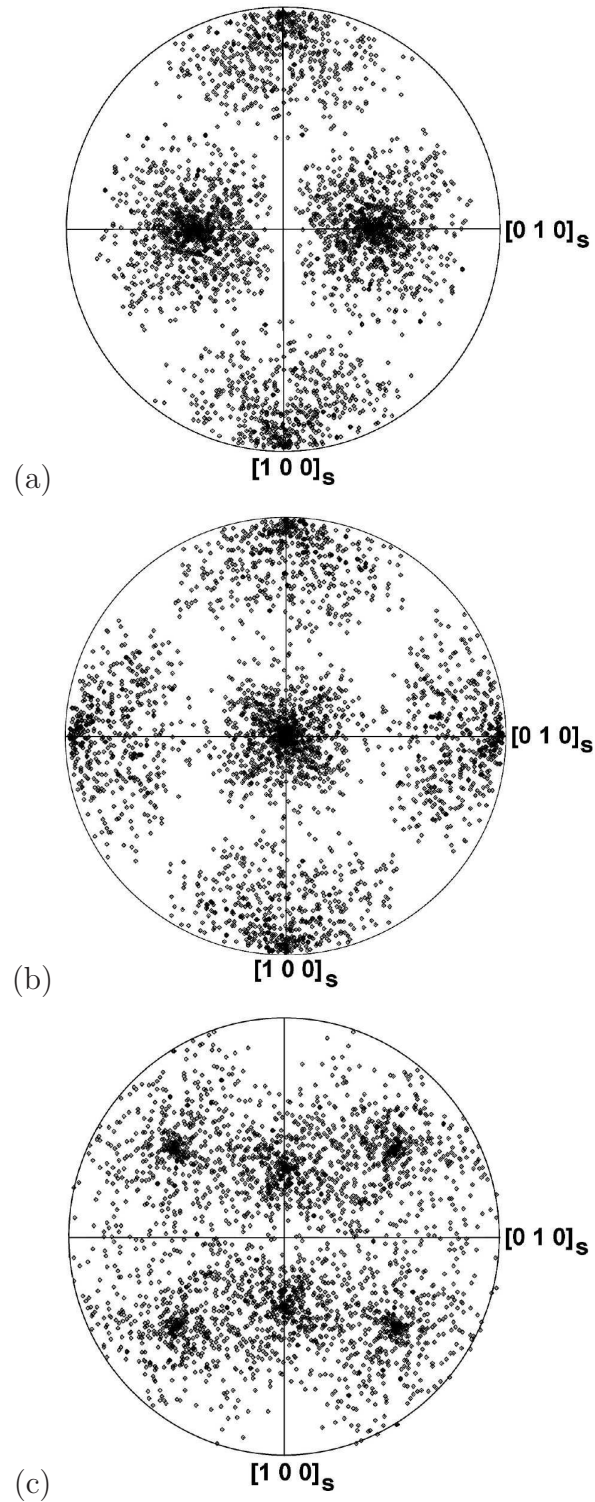


Figure 3.5: Calculated $1\ 0\ 0_\gamma$ pole figures for (a) Goss (b) Cube and (c) Copper textured austenite.

Table 3.1: Angle between vector \mathbf{u} and \mathbf{v} for various number of grains with different number of variants forming.

No. of grains	No. of variants	Angle between \mathbf{v} and \mathbf{u}
1	1	3.87°
	24	0°
10	1	0.30°
	24	0°
100	1	0.28°
	24	0°
300	1	0.21°
	24	0°
500	1	0.13°
	24	0°

On the other hand the, angle between \mathbf{v} and \mathbf{u} becomes very small as the number of grain increases.

Equation 3.6 was used to determine the interaction energy U of each bainite plate with the applied stress; the variants were then ranked in descending order of U . The transformation strain was then calculated for all 24 cases within a given austenite grain, beginning with the most favoured variant consuming the maximum fraction of austenite permitted – this fraction is 0.63 for the specific experiments analysed here [37]. Subsequent calculations assumed groups of most favoured variants forming in equal fractions up to the maximum allowed. The results are presented in Fig. 3.6 for uniaxial tension and compression.

It can be noticed that the strains need not be isotropic when variant selection occurs [16, 55, 67]. The variants are naturally selected in such a manner that the transformation strain supports the nature of the applied stress. Fig. 3.6a shows that the variant selection under tensile stress happens in such a manner that transformation strain becomes tensile in the direction

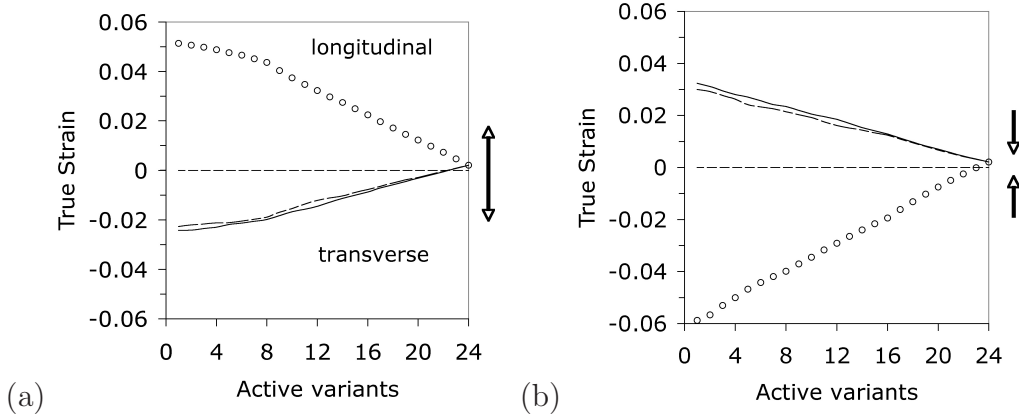


Figure 3.6: Strains developed due to transformation along the $[1\ 0\ 0]_S$ direction (labelled longitudinal, along the stress axis), and the transverse directions $[0\ 1\ 0]_S$ and $[0\ 0\ 1]_S$, (a) tensile stress, (b) compressive stress.

of applied load ($[1\ 0\ 0]_S$) and compressive in two transverse directions. A similar trend is observed when the applied load is compressive, the transformation strain in this case becomes compressive in $[1\ 0\ 0]_S$ direction and tensile in other two directions ($[0\ 1\ 0]_S$ and $[0\ 0\ 1]_S$) as shown in Fig 3.6b.

The true strain along $[1\ 0\ 0]_S$ is different between tension and compression mostly because the natural logarithm function scales the ratio of the initial to final length of $[1\ 0\ 0]_S$ differently depending on whether the ratio is greater or less than one. However, some difference is expected because unlike tension, the positive dilatational transformation strain opposes compression. When all 24 possible variants are allowed to form, the shear strains essentially cancel, so both cases lead to an almost isotropic expansion, Fig 3.6a and b. However, when variant selection occurs, none of the three directions show equal strain.

It is interesting to analyse the effect of prior austenite texture on transformation plasticity.

Fig. 3.7 shows the longitudinal strain along $[1\ 0\ 0]_S$ when polycrystalline samples of austenite undergo martensitic transformation under the influence

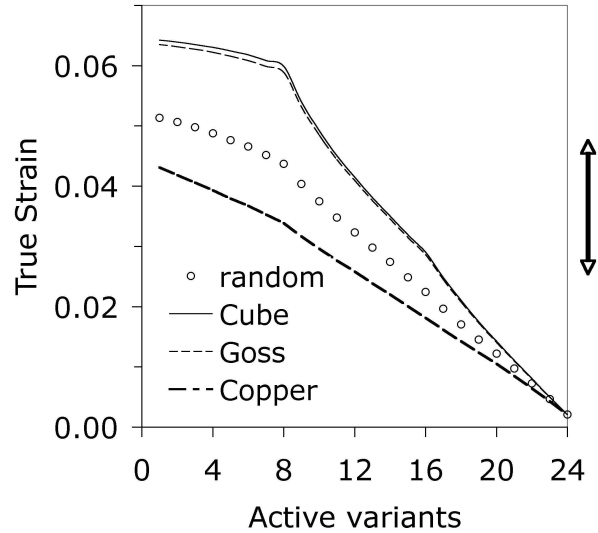


Figure 3.7: The longitudinal strain along $[1\ 0\ 0]_S$ when a polycrystalline sample of austenite undergoes displacive transformation (Table 3.2) under the influence of a uniaxial tensile stress. There are four different austenite textures represented, random, Goss, Cube and Copper.

of a uniaxial tensile stress applied along the same direction. The important observation is that the strain is larger when stress-affected transformation occurs in certain textured austenite (Goss or Cube) where as it is lower with some textures (Copper). This is not surprising since the elongation in this case would be like that from a single crystal of austenite. And the transformation strain in a single crystal depends on its orientation with the axis of the applied stress. It is shown in the Table 3.3 how the strain in a single crystal with Cube or Copper orientation varies with the number of active variants.

It is clear, that for a single crystal austenite with Copper orientation transformation strain is substantially lower than that of Cube orientation and that is what is reflected in the Fig. 3.7 for a polycrystalline material. For a randomly oriented single crystal the value would vary between a maximum (in this case Goss or Cube orientation) and a minimum (Copper orientation).

Table 3.2: The longitudinal strain along $[1\ 0\ 0]_S$ when a polycrystalline sample of austenite (500 grains) having Cube and Copper texture undergoes bainitic transformation under the influence of a uniaxial tensile stress. Each value corresponds to a particular number of active variants, with the first and the last one representing 1 and 24 active variants respectively.

Cube	0.064	0.064	0.064	0.063	0.062	0.062
	0.061	0.060	0.054	0.049	0.045	0.041
	0.038	0.035	0.032	0.029	0.025	0.021
	0.017	0.014	0.011	0.008	0.005	0.002
Copper	0.043	0.042	0.041	0.039	0.038	0.037
	0.035	0.034	0.032	0.030	0.028	0.026
	0.024	0.022	0.020	0.018	0.016	0.014
	0.012	0.011	0.009	0.006	0.004	0.002

Table 3.3: The longitudinal strain along $[1\ 0\ 0]_S$ when a single crystal sample of austenite with Cube and Copper orientation undergoes bainitic transformation under the influence of a uniaxial tensile stress. Each value corresponds to a particular number of active variants, with the first and the last one representing 1 and 24 active variants respectively.

Cube	0.075	0.075	0.073	0.072	0.072	0.073
	0.072	0.072	0.064	0.057	0.052	0.047
	0.043	0.040	0.037	0.035	0.029	0.024
	0.019	0.015	0.011	0.008	0.005	0.002
Copper	0.036	0.034	0.032	0.030	0.028	0.027
	0.026	0.024	0.023	0.022	0.020	0.019
	0.018	0.017	0.015	0.014	0.013	0.012
	0.010	0.009	0.007	0.006	0.004	0.002

When a large number of grains are considered for a randomly orientated sample the transformation strain will take a value that is in between these two limits as evident from Fig. 3.7.

3.5.2 Multiaxial Stresses

The cases considered above deal with uniaxial stress – there exist circumstances, for example when conducting welding, in which combinations of stresses are imposed during transformation. The system is then represented by a stress tensor σ_{lm} and the traction \mathbf{t} on any plane is then given in the usual way by the product of the tensor with the unit normal \mathbf{h} to the plane concerned. The traction can then be resolved into a normal and shear stress on the plane. The axes of the stress tensor correspond to those of the sample.

For a pure shear, $\sigma_{11} = -\sigma_{33}$ with all the other components of the tensor being zero. Fig. 3.8a shows the strains that develop in a polycrystalline sample of austenite subjected to pure shear. The anisotropy of strain is pronounced, with the minimum strain naturally along the $[0\ 1\ 0]_S$ direction. Notice that unlike ordinary plastic deformation, the strain along $[0\ 1\ 0]_S$ is non-zero. This is because the basic unit of deformation is not shear, but an invariant-plane strain with a finite volume change δ directed normal to the habit plane.

The case for hydrostatic compression ($\sigma_{11} = \sigma_{22} = \sigma_{33} < 0$) is illustrated in Fig. 3.8b. The shear component of the invariant-plane strain does not in this case interact with the pressure, so the only contribution to the transformation strain is from δ . This explains why the strains are about an order of magnitude smaller. However, the individual strains are still anisotropic since the volume expansion is directed normal to the habit plane of each plate.

Some specific experimental data on bainite will now be compared with the model results. Whereas the measured transformation strains are from

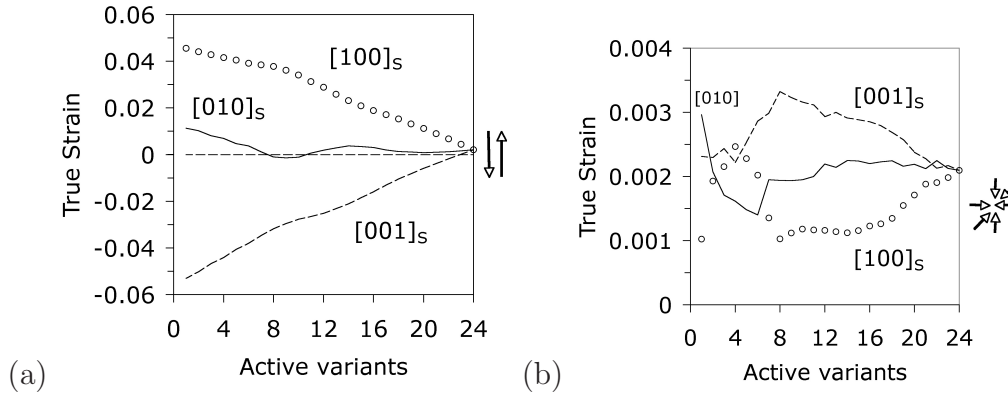


Figure 3.8: (a) Transformation strain when the specimen is subjected to pure shear. (b) The case for hydrostatic compression.

published work [37], the crystallographic measurements are new.

3.6 Comparison with experiments: Transformation Strain

Measured radial strains due to isothermal transformation to bainite under the influence of a stress are illustrated in Fig. 3.9 [37]. The maximum transverse strain at 200 MPa is 0.017 and that at 4 MPa is 0.004. The values of stress essentially correspond to transformation greatly influenced by stress and not affected, respectively. The strain data are macroscopic measurements made on polycrystalline samples of austenite. The data are therefore simulated by considering a cluster of 500 randomly oriented austenite grains, each of which makes a contribution to the overall strain during transformation.

The interaction energy for each of the 24 bainite variants, in each of the 500 austenite grains, is calculated for two different stress conditions in which the applied stress were compressive with a magnitude of 200MPa and 4 MPa respectively. The data were then arranged in descending order for each grain (as in Table 3.4 and Table 3.5). Of course, the most favoured variants

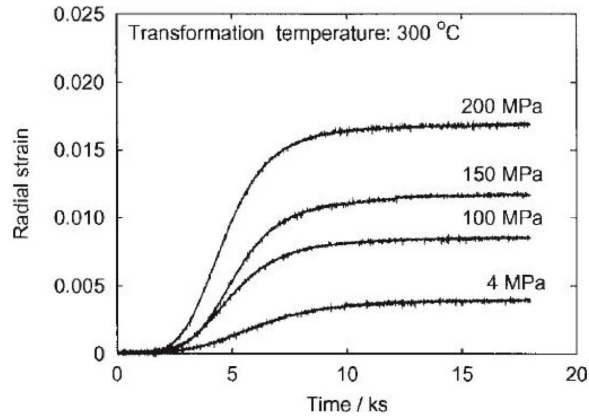


Figure 3.9: Radial strain for isothermal transformation at 300°C as a function of compressive stress [37].

and indeed the values of U will be different for each grain as a function of its orientation. But it then becomes possible to pick the n most favoured variants from each of the 500 grains in the descending arrays of U . Fig. 3.10 shows the calculated transverse strains to be expected when a number n of the most favoured variants form in each of the 500 austenite grains.

It is evident that the observed strains can be explained if it is assumed that between 12–14 of the most favoured variants form when transformation occurs under the influence of a large stress (200 MPa). By contrast, in the absence of a significant stress (4 MPa in this case), it is necessary to assume that most variants form, *i.e.*, there is almost no variant selection. From the data presented in Table 3.4, it is clear that the first 12–14 variants have higher values of positive (or very low negative) interaction energy and so these variants have higher probability of formation. Whereas Table 3.5 shows that the values of the interaction energy even for the most preferred variant is very low compared to the chemical driving force, which is 1225 J mol⁻¹ [37], so the extent of variant selection will be less and most of the variants will form. This is for why in this case the experimental strain matches with the model prediction when 22 out of total 24 variants are allowed to form (Fig.

Table 3.4: Interaction energy U (J mol^{-1}) for a uniaxial compressive stress of magnitude 200 MPa, for each of the 24 possible variants of bainite in three grains of austenite chosen arbitrarily from an aggregate of 500. The energies are arranged in descending order, with positive values corresponding to a favourable interaction with the applied stress and *vice versa*.

Grain 1		Grain 2		Grain 3	
Variant	U	Variant	U	Variant	U
2	126.4	15	112.8	6	137.1
10	126.4	9	91.8	15	133.6
21	108.8	13	81.3	14	115.7
20	108.8	11	63.2	9	110.7
3	48.3	6	61.4	16	89.4
8	48.3	12	40.6	12	89.2
23	30.7	1	26.9	7	71.8
18	30.7	14	26.3	1	70.0
19	26.1	16	20.1	22	37.4
24	26.0	5	8.1	13	31.4
17	-9.8	4	-0.7	24	25.1
22	-9.9	22	-7.3	11	18.7
11	-15.1	7	-7.8	17	-13.6
4	-15.2	23	-12.6	19	-15.4
13	-51.0	24	-29.3	5	-16.8
5	-51.0	21	-46.5	4	-18.2
16	-63.8	18	-48.7	8	-100.9
14	-63.9	8	-49.8	23	-103.4
7	-73.5	17	-53.5	10	-121.5
6	-73.5	19	-58.5	21	-124.4
9	-87.3	20	-73.3	3	-127.1
12	-87.5	3	-75.6	18	-128.5
15	-97.0	10	-87.6	2	-137.2
1	-97.1	2	-96.4	20	-138.2

Table 3.5: Interaction energy U (J mol^{-1}) for a uniaxial compressive stress of magnitude 4 MPa, for each of the 24 possible variants of bainite in three grains of austenite chosen arbitrarily from an aggregate of 500. The energies are arranged in descending order, with positive values corresponding to a favourable interaction with the applied stress and *vice versa*.

Grain 1		Grain 2		Grain 3	
Variant	U	Variant	U	Variant	U
1	3.0	23	3.1	8	3.0
7	2.7	13	3.0	3	2.7
12	2.7	18	2.8	22	2.5
16	2.3	11	2.8	24	2.0
14	2.1	5	2.5	17	1.9
9	2.1	21	2.5	10	1.9
15	1.8	20	2.3	2	1.7
6	1.7	4	2.3	19	1.5
5	0.9	8	0.5	23	1.0
4	0.7	15	0.5	18	0.8
17	0.4	3	0.4	6	0.3
19	0.2	9	0.4	14	0.0
13	-0.1	2	-0.1	21	-0.1
11	-0.1	1	-0.1	20	-0.1
24	-0.3	10	-0.1	7	-0.4
22	-0.3	12	-0.1	16	-0.4
18	-2.3	22	-2.9	13	-2.1
3	-2.5	6	-2.9	15	-2.4
20	-2.6	17	-3.1	5	-2.4
23	-2.8	16	-3.1	11	-2.6
2	-2.8	24	-3.2	12	-2.7
8	-2.9	14	-3.2	9	-2.8
21	-2.9	19	-3.3	4	-2.8
10	-3.0	7	-3.3	1	-1.4

3.10). However, the analysis leaves open the question of the degree of variant selection as a function of the magnitude of the applied stress. This is tackled next.

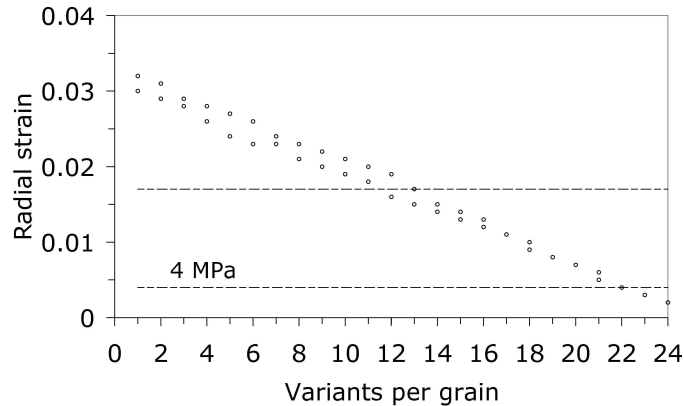


Figure 3.10: Radial strains for isothermal transformation at 300°C as a function of the number of most favoured variants allowed in each of 500 austenite grains. The measured strains are plotted as horizontal lines.

3.6.1 Extent of Variant Selection versus Stress

The total free energy available for transformation is the sum of chemical and mechanical components, the latter being zero in the absence of an applied stress during transformation:

$$\Delta G = \Delta G_{chem} + \Delta G_{mech} \quad (3.9)$$

It would be reasonable to assume that there is strong variant selection when the ratio of $\Delta G_{mech}/\Delta G$ is large. Given relevant dilatometric data, the extent of variant selection can be determined as in Fig. 3.10. The free energies can readily be calculated using standard methods.

Table 3.6 was compiled using data from the published literature. The data cover a pressure vessel steel [67], a low-temperature bainitic steel [37]

Table 3.6: Calculated data for a variety of steels. T is the transformation temperature and σ is the stress.

Reference	$T / ^\circ\text{C}$	σ / MPa	$U/\text{J mol}^{-1}$	ΔG_{chem} / J mol^{-1}	n	$\frac{\Delta G_{mech}}{\Delta G}$
Bhadeshia <i>et al.</i> [67]	400	98.4	61.84	1758	21	0.017
”	420	98.4	61.75	1620	20	0.019
”	440	98.4	61.67	1486	18	0.020
”	460	96.5	60.67	1354	19	0.022
”	400	41.5	26.08	1758	24	0.007
”	420	41.6	26.11	1620	24	0.008
”	440	41.4	25.95	1486	24	0.009
”	460	47.8	30.05	1354	23	0.011
Hase <i>et al.</i> [37]	300	-200	130.62	1225	12	0.051
”	300	-150	97.97	1225	16	0.038
”	300	-100	65.31	1225	19	0.026
Matsuzaki <i>et al.</i> [16]	450	-25	29.69	1199	23	0.006
”	450	-50	14.84	1199	20	0.012

and a high-silicon steel [16].

It is evident from Fig. 3.11 that there is a strong linear correlation between the ratio $\Delta G_{mech}/\Delta G$ and the number of most favoured variants allowed to form in each of the austenite grains. This is an important observation in that it allows for the first time the extent of variant selection, and hence the transformation strains, to be calculated as a function of stress for any steel.

3.7 Stress-free Transformation from austenite

In their classic work on the stress-free transformation to bainite, Davenport and Bain in 1930 [68] noticed that “the volume change (due to transformation) is not necessarily uniformly reflected in linear change in all dimensions”.

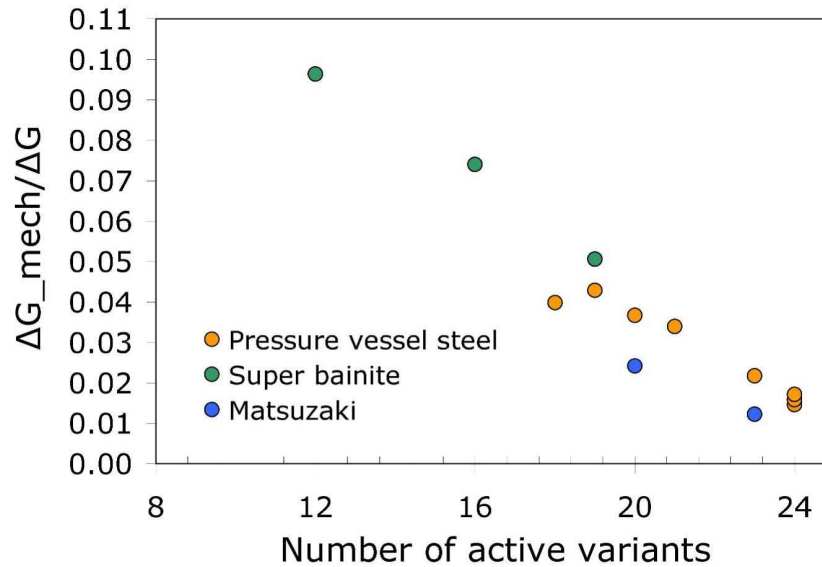
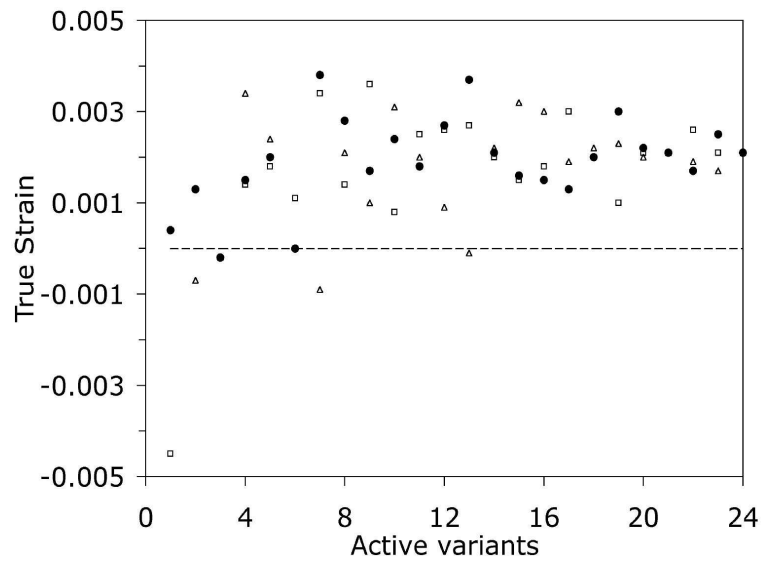


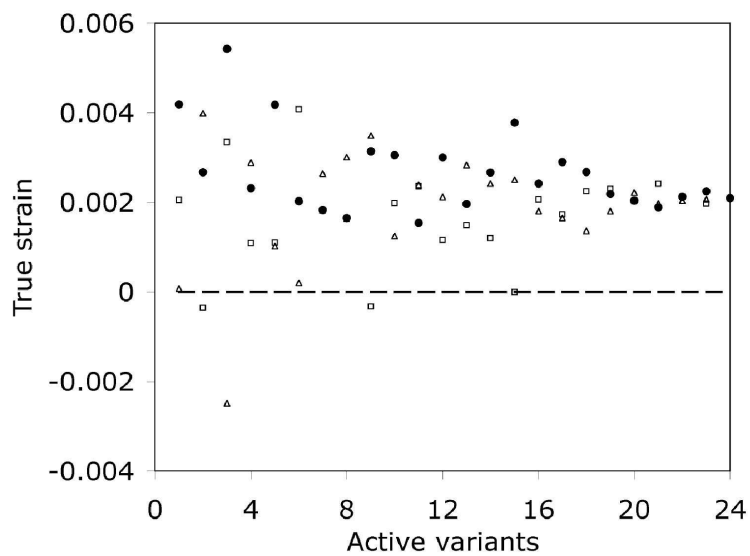
Figure 3.11: $\Delta G_{mech}/\Delta G$ versus the number of most favoured variants per grain (n), for a variety of steels.

They even found that the thickness of a flat disc specimen actually decreased as the volume increased! Bhadeshia *et al.* found a similar effect and explained it qualitatively in terms of transformation from textured austenite [67].

Fig. 3.12 shows calculated strains along three orthogonal directions for a cluster of 100 austenite grains having a Cube texture (Fig. 3.12a) or random orientation (Fig. 3.12b) which transform to bainite, as a function of the number of variants that form. It is evident that in both the cases the transformation strain might be negative in certain directions (which means compression along that direction) when the number of variants form is less than the maximum possible 24 variants. This explains Davenport and Bain's observations if the number of variants that form in the austenite is limited, which might occur because the special grain boundaries present in such austenite limit the variants of bainite that can nucleate.



(a)



(b)

Figure 3.12: Transformation strains observed in three arbitrarily chosen perpendicular directions when (a) Cube textured (b) randomly orientated austenite transforms into bainite under no applied stress.

3.8 Summary

A theory has been compiled for calculating the macroscopic strains which develop when polycrystalline samples of austenite are transformed into bainite or martensite under the influence of applied stress or a system of stresses or without any applied stress. Indeed, the theory can be applied to any scenario where the shape deformation due to displacive transformation is defined.

There is one approximation in the method described in this chapter. It has been assumed that in a polycrystalline sample the state of stress in any particular grain does not affect the state of stress of the other grains. Although in stricter sense that will never be the case in practice. But for the sake of simplification it has been assumed that there is no interaction between the various grains in the microstructure.

The transformation strain has been observed to be anisotropic when there is variant selection during transformation. However, when all the variants form, transformation strain becomes same as the volume strain.

It has been shown that there is a direct correlation between the nature of the transformation strain with the nature of the applied stress. In case of a compressive stress the variants are selected in such a way that the transformation strain becomes compressive in the direction of applied stress and tensile in two transverse directions. The opposite trend is observed when transformation occurs under a tensile load.

The model is developed in such a way that it is capable of taking into account any texture that is present in the austenite prior to transformation. It has been shown that the prior texture present in the microstructure has a strong influence on the transformation strain. This observation is significant, as the transformation strain plays an important role in determining the mechanical properties like fatigue strength or residual stress in a welded joint. Comparisons with experimental data on a bainitic steel are encouraging.

One of the most interesting outcomes of this work is that a strong correlation has been obtained between the proportion of the driving force attributed to stress, and the extent of variant selection. The correlation is entirely expected when it is considered that the driving force has both chemical and mechanical origins, and hence can be used quantitatively to estimate transformation plasticity.

The model seems to also be able to explain an experimental observation made long ago, which showed that during bainite transformation, although there is a net volume expansion, the length of the specimen in one direction might be decreased. The model explains this observation and shows this is possible when transformation occurs from both textured and randomly orientated austenite with some limitations in the total number of variants that can form. The limitations in the number of variants forming could be due to the presence of some special grain boundaries.

The theory developed here will be used in the next chapter to develop another model capable of explaining the experimentally observed texture of bainite obtained when transformation occurs under stress.

Chapter 4

Transformation texture: Single crystal analysis

4.1 Introduction

Crystallographic texture is said to exist when a polycrystalline material has a non-random distribution of crystal orientations relative to the sample axes. This phenomenon is of particular importance in the processing and properties of steels. Texture can arise in many ways but the topic of interest here is that which develops as a consequence of the displacive transformation of austenite. There have been previous studies on the calculation of textures in these circumstances, but they involve a variety of assumptions which prevent rigorous predictions.

As has been discussed in Chapter 3, when transformation occurs under the influence of stress certain variants of martensite/bainite are favoured out of all that might possibly occur [12]. This gives rise to the formation of crystallographic texture. In this chapter, suitable crystallographic theory [10, 11, 21] and data have been used to identify the favoured variants during bainite formation from stressed austenite and then pole figures obtained

4.2 Orientation relationship between martensite and austenite 65

from those variants are compared with the corresponding experimental data obtained from electron back scattered diffraction patterns. The results are obtained assuming a single crystal austenite. The experiments discussed are based on stress-affected transformation, *i.e.*, the external stress was kept below the yield strength of the austenite at the temperature concerned. Plastic strain in the austenite can have other effects, for example the favouring of variants which grow across slip-planes and hence avoid mechanical stabilisation [26, 27]. Such effects become particularly prominent at large strains [28] but might be neglected when the debris associated with plasticity is insufficient to hinder the progress of the growing plates. For example, it has been shown that when an austenitic stainless steel is elongated by 10% and then transformed to martensite, the resulting crystallographic texture can nevertheless be calculated using the variant selection criterion inherent in equation 3.5 of Chapter 3.

4.2 Orientation relationship between martensite and austenite

It is important to define the crystallographic relationship $(\alpha \text{ J } \gamma)$ between the parent austenite and the martensite. If $(\gamma \text{ S } \gamma)$ is the matrix representing the total transformation strain then it can be shown [13] that:

$$(\alpha \text{ J } \gamma)(\gamma \text{ S } \gamma) = (\alpha \text{ C } \gamma) \quad (4.1)$$

where $(\alpha \text{ C } \gamma)$ is the Bain correspondence matrix. It follows that:

$$(\alpha \text{ J } \gamma) = (\alpha \text{ C } \gamma)(\gamma \text{ S } \gamma)^{-1} \quad (4.2)$$

$(\gamma \text{ S } \gamma)$ can be determined as shown in [13]. The Bain correspondence matrix can, for example be expressed in the austenite reference frame as:

$$\begin{pmatrix} 1 & \bar{1} & 0 \\ 1 & 1 & 0 \\ 0 & 0 & 1 \end{pmatrix}$$

It is known that in the cubic crystal system there are 24 symmetry elements, each of which can be represented by a matrix. So there are 24 $(\alpha \text{ J } \gamma)$ matrices, determined by multiplying $(\alpha \text{ J } \gamma)$ with each of the symmetry matrices in turn. Associated with each $(\alpha \text{ J } \gamma)$ will be a variant of the habit plane and displacement vectors.

4.3 Methodology for drawing pole figure

Pole figures are drawn in the sample reference frame so an orientation relationship must be defined between the sample axes and those of the austenite crystals, labelled as $(\text{S J } \gamma)$ where ‘‘S’’ is the sample basis. If the $\{h \ k \ l\}$ pole figure of ferrite (martensite) is to be drawn, then each $\{h \ k \ l\}$ pole of martensite must be expressed in the austenite frame and then in the reference frame of the sample. Writing the pole as $(\mathbf{h}; \alpha^*) = (h \ k \ l)$, $(\mathbf{h}; \gamma^*) = (\mathbf{h}; \alpha^*)(\alpha \text{ J } \gamma)$ and this is repeated for 24 variants of \mathbf{h} . To convert the indices to the sample reference frame $(\mathbf{h}; \text{S}^*) = (\mathbf{h}; \gamma^*)(\gamma \text{ J } \text{S})$. This procedure must be repeated for each martensite plate within the same austenite grain. For example, there are 6 $\{1 \ 0 \ 0\}$ poles per plate so if the total number of plates within one γ grain is n then the number of poles becomes $6n$.

4.4 Determination of matrix (S J γ)

First the $1\ 0\ 0_\gamma$ pole figure of an austenite crystal is experimentally determined, which is shown in Fig. 4.1. Only three poles are shown here because the figure is from the lower hemisphere.

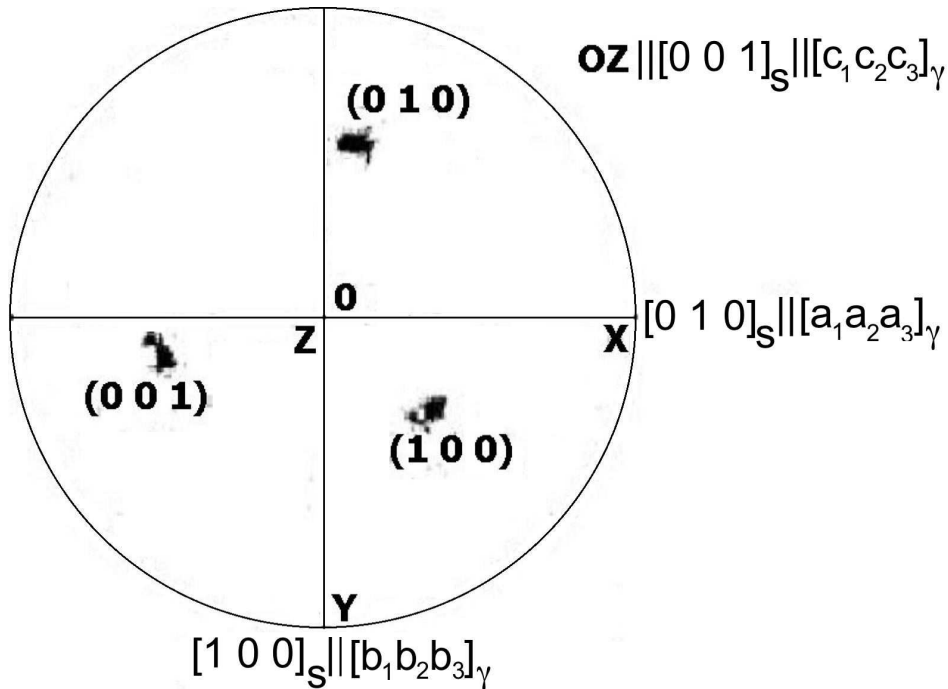


Figure 4.1: $1\ 0\ 0$ pole figure of austenite.

In the second step the angles between the $\{1\ 0\ 0\}$ poles and the sample axes are measured to determine the vectors **a**, **b** and **c** from the direction cosines, and the rotation matrix, (S J γ), is calculated using the procedure described in [13]. The geometry needed to plot the pole figure is illustrated in Fig. 4.2.

“C” corresponds to the centre of the stereographic sphere. The intersection of a pole from a crystal located at the centre, with the sphere is then projected through the north or south poles. The resulting projection on the equatorial plane defines the position of that pole on the stereogram.

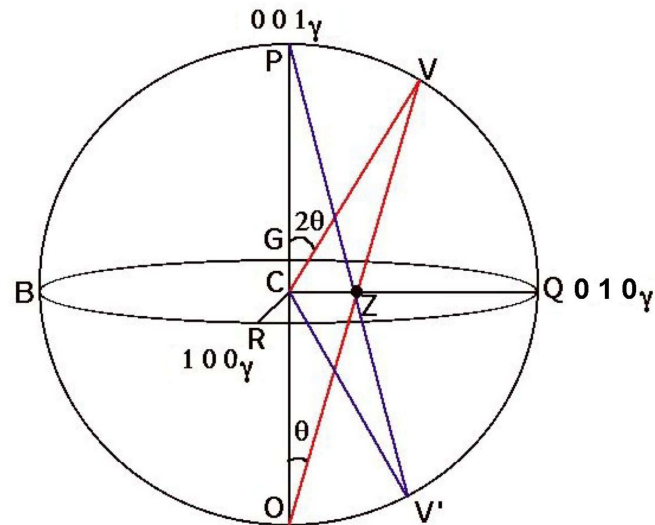


Figure 4.2: Construction of pole figure in gamma reference frame.

All the above discussion is for a single crystal of γ , but the principles are identical when dealing with a polycrystalline sample.

4.5 Data

The transformation texture can in principle be calculated from the knowledge of the initial texture of austenite, and by taking into account variant selection due to the applied stress. But in doing so, it is important to realise that the shape deformation, habit plane and orientation relationship of any particular plate of bainite are mathematically connected by the crystallographic theory [10, 21]. A complete set of crystallographic data is therefore necessary before rigorous calculations can be attempted. Unfortunately, such data are frequently not available, so one purpose of the present work was to study the sensitivity of the texture predictions relative to the crystallographic inputs and the accuracy of routinely available experimental techniques.

The set of data designated (i) in Table 4.1 refer those used to model

the martensitic transformation texture in an austenitic stainless steel (results described in the next chapter), but adapted using the theory described in [13] for the lattice parameters of interest in the present work, *i.e.*, $a_\gamma = 0.3619$ nm and $a_\alpha = 0.2882$ nm [37]. This results in a macroscopic transformation–strain which is a shear of 0.2292 and a dilatational strain of 0.01 normal to the habit plane. The maximum fraction of bainite possible in the alloy system studied, for a transformation temperature of 300°C, is 0.63 [37].

The analysis that follows assumes the first set of data listed in Table 4.1 to describe the displacive transformation to bainite. The remaining data will be discussed towards the end of the chapter to illustrate the sensitivity of the calculations to crystallographic characteristics.

4.6 Comparison with experiments: Variant selection

Bainite was formed in a high carbon steel under uniaxial compressive load in a thermo–mechanical simulator (*Thermecmaster Z*) following the experimental procedure described in [37]. The specimens were later studied metallographically on their longitudinal sections, and subjected to electron backscattered diffraction (EBSD) in a Hitachi S–4300 and JEOL, JXA6400 scanning electron microscope with a step size of 0.25 μm .

Fig. 4.3 is an orientation image of a sample transformed to bainite under the influence of a uniaxial compressive stress. The colours represent crystallographic orientation using a standard technique called electron backscatter diffraction (EBSD) [74–76]. The rectangles mark particular grains of austenite which were subjected to detailed analysis.

The crystallographic data from the EBSD analysis can be represented on stereographic projections in two common ways, by plotting the raw poles or by using pole–density contours on the projections. Both methods are

Table 4.1: Sets of crystallographic data. (i) The first set was used by [69] to successfully estimate the martensitic transformation texture of austenitic stainless steel, but adjusted for the lattice parameters relevant here – the habit plane is close to $\{2\ 9\ 5\}_\gamma$. Although there are no complete data available for the bainitic steel analysed in the present work, the first set is the most appropriate given the approximate habit plane recently reported for the same steel by [70]. The other two sets correspond to what are conventionally referred to as (ii) $\{2\ 5\ 2\}_\gamma$ [71], and (iii) $\{3\ 15\ 10\}_\gamma$ [72, 73] habits. Each set describes the features of a single plate. γ and α refer to austenite and bainite respectively.

	Habit plane \mathbf{p}_γ	Shape change (γ P γ)
(i)	$\begin{pmatrix} -0.168640 \\ -0.760394 \\ -0.627185 \end{pmatrix}$	$\begin{pmatrix} 0.992654 & -0.033124 & -0.027321 \\ 0.026378 & 1.118936 & 0.098100 \\ -0.027321 & -0.123190 & 0.898391 \end{pmatrix}$
(ii)	$\begin{pmatrix} 0.362929 \\ 0.853900 \\ 0.373011 \end{pmatrix}$	$\begin{pmatrix} 0.986887 & -0.030853 & -0.013478 \\ 0.040751 & 1.095879 & 0.041883 \\ -0.051772 & -0.121809 & 0.946790 \end{pmatrix}$
(iii)	$\begin{pmatrix} -0.169270 \\ -0.761321 \\ -0.625890 \end{pmatrix}$	$\begin{pmatrix} 0.992602 & -0.033274 & -0.027355 \\ 0.026503 & 1.119202 & 0.097997 \\ -0.027355 & -0.123033 & 0.898853 \end{pmatrix}$
	Orientation (γ J α)	
(i)	$\begin{pmatrix} 0.575191 & 0.542067 & 0.097283 \\ -0.550660 & 0.568276 & 0.089338 \\ -0.008610 & -0.131800 & 0.785302 \end{pmatrix}$	
(ii)	$\begin{pmatrix} 0.584634 & 0.519305 & 0.119189 \\ -0.529661 & 0.583719 & 0.059597 \\ -0.046858 & -0.118861 & 0.813418 \end{pmatrix}$	
(iii)	$\begin{pmatrix} 0.575371 & 0.542097 & 0.097510 \\ -0.550726 & 0.568476 & 0.089244 \\ -0.008855 & -0.131888 & 0.785465 \end{pmatrix}$	

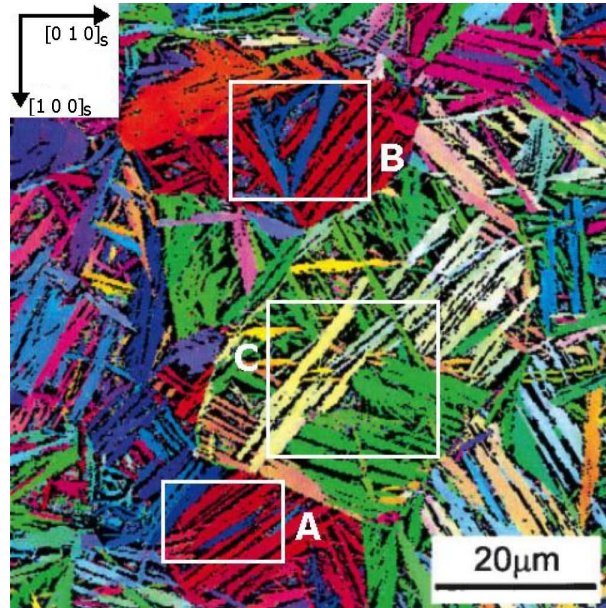


Figure 4.3: All Euler image. The colours represent different crystallographic orientations.

used here for illustrative purposes. The predicted pole figures are presented using open circles for each variant and superimposed on the experimental pole figures for easy comparison.

Considering the austenite in grain A first, the $1\ 0\ 0_\gamma$ pole figure is shown in Fig. 4.4a,b. There is a clear spread in the orientation of the austenite grain, presumably due to strains caused by transformation. It is well known that the formation of bainite introduces dislocation debris in the adjacent austenite [61, 77]. The plotting of pole-density contours somewhat exaggerates the spread in orientation, as can be seen by comparing Fig. 4.4a,c with Fig. 4.4b,d. This is because the latter are produced using data binned into 5° bins with gaussian smoothing.

Table 4.2 lists the interaction energies between the bainite variants and the applied stress, with a positive energy denoting a favourable interaction. There are, therefore, 12 favoured variants, within which the first eight are in

Table 4.2: Interaction energy U (J mol^{-1}) for a uniaxial compressive stress of magnitude 200 MPa, for each of the 24 possible variants of bainite in three grains of austenite. The energies are arranged in descending order, with positive values corresponding to a favourable interaction with the applied stress and *vice versa*. Rank 1 in this listing corresponds to the most favoured variant.

Ranking	1	2	3	4	5	6	7	8
	9	10	11	12	13	14	15	16
	17	18	19	20	21	22	23	24
Grain A	151.2	144.2	133.4	124.6	111.6	111.1	95.7	93.9
	35.6	26.7	24.4	15.7	-7.8	-7.8	-10.9	-12.2
	-126.8	-131.7	-139.0	-145.1	-147.3	-148.8	-152.8	-153.0
Grain B	152.2	151.8	150.4	149.8	143.5	142.9	141.4	141.0
	12.8	12.8	10.9	10.7	10.5	10.3	8.4	8.4
	-167.0	-167.3	-168.8	-169.3	-173.9	-174.5	-175.9	-176.3
Grain C	139.6	128.0	95.4	73.1	71.8	65.9	64.6	64.0
	63.2	38.9	4.1	0.9	-4.8	-21.1	-40.0	-40.5
	-64.1	-83.7	-96.1	-98.6	-110.1	-119.3	-119.8	-126.7

a class of high values of U with the remainder with much smaller positive interaction energies.

It is clear from Fig. 4.4e, which compares experimental versus calculated data, that allowing the eight most favoured variants explains the major intensities in the experimental data. Allowing all 12 of the favoured variants (Fig. 4.4f) completes the match between the calculated data, and all positions on the stereogram where measured intensity exists. It is interesting that the addition of a further four favoured variants with lower values of U in Fig. 4.4f explains the residual lowest-intensity components of the experimental data.

Fig. 4.5 shows reasonable agreement between the experimental data and calculations for grain B. The high intensity areas designated ‘H’ correspond the eight most favoured variants, whereas those designated ‘L’ are of lower

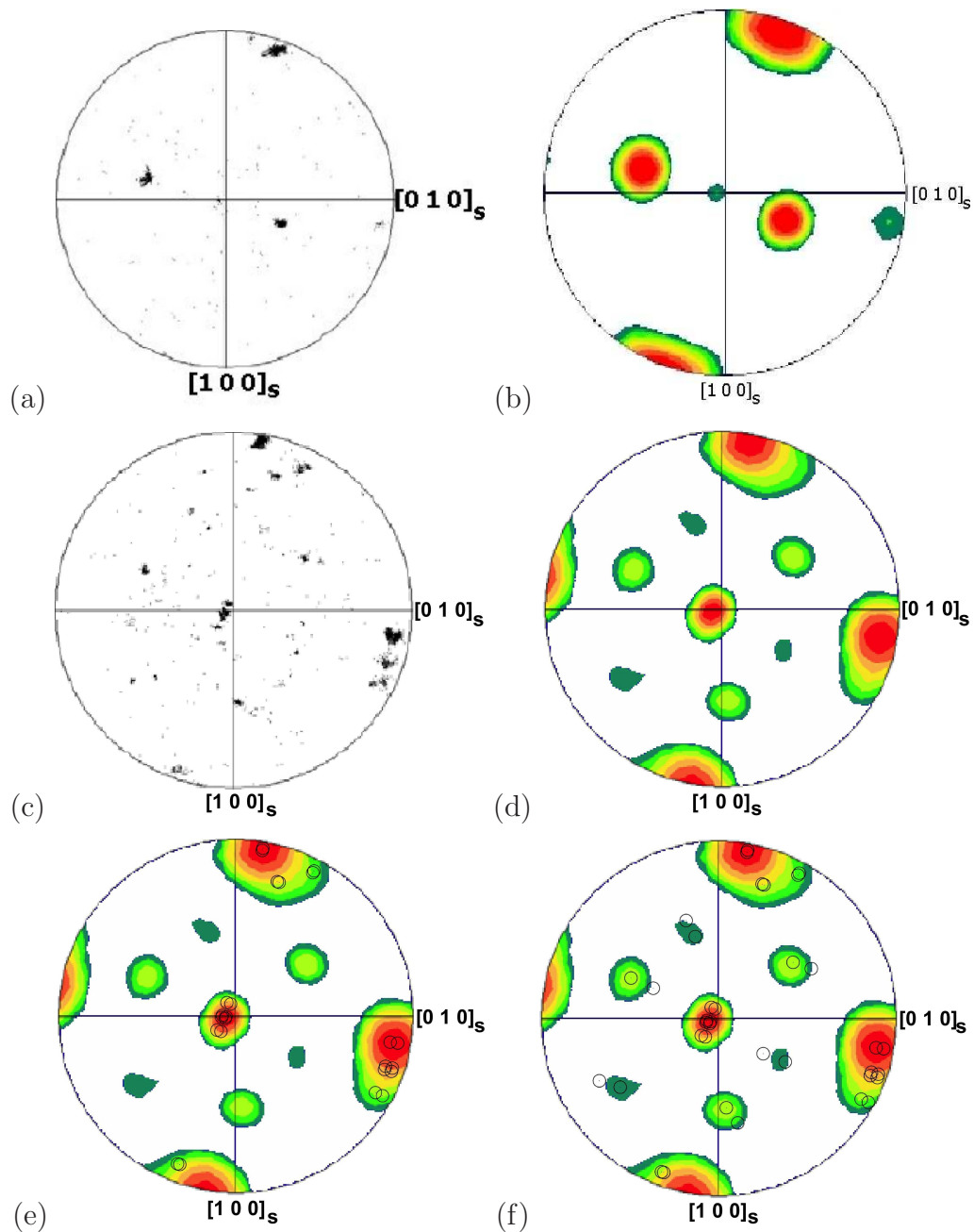


Figure 4.4: Pole figures for grain A, relative to the sample frame of reference. (a,b) $1\ 0\ 0_\gamma$ pole figures, (c,d) $1\ 0\ 0_{\alpha'}$ pole figures. (e) Comparison with calculated $1\ 0\ 0_{\alpha'}$ pole figures, allowing the 8 most favoured variants to form. (f) Comparison with calculated $1\ 0\ 0_{\alpha'}$ pole figures, allowing the 12 most favoured variants to form.

intensity and are explained by the next four less favoured variants listed in Table 4.2. This confirms that the strongest intensities observed correspond to the most favoured variants.

Grain B happens to be roughly in Goss orientation relative to the sample axes. For this orientation, a different transformation texture has been demonstrated both by measurement and by calculation when martensite is induced by *tensile deformation* [8, 69], compared with that illustrated in Fig. 4.5c,d. To explain this, the transformation textures were calculated for both compression (consistent with the present experiments) and tension, for an austenite grain in the exact Goss orientation. The results are illustrated in Fig. 4.6a,b which shows that both the tensile [8, 69] and compression data can be explained by the present model by assuming the formation of all twelve of the favoured variants.

The result from grain C needs special discussion – the interaction energies are again listed in Table 4.2. A maximum of twelve favoured variants can form, but it is not possible to explain all of the observed intensity using the 12 variants for which $U > 0$, Fig. 4.7. There are some low-intensity regions which are not explained. These discrepancies indicate additional variants which are not favoured by the applied stress. Fig. 4.7 confirms that the low-intensity regions correspond to the two variants with interaction energies of -4.8 and -21.1 J mol^{-1} , *i.e.*, the unfavourable variants with the least interaction with the applied stress.

The formation of unfavourable variants with low interaction energies is easy to understand when it is realised that at the transformation temperature of 300°C , the chemical free energy change is about -1225 J mol^{-1} [37], a value much greater than the magnitude of U . This chemical driving force can therefore stimulate transformation even though it opposes the applied stress.

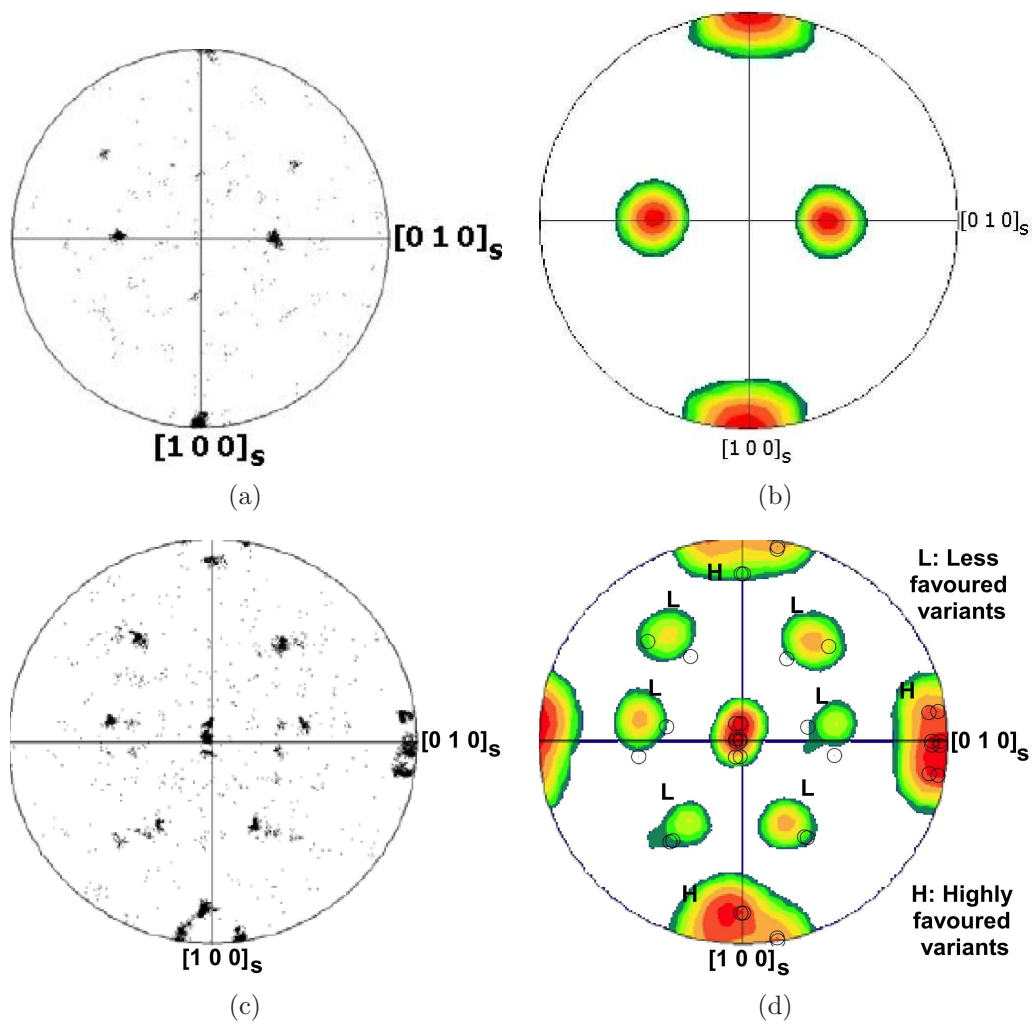


Figure 4.5: Pole figures for grain B, relative to the sample frame of reference. (a,b) $1\ 0\ 0_\gamma$ pole figures, (c) $1\ 0\ 0_{\alpha'}$ pole figure. (d) $1\ 0\ 0_{\alpha'}$ pole figure with calculated data superimposed.

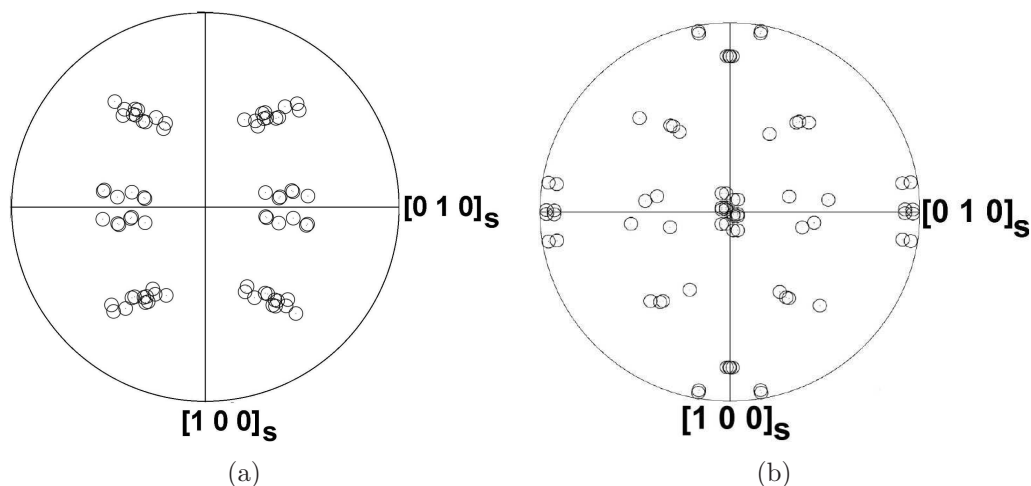


Figure 4.6: Calculated $1\ 0\ 0_{\alpha'}$ pole figures relative to the sample frame of reference, showing the twelve most favoured variants of bainite. (a) Tensile and (b) compressive uniaxial stress. In this figure poles are allowed to form from both hemispheres.

4.7 Observed variant intensities and relation to interaction energies

A favoured crystallographic variant is one for which the interaction energy with the applied stress is positive, *i.e.*, its macroscopic transformation strain complies with that stress. The purpose here is to demonstrate that favoured variants correspond to the highest observed intensities. Fig. 4.3 shows the three grains from which EBSD data were collected to produce the pole figures.

An attempt is made in this section to show conclusively that the observed diffraction intensities can only be systematically explained by the selection of those variants which comply best with the applied stress during transformation.

Additional work has been done to clarify the plot in Fig. 4.3. Although it has been argued in the previous section that in grain A (Fig. 4.3) 12 variants are favoured, it is not clear from Fig. 4.3 that in grain A, there are indeed 12 variants, because the All Euler photograph is not clear on that

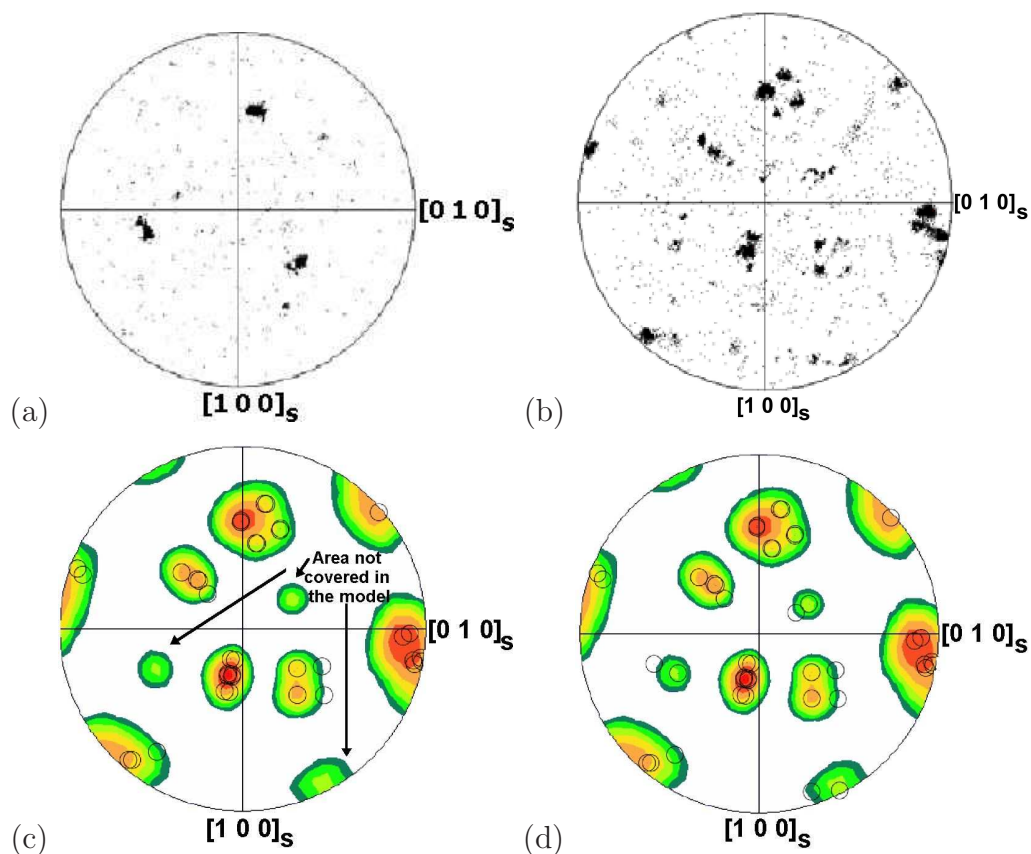


Figure 4.7: Pole figures for grain C, relative to the sample frame of reference. (a) $1\ 0\ 0_\gamma$ pole figures, (b) $1\ 0\ 0_{\alpha'}$ pole figure. (c) $1\ 0\ 0_{\alpha'}$ pole figure with calculated data superimposed for the 12 most favoured variants. (d) $1\ 0\ 0_{\alpha'}$ pole figure with calculated data superimposed for the 14 most favoured variants.

aspect.

Figs 4.8 and 4.9 show that it is not possible to explain all the observed intensities without allowing all the twelve favoured variants to form in grain A. Note that in the EBSD analysis presented there, it is not possible to distinguish closely oriented bainite variants. To further analyse the data, the closely oriented variants (8 variants in each group) are clubbed together in groups of similar orientation for the purposes of variant–selection analysis. It is noted that the 24 variants fall into 3 groups of eight each with very similar

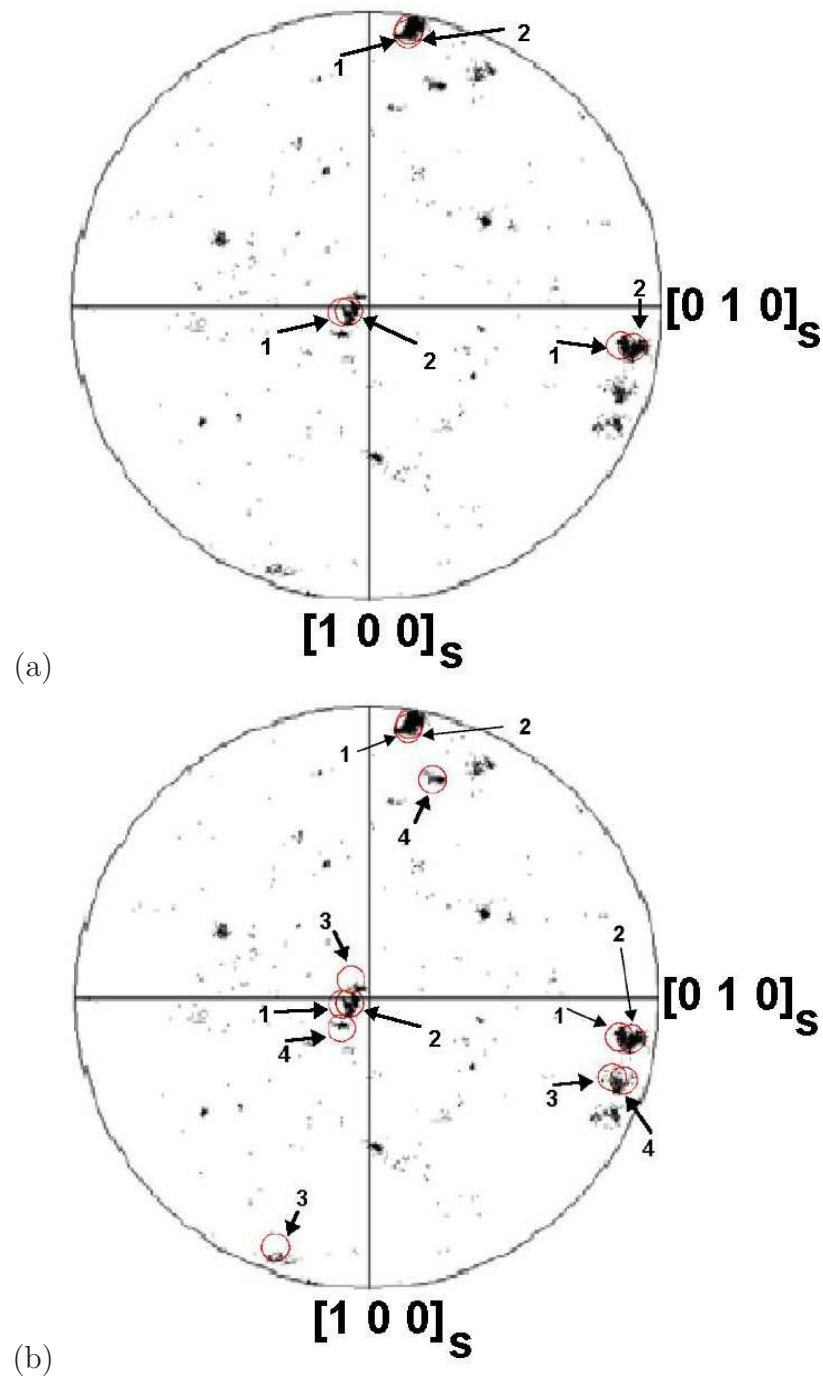


Figure 4.8: $100_{\alpha'}$ pole figure from grain A. Red circles are model predictions. Comparisons with the experimental pole figures is made allowing (a) 2, (b) 4 most-favoured variants to form in the model.

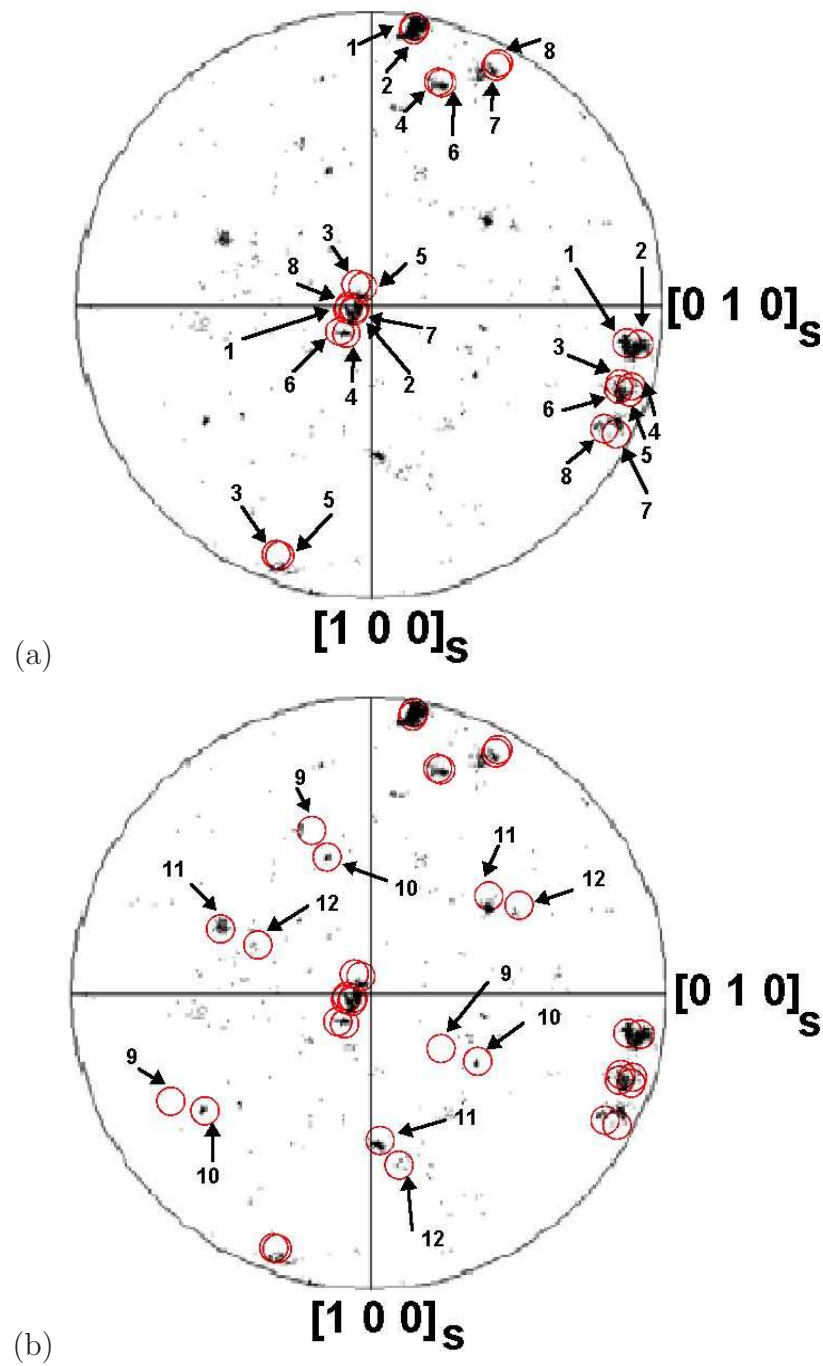


Figure 4.9: $100_{\alpha'}$ pole figure from grain A. Red circles indicate model predictions. Comparisons with the experimental pole figures is made allowing (a) 8 and (b) 12 most-favoured variants to form in the model.

orientations. These are designated X, Y, Z. The 8 most favoured variants all lie in group X (only in case of grain C, 6th most favoured variant lie in group Y) and the remaining 16 are distributed between the other groups. The interaction energies for all 24 variants in the three grains from Fig. 4.3 are given in Table 4.2.

From Figs 4.10, 4.11 and 4.12, it is evident that the high intensity regions of the experimental pole figures consistently correspond to the variants with the greatest interaction energies, orientations designated X. The interaction energies plotted in the bar charts therein represent the average interaction energy for that cluster of variants. The average interaction energy for each cluster can be deduced from Table 4.2. For example, in Fig. 4.10 the average interaction energy for the cluster “X” orientations is 121 J mol^{-1} , which is the average of the interaction energies of the first 8 most favoured orientations listed for grain A in Table 4.2.

In summary, whilst it has not been possible to isolate the intensities corresponding to each individual crystallographic variant within a given austenite grain, the work does clearly establish that the largest observed intensities do indeed correspond to the most favoured variants.

4.8 Sensitivity to Crystallographic Data

It is a fact that detailed crystallographic data of the kind listed in Table 4.1 are few and far between. However, a large number of ferrous alloys fall roughly within the range of the three sets in Table 4.1 [1, 73]. It is instructive therefore to analyse the sensitivity of the calculated texture to the data. Fig. 4.13 shows the analysis for grain B. A comparison of the stereograms shows that the texture is reasonably predicted for all three sets, although there are detailed differences for the $\{2\ 5\ 2\}_{\gamma}$. These differences are important if the accuracy of the experimental technique is greater. Large numbers of

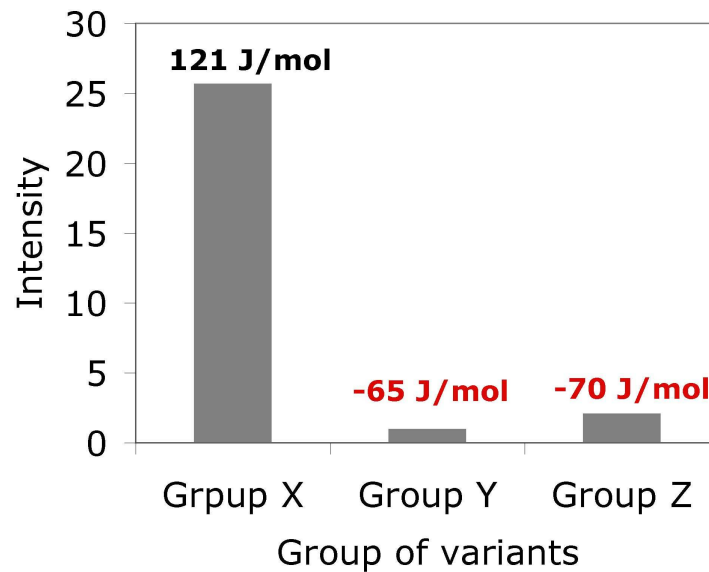
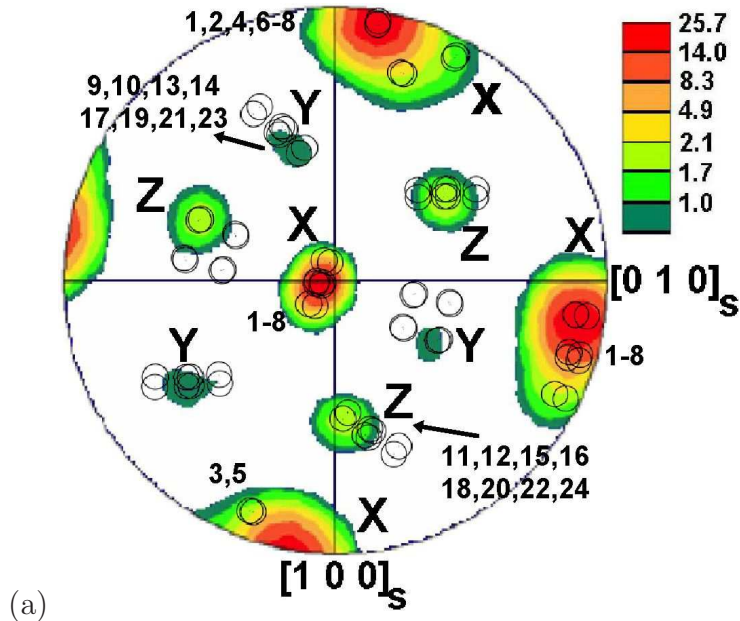


Figure 4.10: $100_{\alpha'}$ pole figure from grain A. There are total 24 variants, which includes both favoured and unfavoured variants. (a) The poles are grouped into three regions, X, Y and Z. The numbers indicate variant rankings as listed in Table 4.2. The colours are indicative of the intensities of poles. (b) Bar chart showing the intensity as a function of region, and the average interaction energy for that region (Table 4.2).

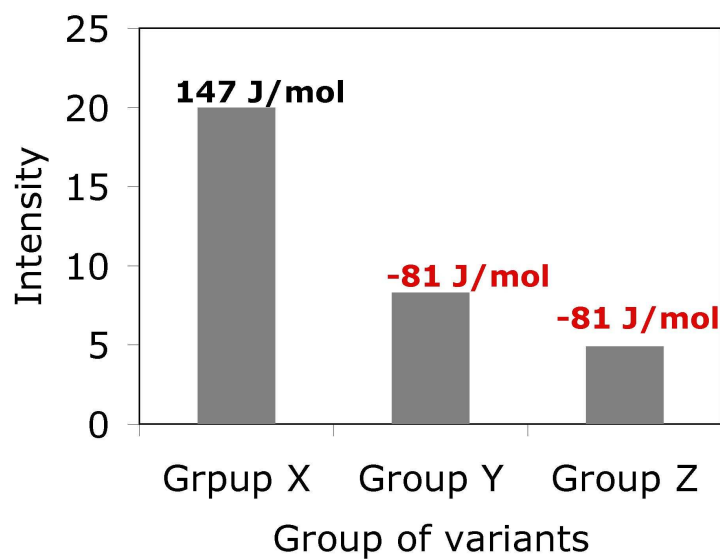
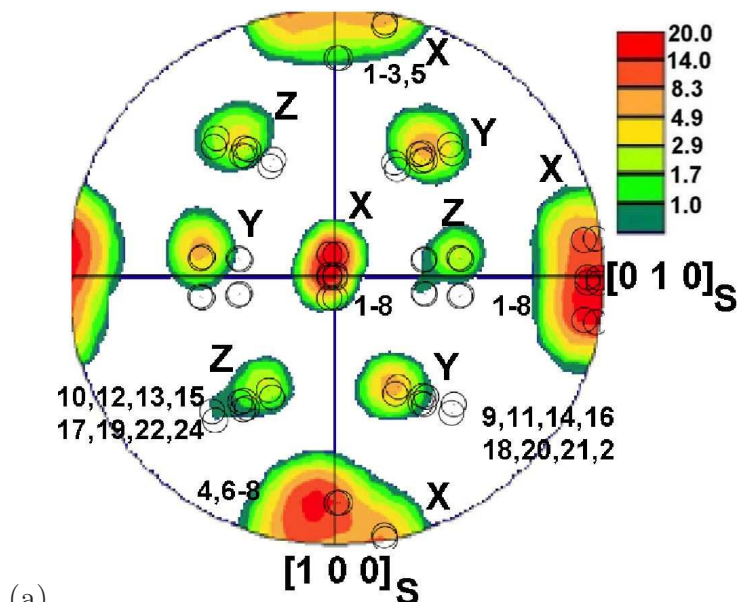
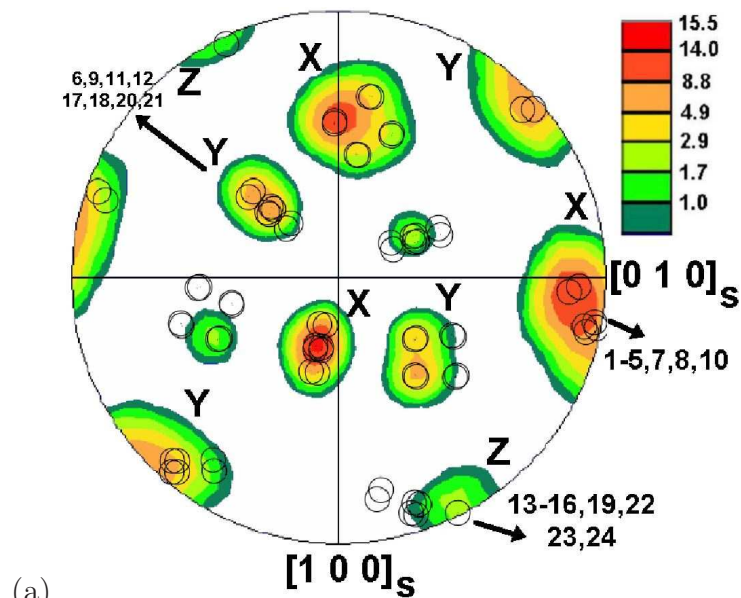
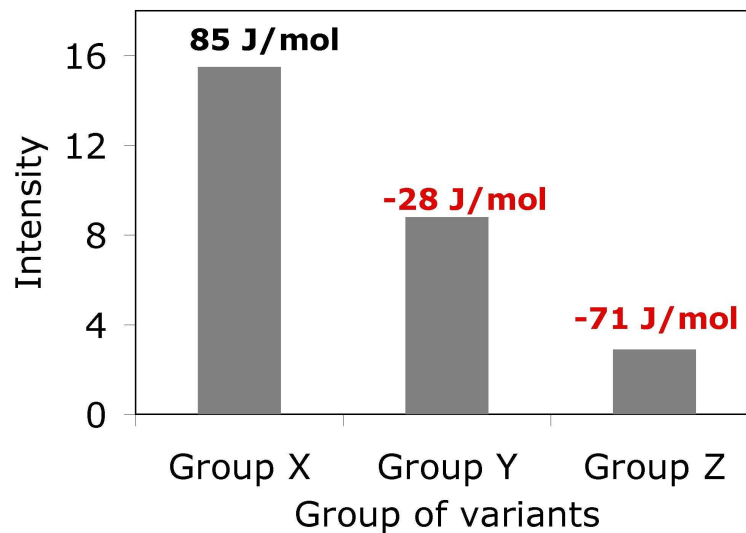


Figure 4.11: $100_{\alpha'}$ pole figure from grain B. There are total 24 variants, which includes both favoured and unfavoured variants. (a) The poles are grouped into three regions, X, Y and Z. The numbers indicate variant rankings as listed in Table 4.2. The colours are indicative of the intensities of poles. (b) Bar chart showing the intensity as a function of region, and the average interaction energy for that region (Table 4.2).



(a)



(b)

Figure 4.12: $100_{\alpha'}$ pole figure from grain C. There are total 24 variants, which includes both favoured and unfavoured variants. (a) The poles are grouped into three regions, X, Y and Z. The numbers indicate variant rankings as listed in Table 4.2. The colours are indicative of the intensities of poles. (b) Bar chart showing the intensity as a function of region, and the average interaction energy for that region (Table 4.2).

accurate measurements can indeed be made, as demonstrated by [22] with respect to the orientation relationship between the austenite and martensite but such accuracy is not common, particularly when EBSD measurements are reported. There also is a need for complete crystallographic measurements of the shape deformation, habit plane and orientation relationship of the transformation products in the new steels.

4.9 Summary

A theory has been compiled for calculating the crystallographic texture which develops when austenite is transformed into bainite or martensite under the influence of applied stress. Indeed, the theory can be applied to any scenario where the shape deformation due to displacive transformation is defined. The orientation of the prior austenite grain has been shown to be very important in determining the texture of the product phase.

Comparisons of the model predicted pole figure with experimental ones on a bainitic steel are encouraging. It has been shown that when transformation occurs under the influence of stress only, the variant selection criteria follows the theory given by Patel and Cohen [12].

It has been shown theoretically how the reversal of sign in the applied stress, will change the texture of bainite or martensite. It has also been proved that the variant selection will be more prominent from the pole figures, when transformation occurs under tensile stress than compressive stress.

Analysis has been presented to show that the arcs of highest intensity in the pole figures consistently correspond to the variants having highest interaction energies. This conclusively proves that the variant selection model presented here is sound.

The results shown in this chapter indicate that change in crystallographic data set, which comprises of habit plane, displacement direction,

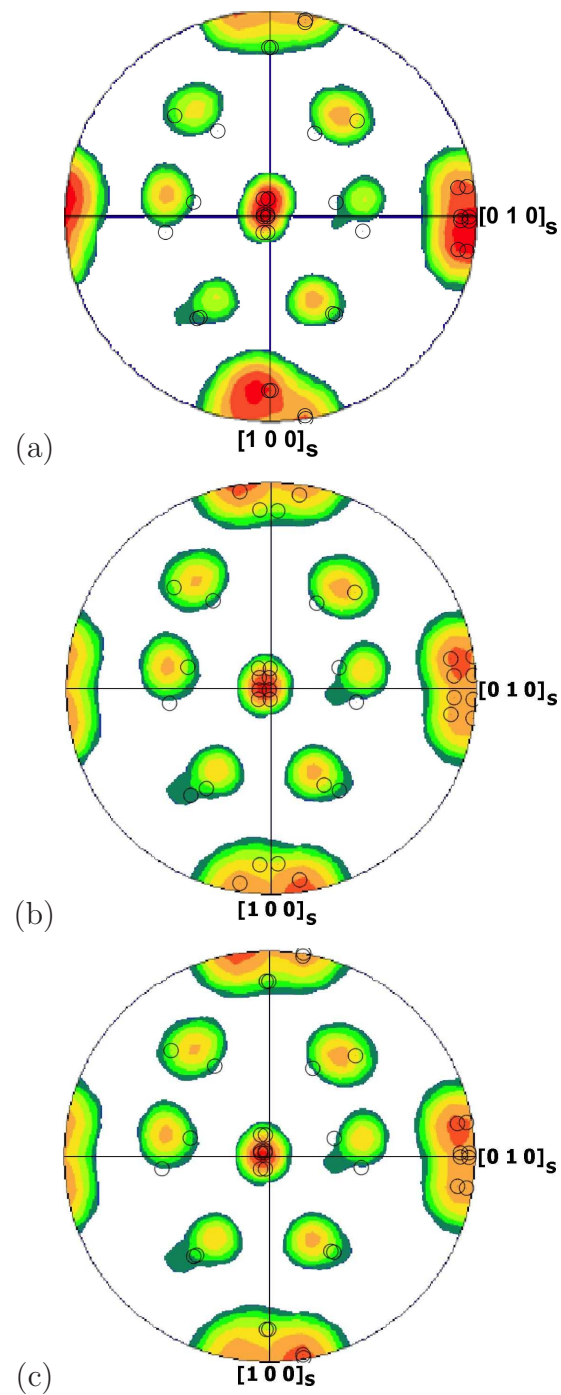


Figure 4.13: $1\ 0\ 0_{\alpha'}$ pole figures for grain B, assuming crystallographic data corresponding to the following approximate habit planes (Table 4.1): (a) $\{2\ 9\ 5\}_\gamma$ (reproduced from Fig. 4.5d), (b) $\{2\ 5\ 2\}_\gamma$, (c) $\{3\ 15\ 10\}_\gamma$.

orientation relationship matrix (between product and parent phase) and the shape deformation matrix, has little effect on the crystallographic texture. A theoretical comparison of pole figures of bainite calculated using three different data set shows minor difference in texture.

Chapter 5

Texture of martensite formed from plastically deformed austenite

5.1 Introduction

Displacive transformation is influenced by externally applied stress as described in Chapter 3 and 4. However, the effect of prior strain on displacive transformation is not fully understood. The austenite may be considered to be plastically deformed but eventually stress-free. Alternatively, it may have experienced deformation and be under the influence of external stress. Stress or strain can of course influence variant selection and hence crystallographic texture.

A more subtle effect is that the austenite may acquire a deformation texture prior to transformation, in which case this will influence the development of transformation texture. This second effect is easy to deal with but the role of plastic strain in the austenite in determining transformation texture is not all that clear. Understandably this is an aim of this chapter.

5.2 Experimental Procedure

5.2.1 Tensile Tests

A Fe-30Ni-0.3C (wt%) steel was studied because it is austenitic at room temperature and hence can be easily deformed prior to transformation. Tensile specimens were prepared as shown in Fig. 5.1. These were then sealed in quartz tubes filled with argon and given a homogenising treatment for 48 hours at 1200°C. This results in a coarse austenite grain size, Fig. 5.2, and a further treatment is needed to reduce the size. This was achieved by cooling the coarse grained samples in liquid nitrogen to form martensite and then re-austenitising at 900°C for 20 min to form finer austenite grains. The samples were air cooled from 900°C. The fine grains are conducive to texture analysis.

Samples for electron back scattered diffraction (EBSD) analysis were prepared by straining to 20% elongation in tension (“Schenck” 50 kN Electric Screw Machine). They were then unloaded and transferred into liquid nitrogen to form martensite from plastically deformed austenite but without any influence of applied stress. Such samples are designated “30Ni-Strain”.

To form martensite under the influence of both stress and strain, a special experimental set-up was designed as shown in Fig. 5.3. A rubber disc was press-fitted onto the tensile specimen (Fig. 5.3a) and then one of the two grips of the specimen was inserted into a plastic container (Fig. 5.3b) through a hole at its base. The hole was then blocked by the rubber disc to make the container water-proof, and the assembly was connected to a tensile testing machine in the usual manner. The cross head movement was kept at 0.1 mm s⁻¹. After 20% elongation with the specimen still under stress liquid nitrogen was poured into the container to induce martensite. These samples were designated “30Ni-Stress”, containing martensite formed under the influence of both stress and plastic strain. The sample was then unloaded

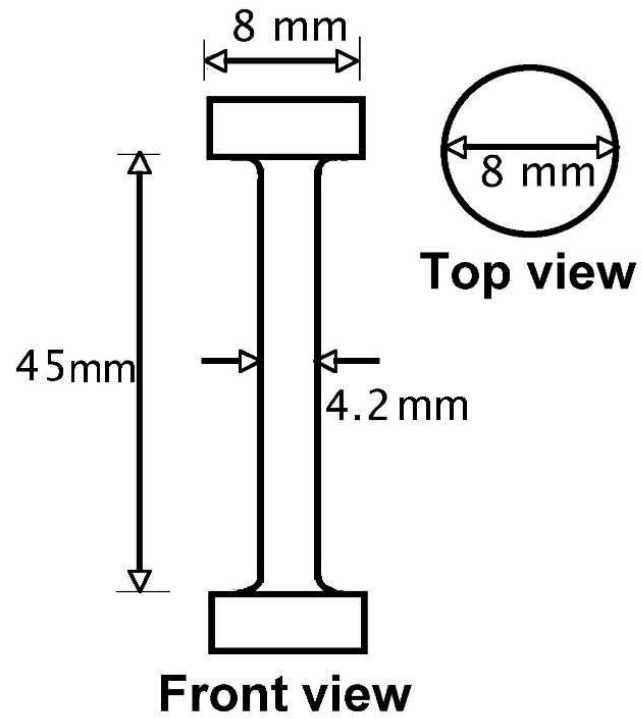


Figure 5.1: Diagram of the tensile specimen.

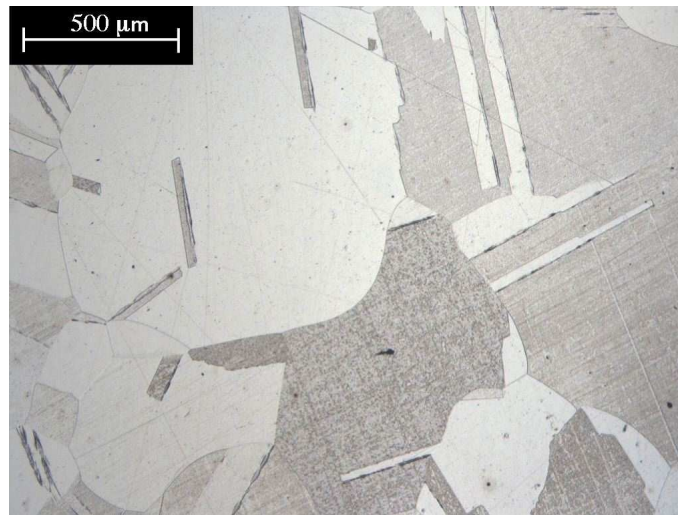


Figure 5.2: Microstructure of austenite after homogenising treatment.

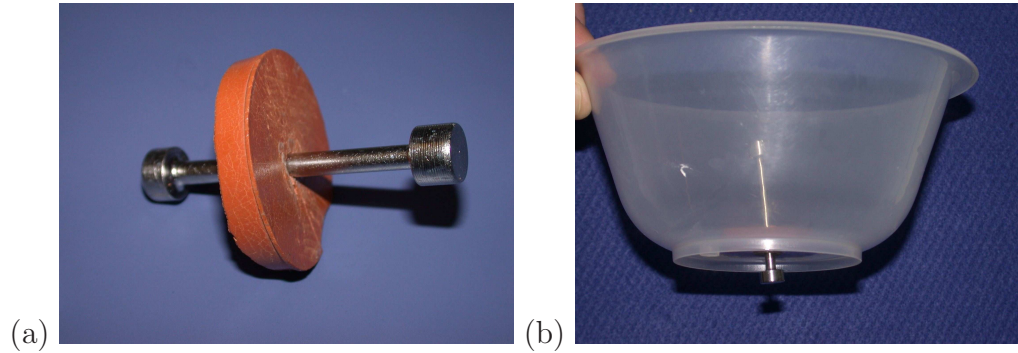


Figure 5.3: (a) Tensile specimen fitted with the rubber disc. (b) Tensile specimen in a water-proof plastic container.

for further studies.

5.2.2 EBSD analysis

Samples were cut from the tensile test specimens as shown in Fig. 5.4.

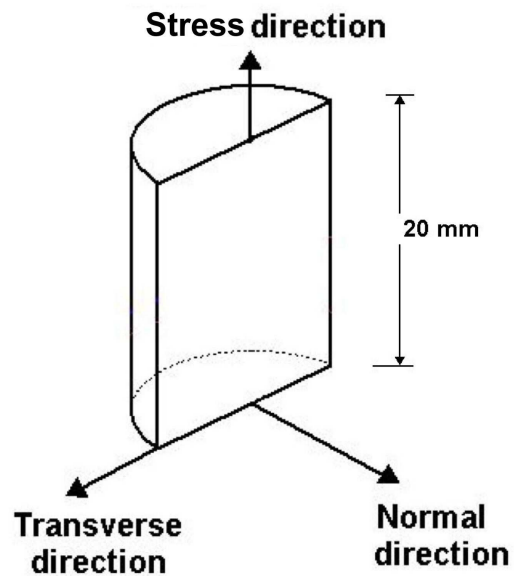


Figure 5.4: Dimension of the EBSD specimen cut from a tensile sample.

Variant selection is probably best studied by mapping the distribution of crystallographic orientations. Therefore, samples were prepared for electron backscattered diffraction (EBSD) analysis in an orientation imaging scanning electron microscope at Tata Steel in India. The samples were prepared as for optical microscopy, but then polished again using a colloidal silica solution for 30 min for a better finish and to minimise the influence of any stressed surface layer. An EBSD analyser (make:HKL) attached with a scanning electron microscope (JEOL, JXA6400) was used for the crystallographic studies with a step size of $0.5 \mu\text{m}$, a minimum of $600 \times 120 \mu\text{m}$ area was scanned for each specimen. The data were analysed using the ‘Channel 5’ software to construct experimental pole figures.

In the next two sections the applied stress direction is expressed in the sample reference frame as $[1\ 0\ 0]_S$ and the transverse direction in the same reference frame is represented as $[0\ 1\ 0]_S$.

5.3 Pole figures from single crystals of γ

In this section the predicted pole figures are presented using open circles for each variant and superimposed on the experimental pole figures for easy comparison.

5.3.1 Analysis of “30Ni-Stress”

Fig. 5.5 shows the “All Euler” photograph of the scanned area from the sample 30Ni-Stress. An “all Euler” photograph gives useful information about the orientation difference of a phase (in this case γ) at various places in the microstructure. Thus it can be useful in determining the prior austenite grain boundaries as different austenite grain areas would be shown in different colours. The pole figures were measured from the two grains A and B. The macroscopic stress tensor acting on these grains was assumed to be

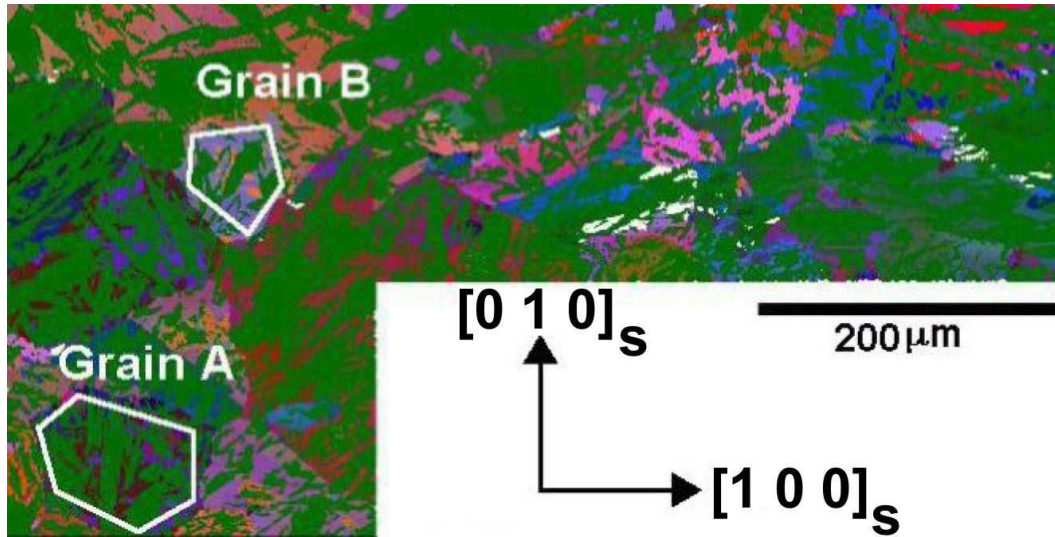


Figure 5.5: All Euler image from EBSD analysis of the sample “30Ni-Stress”. Pole figures were computed from the two grains marked as ‘A’ and ‘B’.

purely tensile, for calculating the interaction energies associated with each variant using the Patel and Cohen method. The orientation relationship matrix between the sample and the crystal axes was determined following the procedure described in section 4.4. Fig. 5.6a shows the measured $1\ 0\ 0_{\alpha'}$ pole figure of Grain A and Figs 5.6b and 5.6c show the model predictions superimposed on the experimental data assuming 12 and 18 most favoured variants.

From Table 5.1 it can be seen that there are 12 variants which have positive interaction energies. However if only these are allowed to form then not all the observed areas of intensity are explained (Fig. 5.6b). To recover consistency it was found necessary to use 18 variants including six which do not comply with the stress.

This is not unreasonable given the large chemical driving force associated with forming martensite in liquid nitrogen. In these circumstances it is possible to induce unfavourable variants. Nevertheless the regions of greatest

Table 5.1: Interaction energy U (J mol⁻¹) for a uniaxial tensile stress of magnitude 300 MPa, for each of the 24 possible variants of martensite in grain A and grain B of alloy 30Ni-Stress. The energies are arranged in descending order, with positive values corresponding to a favourable interaction with the applied stress and *vice versa*.

Grain A		Grain B	
Variant	U	Variant	U
22	271.0	19	277.6
17	268.2	24	268.0
6	267.6	14	249.2
16	265.4	16	248.8
19	252.0	7	232.0
7	246.6	6	202.7
24	237.0	17	186.4
14	232.3	22	167.1
3	4.1	1	23.5
8	3.8	12	19.6
9	2.1	2	18.1
15	1.1	10	4.4
2	-21.8	15	-11.6
10	-29.9	9	-33.2
1	-45.8	3	-45.1
12	-46.4	8	-72.8
23	-145.3	5	-100.2
11	-148.4	20	-112.8
13	-149.4	21	-127.1
18	-155.9	4	-135.9
21	-173.8	13	-141.2
20	-187.0	18	-176.2
4	-196.4	11	-182.8
5	-196.8	23	-204.1

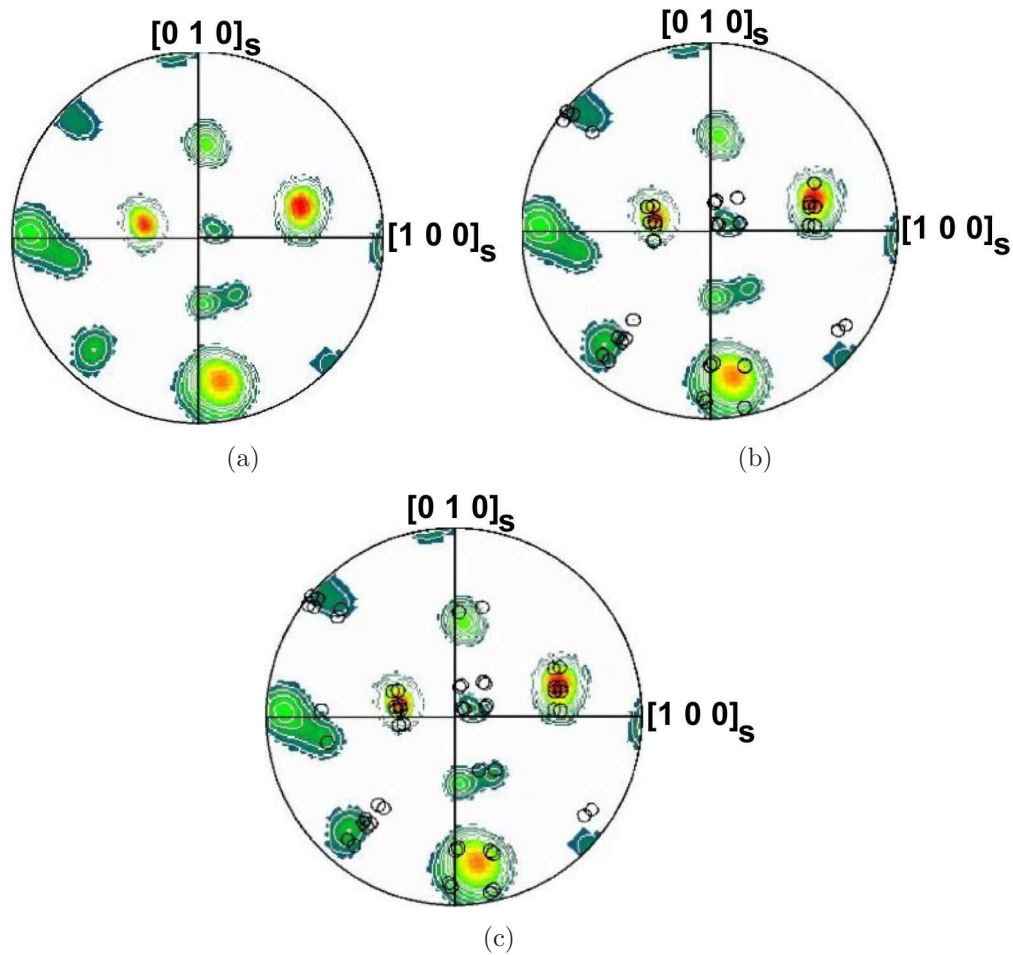


Figure 5.6: $1\ 0\ 0_{\alpha'}$ pole figures of Grain A from 30Ni-Stress steel. (a) Experimental. (b) Model predicted, allowing 12 most favoured variants to form. (c) Model predicted, allowing 18 most favoured variants to form.

intensity are in fact covered by the first 12 variants associated with positive interaction energies.

To further check the variant selection model another grain has been chosen (shown as Grain B in Fig. 5.5) which is smaller in size and thus it is more likely that not all the variants of martensite would form. Fig. 5.7a shows the experimental $1\ 0\ 0_{\alpha'}$ pole figure from this grain where the data are fully explained by the first 8 most favoured variants listed in Table 5.1. The

model predicted pole figure is shown in Fig. 5.7b.

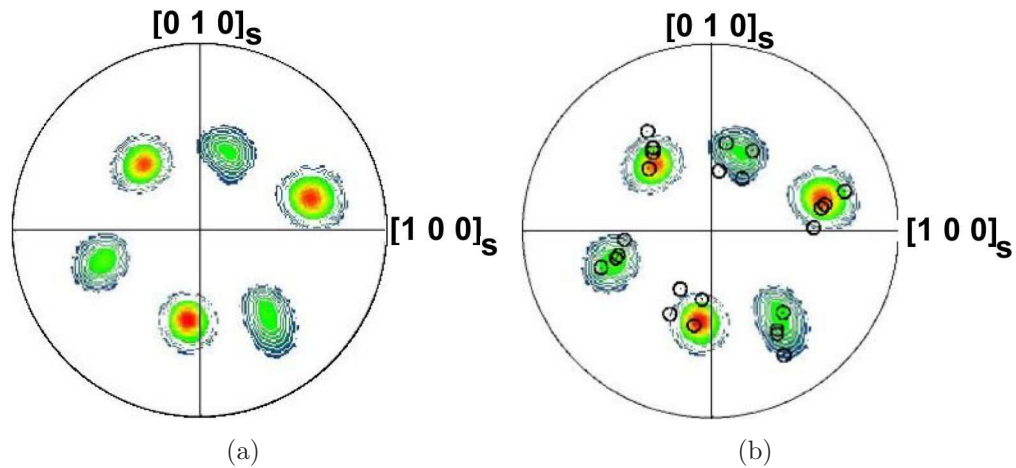


Figure 5.7: $1\ 0\ 0_{\alpha'}$ pole figures of Grain B from 30Ni-Stress steel. (a) Experimental. (b) Model predicted, allowing 8 most favoured variants to form.

5.3.2 Analysis from alloy “30Ni-Strain”

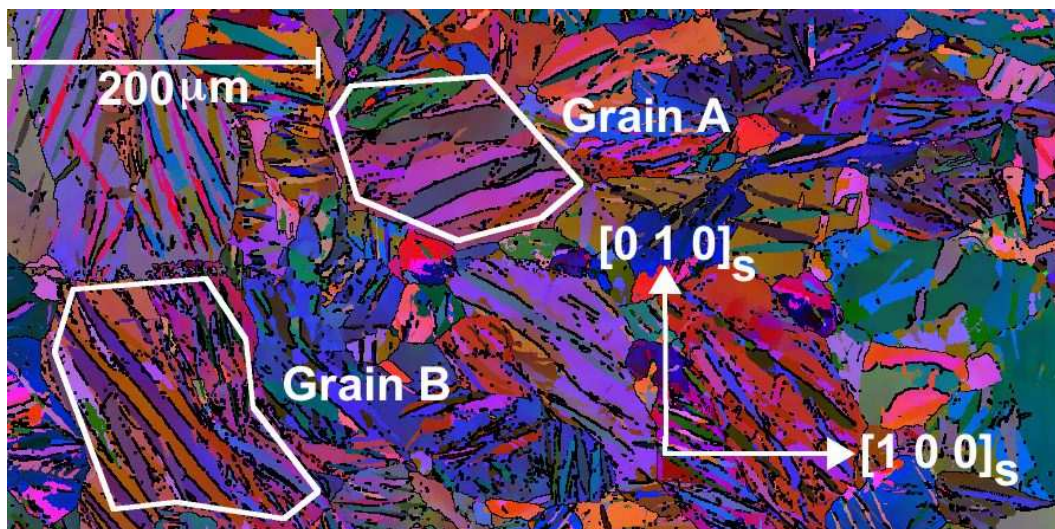


Figure 5.8: All Euler image from EBSD analysis of the samples “30Ni-Strain”. From two grains marked as ‘A’ and ‘B’ pole figures are constructed.

Fig. 5.8 shows the all Euler photograph of the of sample “30Ni-Strain”. This figure shows the total area scanned in EBSD, pole figures were obtained from two grains marked as Grain A and Grain B. Although the sample was unloaded prior to cryogenic treatment, the analysis that follows assumes that variant selection can be determined on the basis of the interaction of α' with stress. The purpose was to see how far this might succeed in explaining texture on the crude hypothesis that the unloaded, plastically strained austenite retains a memory of the original stress in the dislocation or other strain induced structure during tensile deformation.

The stress tensor acting on the sample before quenching is assumed to be pure tensile. This is of course a simplified assumption as the real stress tensor here should be the residual stress acting on these grains which is very difficult to measure or calculate.

Following the same procedure described in the previous section $1\ 0\ 0_{\alpha'}$ pole figures have been predicted for the two grains. It can be seen from Fig. 5.9 and Fig. 5.10 that the experimental and model predicted pole figures matches very well.

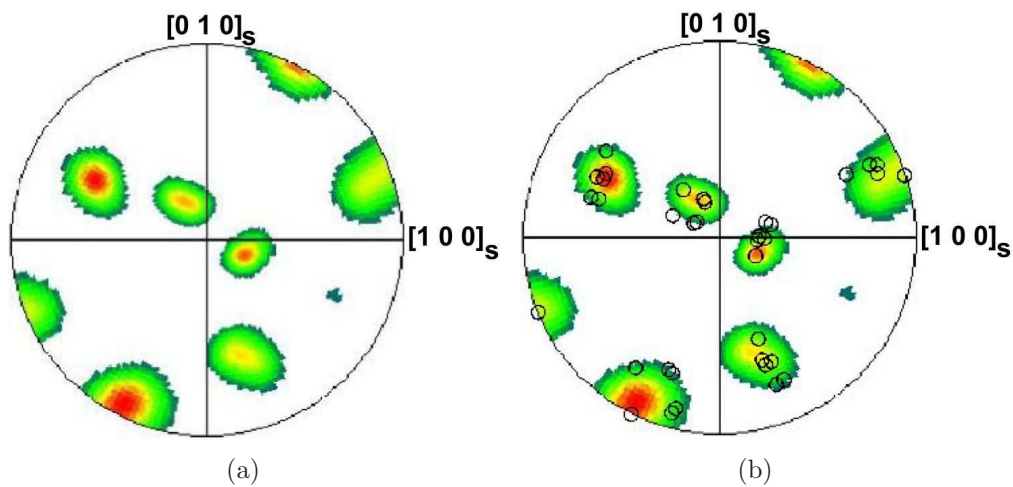


Figure 5.9: $1\ 0\ 0_{\alpha'}$ pole figures of Grain A from 30Ni-Strain steel. (a) Experimental. (b) Model predicted, allowing 12 most favoured variants to form.

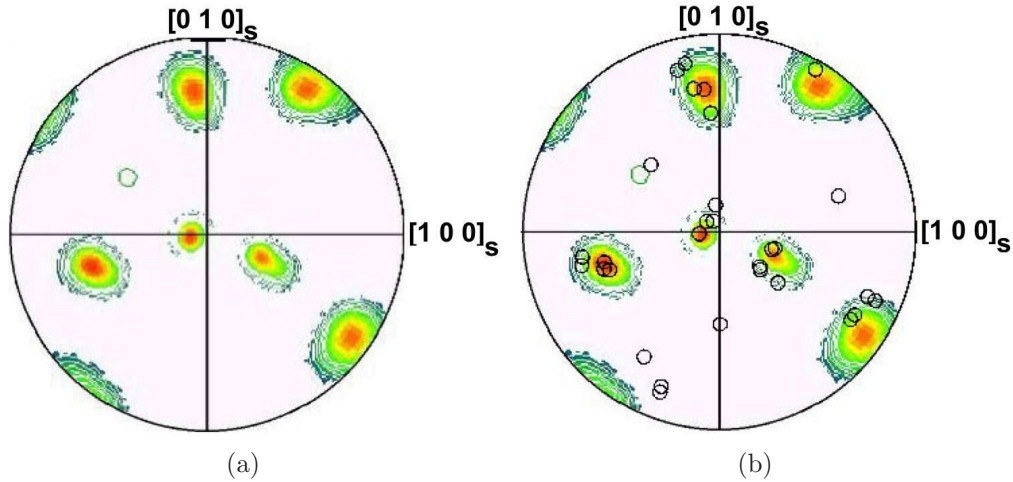


Figure 5.10: $1\ 0\ 0_{\alpha'}$ pole figures of Grain B from 30Ni-Strain steel. (a) Experimental. (b) Model predicted, allowing 10 most favoured variants to form.

The following conclusions can be made from the results produced in this section.

1. When transformation occurs from plastically deformed austenite under stress variant selection can be described using Patel and Cohen's theory [12].
2. When transformation takes place from plastically strained austenite but without any influence of external load variant selection can still be explained using Patel and Cohen's theory. It seems under low degree of plastic strain austenite retains the memory of the original stress.
3. The results presented here contains 12-18 variants of martensite in each grain due to large chemical driving force. The large number of variants makes it difficult to validate the variant selection model with high precision in some cases. If the under cooling can be restricted and formation of martensite is limited to 20-30% variant selection models can be validated more rigorously.

5.4 Texture prediction in a 304 austenitic stainless steel

In an elegant experimental study on 304 austenitic stainless steel, Gey *et al.* [8] found that not all of the 24 possible crystallographic variants of martensite (α') formed when the alloy was deformed to 10% elongation in tension at -60°C.

Variant selection was particularly noticeable in austenite (γ) grains belonging to the Goss and Cube components of texture, which transformed to smaller fractions of martensite. This is presumably because the early stages of transformation are dominated by the α' variants most favoured by the external stress. The selection process was explained qualitatively by associating the martensite with the slip systems that have the greatest Schmidt factors, although even on the “activated” $\{111\}_\gamma$ planes, only a fraction of the possible variants were found.

The transformation texture for the data published by Gey *et al.* [8] was modelled using a self-consistent set of crystallographic parameters. The set associated with a single martensite variant, gives a habit plane close to the approximately $\{2\ 5\ 9\}_\gamma$ plane reported by Lagneborg [78] for the same steel. The lattice parameter of austenite in 304 stainless steel is estimated to be 0.3589 nm [79] and that of the martensite is taken to be 0.2873 nm. This standard set is given as follows, calculated as in [13]:

Habit plane	$(-0.183989 \ 0.596344 \ -0.781359)_\gamma$
Shape deformation matrix $(\gamma \text{ P } \gamma)$	$\begin{pmatrix} 0.991342 & 0.028064 & -0.036770 \\ 0.028064 & 0.909040 & 0.119180 \\ 0.029429 & -0.095386 & 1.124979 \end{pmatrix}$
Coordinate transformation matrix $(\gamma \text{ J } \alpha)$	$\begin{pmatrix} 0.579356 & 0.542586 & 0.102537 \\ 0.014470 & 0.133650 & -0.788984 \\ -0.552000 & 0.572979 & 0.086936 \end{pmatrix}$

The matrix notation used above is due to [10]. This set implies that

$$(1 \bar{1} 1)_\gamma = (0.012886 \ 0.981915 \ 0.978457)_\alpha$$

$$[1 \ 1 \ 0]_\gamma = [0.927033 \ 1.055684 \ -1.071623]_\alpha$$

It can be noticed that $(1 \bar{1} 1)_\gamma$ is approximately parallel to $(0 \ 1 \ 1)_\alpha$ and $[1 \ 1 \ 0]_\gamma$ is approximately parallel to $[1 \ 1 \ \bar{1}]_\alpha$. The actual relationship is irrational to ensure the invariant–line necessary for martensitic transformation.

The full twenty four crystallographic sets corresponding to the 24 variants of martensite possible in each austenite grain can be generated using symmetry operations. The interaction energy for each of the 24 variants in a 500 γ grain aggregate have been calculated using the procedure described in section 3.3. δ and s are the dilatational and shear strains due to the shape deformation of martensite, which can be shown using $(\gamma \text{ P } \gamma)$ to be 0.02536 and 0.2245 respectively [13]. It is to be noted that calculating the interaction energy in this way is complete [12] compared with the approach in which only the symmetrical part of the shape deformation is used [20, 80].

To model the martensite texture beginning with that of austenite it was necessary to replicate the latter first. This was done for Goss and Cube texture for a 500 austenite grains aggregate following the procedure described in section 3.4 of Chapter 3.

A variant is said to be favoured when interaction energy adds to the driving force for transformation. Each austenite grain is then allowed to transform to only the favoured variants, thus allowing the transformation texture to be calculated. It is emphasised that each austenite grain is transformed equally into the selected variants having equal fractions of each favoured variant. This is because the relationship between the interaction energy and fraction transformed is not clear. Therefore, although the crystallography should be correctly predicted, the detailed intensities may not be accurate.

For the Cube component of austenite texture, Fig. 5.11a shows the measured pole figure for martensite [8], Fig. 5.11b the calculated pole figure allowing only the favoured variants, and finally, Fig. 5.11c illustrates what should happen if all possible variants are allowed to form. Similar results for the Goss oriented austenite grains are shown in Fig. 5.12. The agreement between the calculated transformation texture based on favoured variants and the measured data is remarkably good.

The following conclusions can be made from the results produced in this section.

1. Variant selection has a substantial effect on the crystallographic texture during displacive transformation.
2. Variant selection can be explained with the help of Patel and Cohen's [12] theory.
3. Not only under stress but Patel and Cohen's theory is able to explain the variant selection when the transformation occurs from plastically deformed austenite. However the degree of plastic deformation has to be low.
4. The model is fully capable of predicting the transformation texture

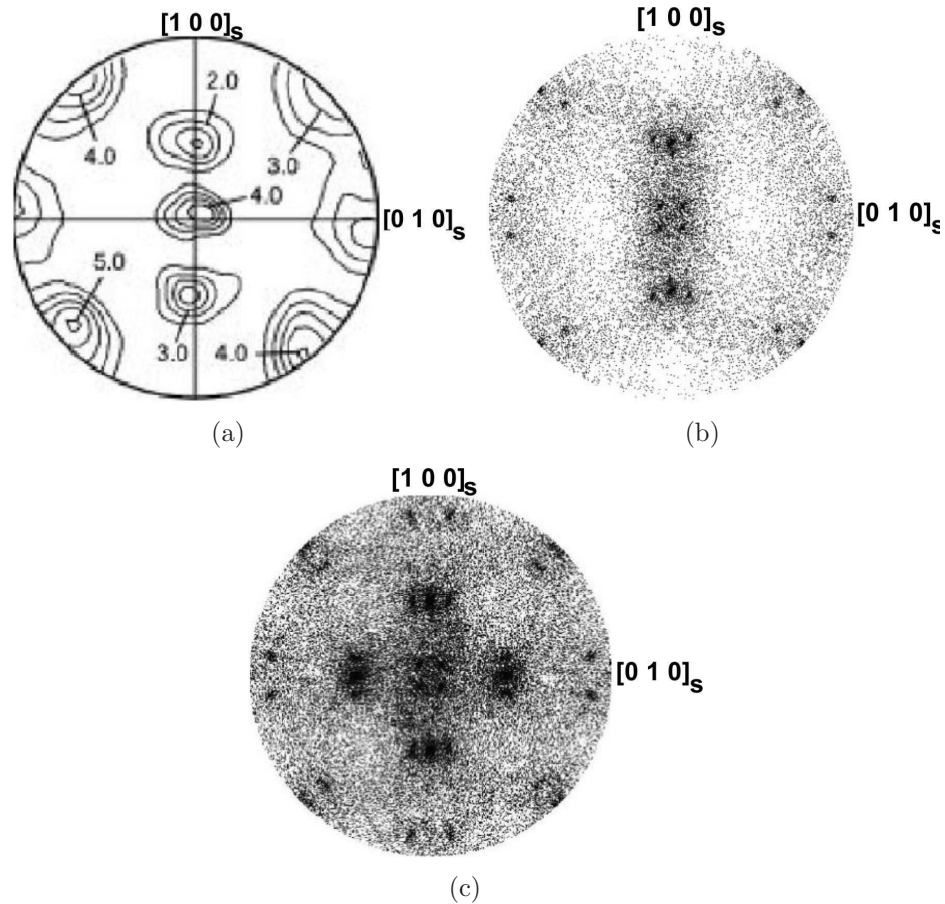


Figure 5.11: $100_{\alpha'}$ pole figures for transformation of Cube oriented austenite grains. (a) Experimental data [8]. (b) Calculations allowing only favoured variants of martensite to form in each austenite grain. (c) Calculations allowing all possible variants of martensite to form in each austenite grain.

using a self-consistent crystallographic data set generated following the phenomenological theory of martensite crystallography.

5.5 Texture in rolled steels

It has been discussed in Chapter 2, Furubayashi *et al.* [9, 33] attempted various variant selection models to estimate the transformation texture in

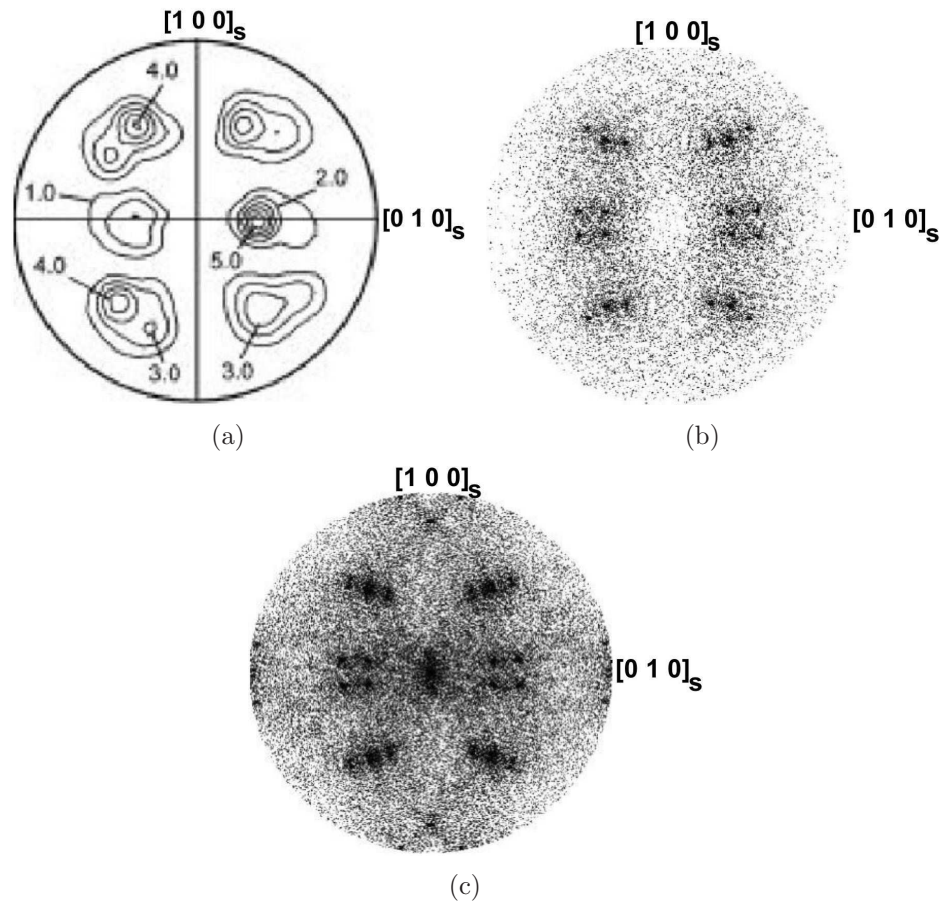


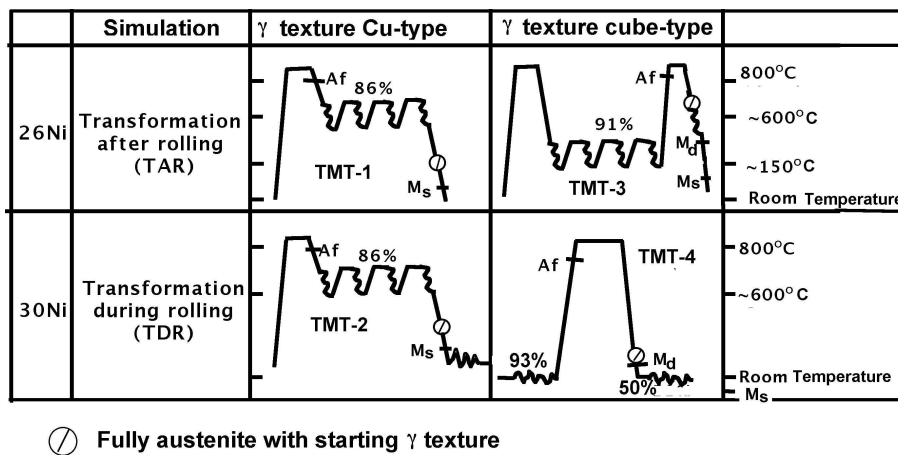
Figure 5.12: $100_{\alpha'}$ pole figures for transformation of Goss oriented austenite grains. (a) Experimental data [8]. (b) Calculations allowing only favoured variants of martensite to form in each austenite grain. (c) Calculations allowing all possible variants of martensite to form in each austenite grain.

two high Ni alloys (composition is given in Table 5.2).

Through proper heat treatment and rolling (shown in Fig. 5.13) Cube and Copper type texture was introduced in the austenite of the two Fe-Ni alloys. Martensite transformation was then induced either by cooling the austenite below the M_S temperature (Transformation After Rolling, TAR process) or by deforming the austenite below the M_d temperature (Transformation During Rolling, TDR process). Furubayashi *et al.* has shown that

Table 5.2: Composition of the two alloys used by Furubayashi *et al.* [9].

Alloy	Composition / wt%						
	Ni	Mn	Al	C	N	Si	Fe
26Ni	25.76	0.085	0.025	0.001	0.0012	0.002	bal.
30Ni	29.67	0.085	0.025	0.001	0.0012	0.002	bal.

Figure 5.13: Thermo-mechanical treatment given by Furubayashi *et al.* to produce desired texture in Fe-Ni alloys [9].

the “Bain strain model” was most accurate in predicting the transformation texture amongst all the models they considered. The Bain strain alone is however an incomplete description of the shape deformation associated with the martensite transformation.

There exist a few more limitations in the work done by Furubayashi *et al.*. First of all, experimental evidence has been given about the formation of Cube type texture after a particular heat treatment and rolling cycle (TMT-3 and TMT-4 as shown in Fig. 5.13) but the same for Cu type texture (TMT-1 and TMT-2 as shown in Fig. 5.13) has not been presented in [9]. From the experimental pole figure presented in another work by the same author [33] and from the simulated austenite pole figure presented in [9], it seems

that a pure Cu-type texture in austenite has not been achieved. Which is quite expected, as rolling of steel almost always results in a mixture of various texture components. Fig. 5.14a,b show the experimentally observed and simulated “Cu-type” texture by Furubayashi *et al.*. If this is compared with the pure Cu-type texture presented in Fig. 3.5c the difference is evident.

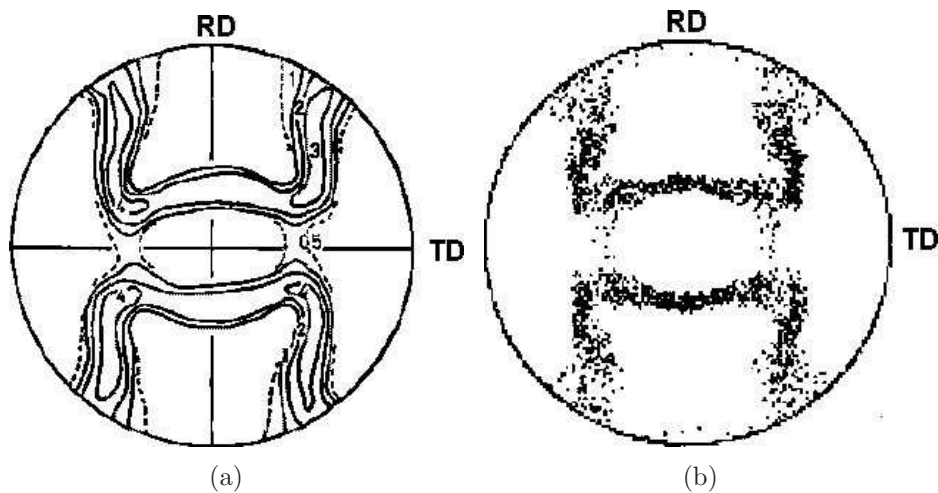


Figure 5.14: “Cu-type” texture in austenite, (a) experimental [33] and (b) simulated [9].

To reproduce the initial austenite texture for the TMT-1 and TMT-2 treatments a combination of common texture components of austenite were composed and compared with observation. It was found (Fig. 5.15) that a mixture of 50% Cu and 50% S type texture gave a good match with the texture used by Furubayashi *et al.* (as shown in Fig. 5.14). So in the present model for TMT-1 and TMT-2 rolling sequence prior austenite texture has been assumed to be a mixture of 50% S and 50% Cu.

Furubayashi *et al.* assumed that the stress during rolling is a triaxial compressive type. But the exact nature of the stress tensor during rolling is a subject of study in its own right [81–84]. Although a triaxial compressive stress may be relevant to TDR process, this is not the case for TAR process

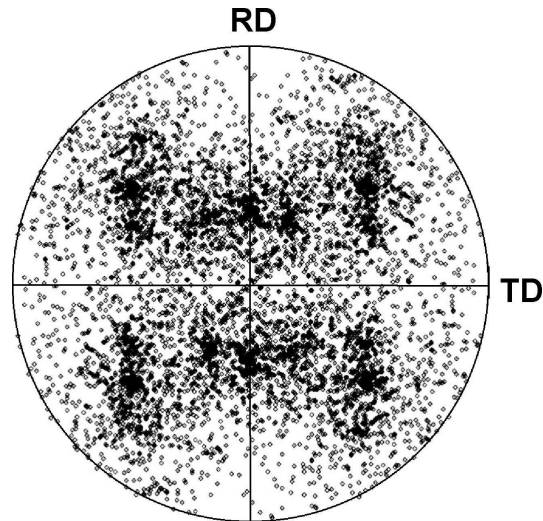


Figure 5.15: Simulated $1\ 0\ 0_\gamma$ pole figure assuming 50% Cu and 50% S component.

where the residual stress due to plastic deformation plays a role.

According to Wang *et al.* [85] the residual stress tensor varies with the type of austenite texture. Furubayashi *et al.* did not begin with such a tensor but rather varied the stress components until a fit could be obtained with the transformation texture. Indeed four empirical parameters were additionally introduced to deal with variant selection. The work presented in the next section addresses this without fitting the stress tensor and using better justified variant selection criteria.

5.5.1 Modelling the TAR process

An attempt was made to separate the effects of stress and strain by assuming that variant selection is affected by stress only. Strain manifests by influencing the prior texture of austenite and by generating a pattern of residual stress within the material. The residual stress tensor associated with the prior austenite texture has been taken from the work of Wang *et al.* [85], Ta-

ble 5.3. To model the TAR process the initial austenite texture was assumed to be a mixture of Cu and S components (50% each) and the residual stress tensor (equation 5.1) was calculated using the data presented in Table 5.3 :

$$\begin{pmatrix} -219 & 0 & -35 \\ 0 & -35 & 24 \\ -35 & 24 & -52 \end{pmatrix} \quad (5.1)$$

Table 5.3: Stress tensor for major texture components in the austenite phase of cold-rolled stainless steel [85].

Texture components	σ_{11} / MPa	σ_{22} / MPa	σ_{33} / MPa	σ_{23} / MPa	σ_{13} / MPa	σ_{12} / MPa
{1 1 0}<1 1 2> Brass	-292	37	73	0	0	± 13
{1 1 0}<0 0 1> Goss	9	64	158	0	0	0
{1 1 2}<1 1 1> Copper	-188	-83	-108	0	± 41	0
{1 2 3}<6 3 4> S	-250	12	5	± 24	± 30	0

Variant selection model in this work is done following the Patel and Cohen's theory. Variants were ranked in terms of the interaction energies and the first 8 most favoured variants were allowed to form. In any grain if any of the first 8 variants had negative interaction energy it was not considered as a favoured variant. The values of the interaction energies are given in Table 5.4. The experimental [9] and the model predicted pole figures are shown in Fig. 5.16 and the agreement is good without the assumptions made by Furubayashi *et al.*. It must be noted that the stress tensor used in this model is taken from literature, which is an approximation. If a model is developed to predict the residual stress tensor for the appropriate rolling conditions a much better texture prediction can be obtained.

Table 5.4: Interaction energy U (J mol^{-1}) for 24 variants in five randomly chosen austenite grains from an aggregate of 1000 grains with an initial γ texture consists of Cu and S components (50% each). The simulation is done for a stress tensor shown in equation 5.1. The energies are arranged in descending order, with positive values corresponding to a favourable interaction with the applied stress and *vice versa*.

Grain 1		Grain 2		Grain 3		Grain 4		Grain 5	
Variant	U	Variant	U	Variant	U	Variant	U	Variant	U
23	47.4	8	48.5	23	117.4	18	122.3	23	84.9
8	34.6	23	42.2	18	114.9	23	111.3	18	69.9
13	32.2	22	23.8	8	92.7	5	94.6	13	64.5
18	25.2	18	20.9	3	83.5	4	73.9	8	40.4
15	10.8	3	17.8	20	48.9	20	71.6	5	35.1
3	5.8	13	5.5	21	45.5	13	66.7	11	31.1
11	0.7	6	2.2	10	23.9	21	58.1	3	22.6
22	-0.6	24	-2.7	13	20.2	11	43.6	21	12.1
6	-9.2	10	-8.8	5	18.3	8	41.3	4	10.8
5	-10.1	15	-9.8	2	14.4	3	41.2	15	8.9
21	-16.9	14	-17.8	4	-7.9	1	-2.7	20	6.1
9	-20.9	21	-19.4	11	-11.8	12	-5.6	9	-14.7
20	-24.0	20	-24.1	22	-44.0	10	-6.9	12	-24.9
4	-26.5	11	-25.2	15	-61.5	2	-14.6	1	-30.5
10	-26.7	2	-31.4	17	-66.1	15	-27.9	10	-31.1
24	-29.1	5	-33.7	12	-69.5	9	-38.7	2	-42.5
14	-31.3	17	-43.3	1	-69.8	22	-116.5	22	-52.7
12	-31.4	9	-43.4	24	-73.0	17	-122.0	6	-63.8
2	-46.4	12	-47.7	9	-80.0	24	-134.6	14	-83.3
1	-48.2	4	-47.9	19	-95.4	14	-135.7	24	-84.8
17	-62.7	19	-61.7	6	-101.0	7	-138.2	17	-90.6
16	-74.2	1	-67.3	14	-109.6	6	-141.1	16	-107.4
7	-81.4	16	-67.9	7	-122.8	19	-147.8	7	-108.9
19	-82.1	7	-73.9	16	-132.3	16	-157.3	19	-116.2

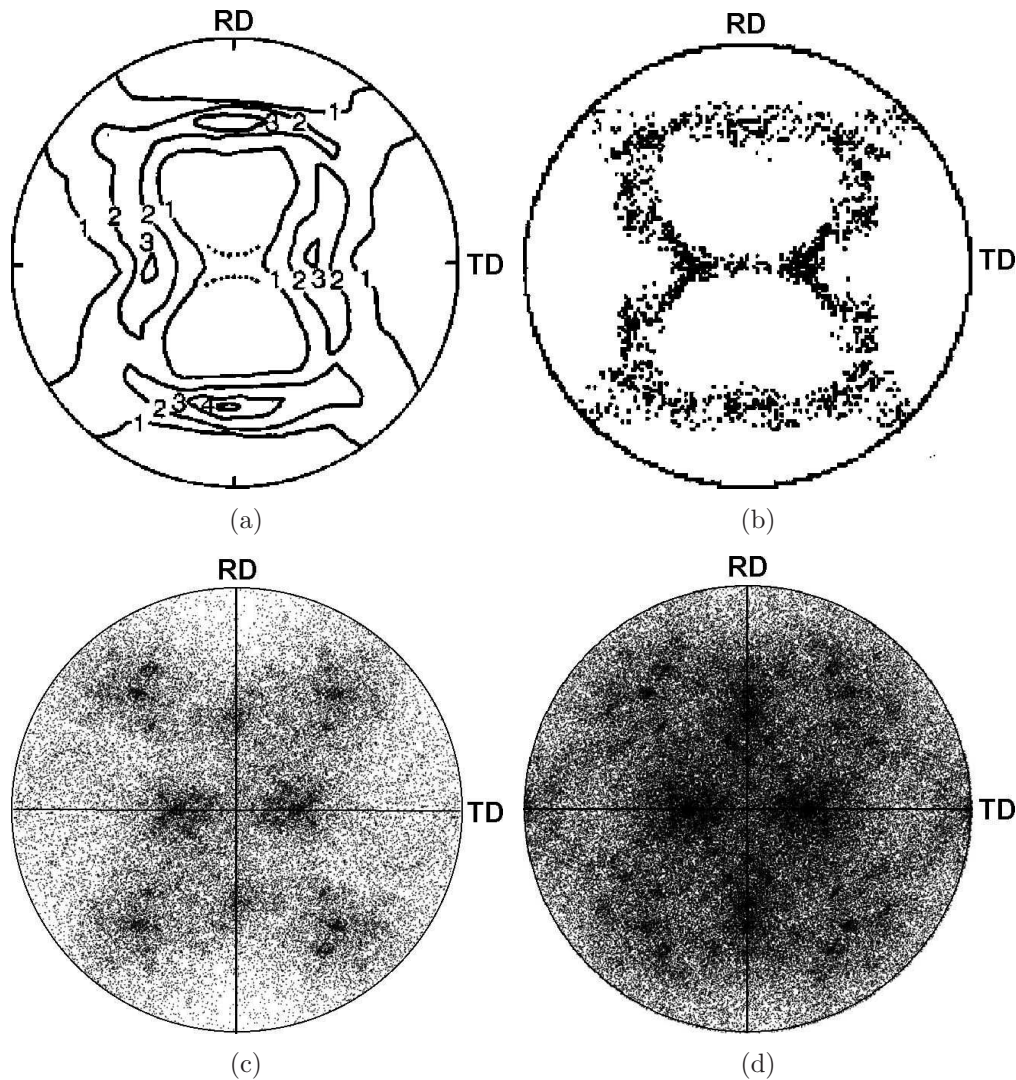


Figure 5.16: $1\ 0\ 0_{\alpha'}$ pole figures from 26Ni steel after TAR simulations. (a) Experimental and (b) simulated [9]. Model prediction from the present work following Patel-Cohen theory, (c) allowing 8 most favoured variants (d) allowing all 24 variants.

5.5.2 Modelling the TDR process

Transformation during rolling occurs below the M_d temperature (Fig. 5.13). Furubayashi *et al.* have modelled the texture assuming triaxial compressive stresses, but the components of stress were chosen empirically.

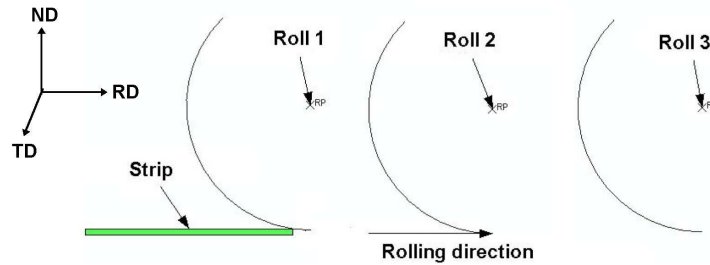


Figure 5.17: Arrangement of rolls in the finite element simulation done in ABAQUS.

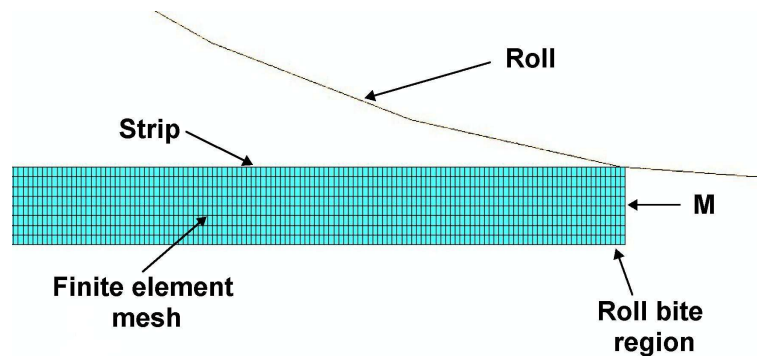


Figure 5.18: Finite element mesh distribution in the strip for the rolling simulation in ABAQUS. The resultant stress tensor is obtained from a mesh pointed as 'M' from the roll bite region at mid-thickness in the strip.

In order to estimate the stress tensor, Mr. Raju Dasu (TATA STEEL) assisted with a finite element (FE) analysis of an elastic-plastic deformable sheet using ABAQUS/Standard (version 6.6) in cold rolling reduction of 60% (Fig. 5.13). Although in [9] the entire reduction was achieved in single pass, the FE model assumed rigid rolls and elastic-plastic deformable sheet with an initial sheet thickness of 1.6 mm reduced finally to 0.8192 mm in three equal passes. The sheet was assumed to be symmetrical about a mid plane through the thickness of the sheet. Plane strain conditions were assumed to prevail. The total number of elements for the sheet was 4000. The contact between

the rolls and the sheet is significant in simulating the rolling processes. These interactions were modelled with a penalty frictional contact algorithm in kinematic constraint formulation. The interactions between the rolls and the strip is modelled with a friction coefficient of 0.3. Figs 5.17 and 5.18 show the rolling arrangement and the mesh distribution, respectively. The stress tensor (given in equation 5.2) is determined for every element shown in Fig. 5.18 but used is that from an element mid-thickness in the roll-bite region ('M' in Fig. 5.18).

$$\begin{pmatrix} -136 & 0 & -35 \\ 0 & -386 & 0 \\ -35 & 0 & -623 \end{pmatrix} \quad (5.2)$$

Model predictions for $1\ 0\ 0_{\alpha'}$ texture have been done for the Cube and a mixture of Cu and S (50% each). For initial Cube texture experimental and model predicted $1\ 0\ 0_{\alpha'}$ texture is shown in Fig. 5.19. It can be seen that excellent match is obtained. For the present model in each grain first four most favoured variants were allowed to form because in most of the grains it has been found that the interaction energy values for first four variants are much higher than the rest. The examples of interaction energies, for austenite having Cube type texture, are shown in Table 5.5.

Fig. 5.20 shows the experimental and model predicted $1\ 0\ 0_{\alpha'}$ texture for TDR process where the initial austenite texture was a mixture of Cu and S. It can be seen that the match in this case is not as good as it is for the Cube textured austenite.

There are two possible explanations. The Cube textured austenite is an accurate representation of the experimental austenite. For TMT-1 and TMT-2 the texture in austenite is a mixture of various components, it has been assumed to be a mixture of 50% Cu and 50% S but is likely to be more complex. Secondly the estimation of the stress tensor is simplistic.

Table 5.5: Interaction energy U (J mol^{-1}) for 24 variants in three randomly chosen austenite grains from an aggregate of 500 grains having a Cube type texture. The simulation is done for a stress tensor shown in equation 5.2. The energies are arranged in descending order, with positive values corresponding to a favourable interaction with the applied stress and *vice versa*.

Grain 1		Grain 2		Grain 3	
Variant	U	Variant	U	Variant	U
21	121.0	18	315.5	20	318.8
23	113.2	20	305.8	21	309.0
13	105.1	23	297.4	18	304.6
11	102.9	21	288.9	23	297.7
20	61.2	3	173.3	10	178.5
18	34.5	8	165.7	2	171.2
8	15.6	10	162.1	8	163.1
10	11.3	2	158.7	3	161.1
2	2.5	5	85.6	4	78.1
15	-3.0	4	81.1	5	71.2
9	-31.1	13	43.4	11	56.8
3	-36.3	11	40.3	13	52.9
4	-51.8	1	-197.4	12	-208.8
5	-68.6	12	-200.7	1	-215.1
22	-157.7	9	-240.1	15	-230.3
12	-164.9	15	-240.9	9	-233.3
6	-168.2	17	-292.6	24	-293.7
24	-172.0	24	-301.3	22	-301.6
1	-197.5	19	-301.9	19	-307.3
19	-222.5	22	-302.9	17	-310.1
14	-235.2	7	-433.3	14	-440.2
16	-238.0	14	-439.4	6	-450.2
17	-251.3	16	-452.0	7	-452.9
7	-309.5	6	-455.7	16	-459.6

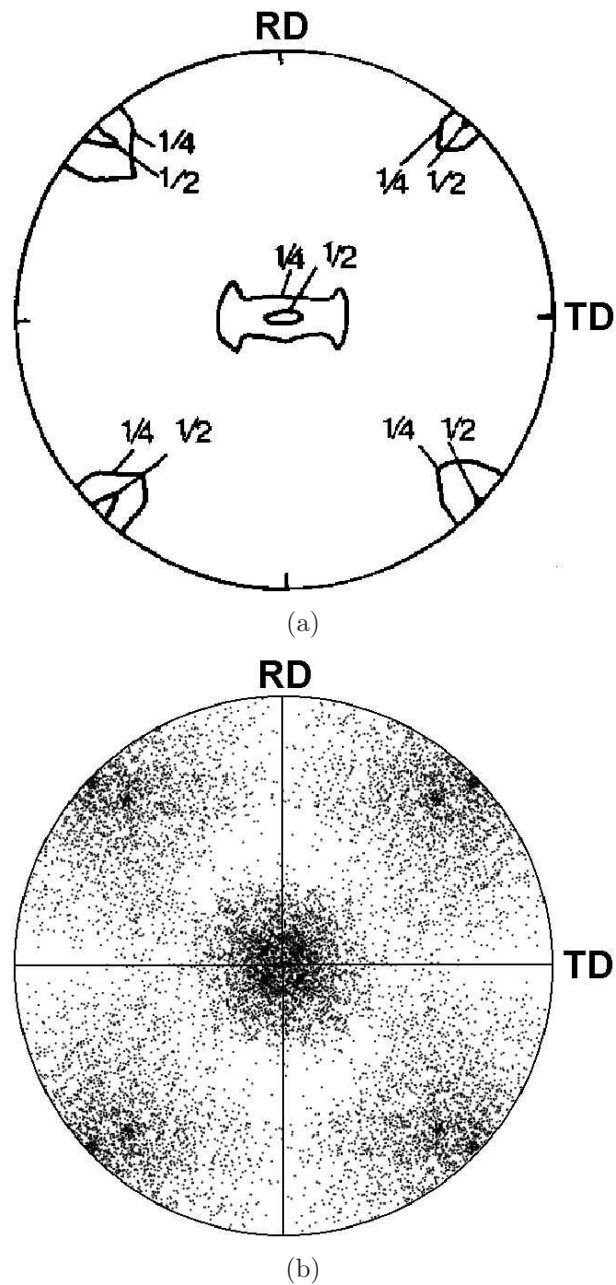


Figure 5.19: $1\ 0\ 0_{\alpha'}$ pole figures from 30Ni steel after TDR process forming from Cube texture austenite. (a) Experimental [9] and (b) model predicted following Patel-Cohen theory allowing 4 most favoured variants to form.

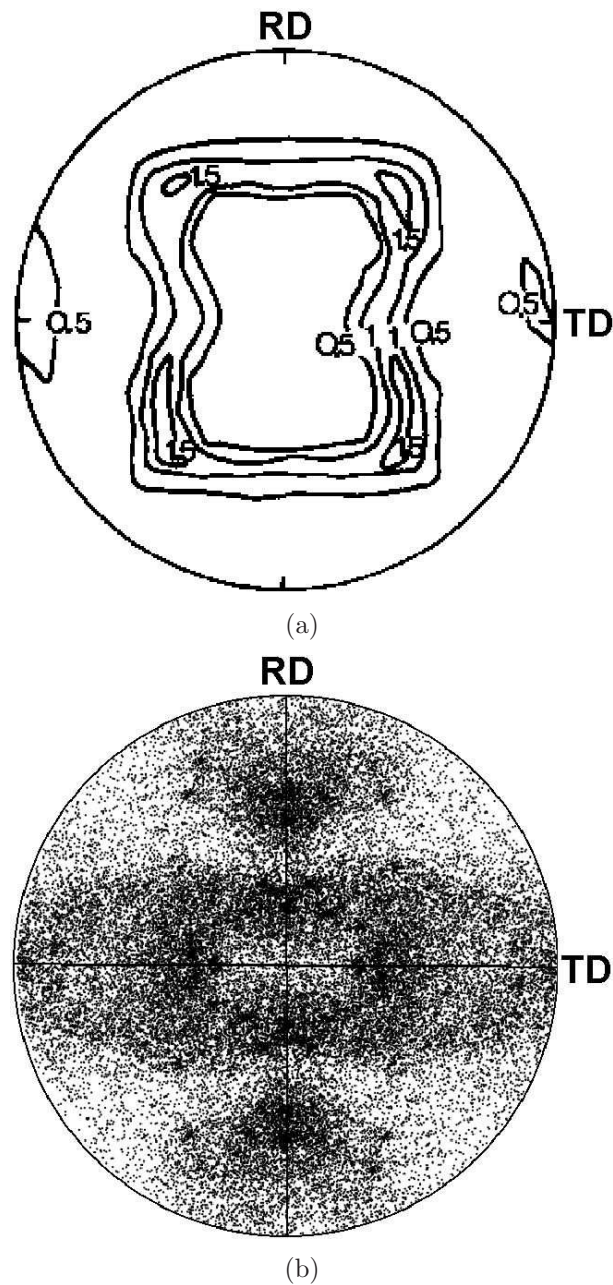


Figure 5.20: $1\ 0\ 0_{\alpha'}$ pole figures from 30Ni steel after TDR process forming from austenite having a mixture of Cu and S type texture. (a) Experimental [9] and (b) model predicted following Patel-Cohen theory allowing 8 most favoured variants to form.

Fig. 5.21 shows the $1\ 0\ 0_{\alpha'}$ texture for a pure compressive stress with an initial austenite texture as in Fig. 5.15, this results in a better match. This pole figure (Fig. 5.21) is quite different from that in Fig. 5.20 indicating the sensitivity of the texture to the nature of stress tensor.

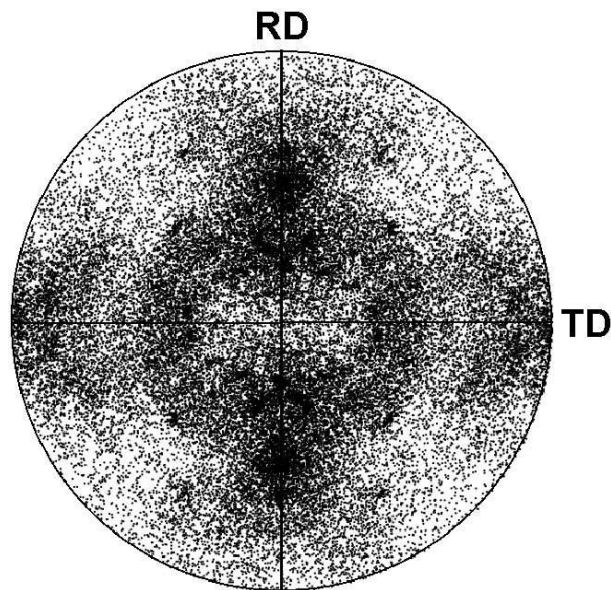


Figure 5.21: Model predicted $1\ 0\ 0_{\alpha'}$ pole figures from 30Ni steel after TDR process assuming a pure compressive stress tensor operative during rolling.

5.6 Severity of transformation texture

Calculations have been done to compare how the $1\ 0\ 0_{\alpha'}$ pole figure would differ when it forms in randomly oriented austenite, and from Cube or Goss textured austenite. Fig. 5.22a shows the texture developed from random austenite under the same conditions as for the Cube and Goss varieties shown in Figs. 5.11 and 5.12 respectively. It has been assumed in all cases that the transformation occurs under tensile stress and 8 most favoured martensite variants are formed. It is evident from Fig. 5.22a,b that transformation from randomly oriented austenite leads to a weaker martensite texture. The effect

is more pronounced when a compressive load is applied to randomly oriented grains (Fig. 5.22b). The conclusion is valid even if a stronger variant selection criteria is used. Fig. 5.23a,b shows the same pole figure as in Fig. 5.22 but allowing only two favoured variants to form. It is clear that the texture becomes slightly stronger but not as much as shown in Figs 5.11 and 5.12.

5.7 Summary

It has been shown for both single crystal and polycrystalline austenite that Patel and Cohen theory can be employed to predict variant selection during martensite transformation that takes place under the influence of stress or indeed, small plastic strain. The method developed here can correctly predict the transformation texture of martensite and capable of incorporating the influence of persisting texture in austenite.

An attempt has also been made to study variant selection in heavily deformed austenite and has been met with partial success in separating the effects of plastic strain and stress. When transformation occurs during the rolling deformation of austenite, variant selection can be reasonably well explained by a triaxial compressive stress. But when transformation occurs on quenching heavily deformed austenite variant selection depends on the nature of residual stresses the characteristics of which is difficult to estimate as a global tensor. It has also been shown that transformation texture is influenced more by the prior austenite texture rather than variant selection.

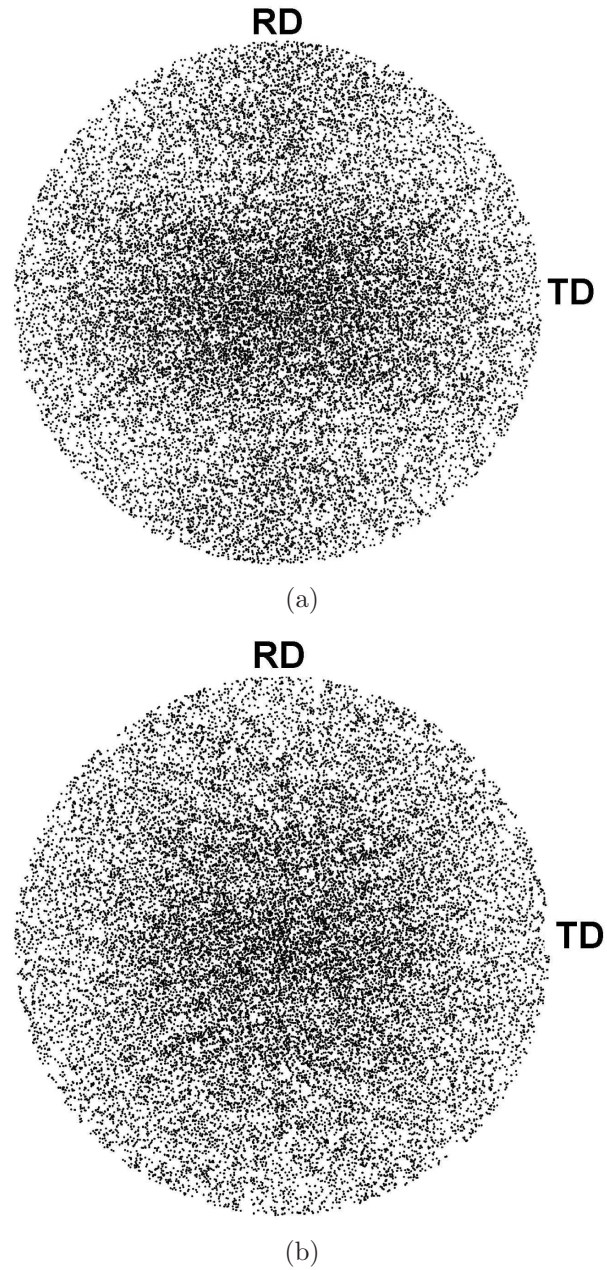
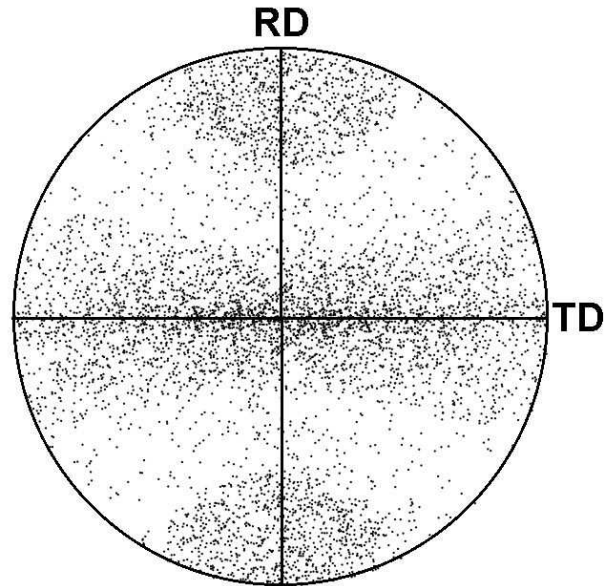
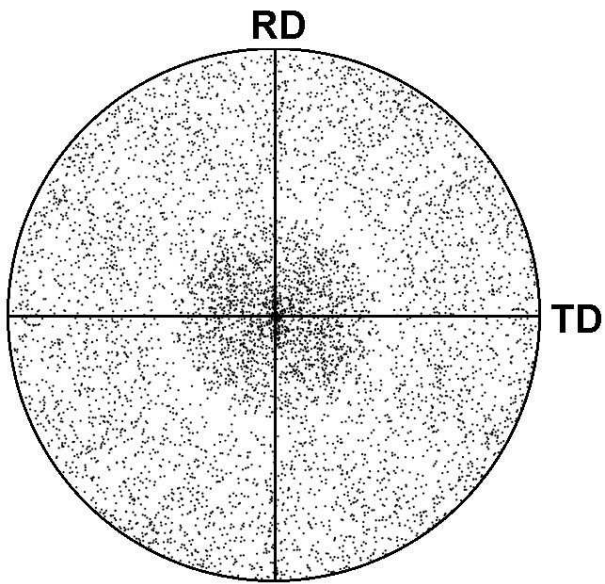


Figure 5.22: Model predicted $1\ 0\ 0_{\alpha'}$ pole figures from randomly oriented austenite matrix allowing 8 most favoured variants to form under (a) tensile load and under (b) compressive load.



(a)



(b)

Figure 5.23: Model predicted $1\ 0\ 0_{\alpha'}$ pole figures from randomly oriented austenite matrix allowing 2 most favoured variants to form under (a) tensile load and under (b) compressive load.

Chapter 6

Texture and intervening transformations

6.1 Introduction

It has been argued in a recent study that the transformation texture of austenitic stainless steels should be calculated in two stages [7]. The austenite first transforms into ϵ -martensite and this then undergoes $\epsilon \rightarrow \alpha'$ reaction, where α' is the body centred cubic martensite and ϵ the hexagonal close packed martensite.

This is because the $\gamma \rightarrow \alpha'$ transformation is said in reality to occur in two stages [86, 87]. A different approach is used to calculate the interaction energy between the applied stress and the transformation strain [7], based on infinitesimal strain elasticity theory rather than the plastic work model of Patel and Cohen [12].

The purpose of the work presented in this Chapter was to see whether it is in fact necessary to account for ϵ -martensite when estimating the transformation texture due to α' . There is after all no *a priori* reason to suppose that anything but the macroscopic shear deformation due to α' can influence

the selection of variants. There should be twenty four of these variants possible irrespective of the way in which the α' develops. The second aim was to assess the different interaction energy criterion used in [7].

There were two sets of results presented by Humbert *et al.* [7]. First, for the transformation of a polycrystalline aggregate of austenite and secondly the detailed assessment of transformation texture in a particular grain of austenite. Using various variant selection criteria they managed to explain the observed crystallography with reasonable amount of success. The following section includes a consideration of their procedure alongside the methodology presented in Chapter 3 and Chapter 4.

6.2 Interaction energy for $\gamma \rightarrow \epsilon$ transformation

The mechanical component of free energy, due to the interaction between an applied stress and the shape deformation associated with each martensite variant has been evaluated following the Patel-Cohen method [12], as described in Section 3.3. This is because the transformation strains are large and are plastic rather than elastic. Table 6.1 lists the interaction energies evaluated by Humbert *et al.* [7] and according to Patel and Cohen. The volume strain associated with the transformation was taken as zero. Humbert *et al.* have used the following equation for calculating the interaction energy:

$$E = \frac{1}{2} \sigma_{ij} \epsilon_{ij} \equiv \frac{1}{2} [\sigma_{11} \epsilon_{11} + \sigma_{22} \epsilon_{22} + \sigma_{33} \epsilon_{33} + \sigma_{12} \gamma_{12} + \sigma_{13} \gamma_{13} + \sigma_{23} \gamma_{23}] \quad (6.1)$$

where E is the strain energy per unit volume, γ_{ij} represents the strain in the simple shear, σ_{ij} is the applied stress presented in the austenite reference frame and ϵ_{ij} is the strain tensor associated with $\gamma \rightarrow \epsilon$ or $\epsilon \rightarrow \alpha'$ transformation. The state of applied stress is classified by a tensor in the austenite

basis, which for a uniaxial stress becomes;

$$\begin{pmatrix} \sigma & 0 & 0 \\ 0 & 0 & 0 \\ 0 & 0 & 0 \end{pmatrix} \quad (6.2)$$

If the shape deformation for any martensite transformation is an invariant-plane strain on a plane with a unit normal $(\mathbf{p}; \gamma^*) = (p_1 \ p_2 \ p_3)$, with a displacement in the unit direction $[\gamma; \mathbf{d}] = [d_1 \ d_2 \ d_3]$ and with a magnitude of the displacement given by 'm' then it can be written as follows [10] :

$$(\gamma \ P \ \gamma) = \begin{pmatrix} 1 + md_1p_1 & md_1p_2 & md_1p_3 \\ md_2p_1 & 1 + md_2p_2 & md_2p_3 \\ md_3p_1 & md_3p_2 & 1 + md_3p_3 \end{pmatrix} \quad (6.3)$$

For $\gamma \rightarrow \epsilon$, $\mathbf{p} \parallel (1 \ 1 \ 1)$, $\mathbf{d} \parallel [\bar{1} \ 2 \ \bar{1}]$ and $m = \frac{1}{\sqrt{8}}$ if there is no volume change accompanying transformation. There will be 11 other crystallographically equivalent variants as listed in Table 6.1.

According to Humbert *et al.*, the strain tensor is obtained as follows:

$$\epsilon_{ij} = \frac{(\gamma \ P \ \gamma) + (\gamma \ P' \ \gamma)}{2} - \mathbf{I} \quad (6.4)$$

where as usual, $(\gamma \ P' \ \gamma)$ is the transpose of the matrix $(\gamma \ P \ \gamma)$, so that:

$$\epsilon_{ij} = \begin{pmatrix} md_1p_1 & (md_1p_2 + md_2p_1)/2 & md_1p_3 + md_3p_1)/2 \\ (md_1p_1 + md_2p_1)/2 & md_2p_2 & md_3p_2 + md_2p_3)/2 \\ (md_3p_1 + md_1p_3)/2 & (md_3p_2 + md_2p_3)/2 & md_3p_3 \end{pmatrix} \quad (6.5)$$

In their approach, for a uniaxial tensile stress, the interaction strain energy

Table 6.1: Calculation of interaction energies associated with $\gamma \rightarrow \epsilon$ transformation following Humbert *et al.* [7] and Patel and Cohen [12] for $\sigma = 200$ MPa and austenite grain oriented with $g^\gamma = [128.99^\circ, 48.27^\circ, 24.27^\circ]$. The ranking is in a descending order of interaction energy. A positive value of interaction energy corresponds to a favourable interaction with the applied stress and *vice versa*.

Variant number	Plane and direction of shear	Interaction energy /MJ m ⁻³ [7]	Interaction energy /MJ m ⁻³ [12]	Ranking
1	(1 1 1)[$\bar{1}$ 2 $\bar{1}$]	-0.77	-1.54	7
2	(1 1 1)[$\bar{1}$ $\bar{1}$ 2]	7.54	15.09	3
3	(1 1 1)[2 $\bar{1}$ $\bar{1}$]	-6.78	-13.55	10
4	($\bar{1}$ 1 1)[2 1 1]	-11.58	-23.17	12
5	($\bar{1}$ 1 1)[$\bar{1}$ 1 $\bar{2}$]	-5.64	-11.28	9
6	($\bar{1}$ 1 1)[$\bar{1}$ $\bar{2}$ 1]	17.23	34.45	1
7	(1 1 $\bar{1}$)[1 $\bar{2}$ $\bar{1}$]	12.37	24.75	2
8	(1 1 $\bar{1}$)[1 1 2]	-2.12	-4.23	8
9	(1 1 $\bar{1}$)[$\bar{2}$ 1 $\bar{1}$]	-10.26	-20.51	11
10	(1 $\bar{1}$ 1)[$\bar{2}$ $\bar{1}$ 1]	0.13	0.27	4
11	(1 $\bar{1}$ 1)[1 $\bar{1}$ $\bar{2}$]	-0.1	-0.2	6
12	(1 $\bar{1}$ 1)[1 2 1]	-0.04	-0.07	5

per unit volume is therefore given by:

$$E = \frac{1}{2} m d_1 p_1 \sigma \quad (6.6)$$

This value is now compared against that obtained using Patel and Cohen's method.

6.2.1 Patel and Cohen approach

From Fig. 6.1a, the displacement along \mathbf{d} can be resolved into components normal to the habit plane ($\delta\mathbf{p}$) and another on the habit plane ($s\mathbf{e}$), where \mathbf{p} and \mathbf{e} are unit vectors, ' δ ' is the dilatational strain and ' s ' is the shear strain. The traction σ_t acting on the habit plane is resolved into a normal stress σ_N and a shear stress τ parallel to \mathbf{e} .

$$\boldsymbol{\sigma}_t = \begin{pmatrix} \sigma & 0 & 0 \\ 0 & 0 & 0 \\ 0 & 0 & 0 \end{pmatrix} \begin{pmatrix} p_1 \\ p_2 \\ p_3 \end{pmatrix} = \begin{pmatrix} \sigma p_1 \\ 0 \\ 0 \end{pmatrix} \quad (6.7)$$

$\therefore \boldsymbol{\sigma}_t \parallel [1 \ 0 \ 0]_\gamma$.

$$\sigma_N = \boldsymbol{\sigma}_t \cdot \mathbf{p} = (p_1 \ p_2 \ p_3) [\sigma p_1 \ 0 \ 0] = \sigma p_1^2 \quad (6.8)$$

As $\boldsymbol{\sigma}_N \parallel \mathbf{p}$, $\therefore \boldsymbol{\sigma}_N = \sigma p_1^2 \mathbf{p}$. From Fig. 6.1b it can be written:

$$\boldsymbol{\sigma}_t - \boldsymbol{\sigma}_N = \boldsymbol{\tau}_{max} = \begin{pmatrix} \sigma p_1 \\ 0 \\ 0 \end{pmatrix} - \begin{pmatrix} \sigma p_1^3 \\ \sigma p_1^2 p_2 \\ \sigma p_1^2 p_3 \end{pmatrix} \quad (6.9)$$

Taking dot product with \mathbf{e} in both sides:

$$\tau = \boldsymbol{\tau}_{max} \cdot \mathbf{e} = (\sigma p_1 \ 0 \ 0) [e_1 \ e_2 \ e_3] - (\sigma p_1^3 \ \sigma p_1^2 p_2 \ \sigma p_1^2 p_3) [e_1 \ e_2 \ e_3] = \sigma p_1 e_1 \quad (6.10)$$

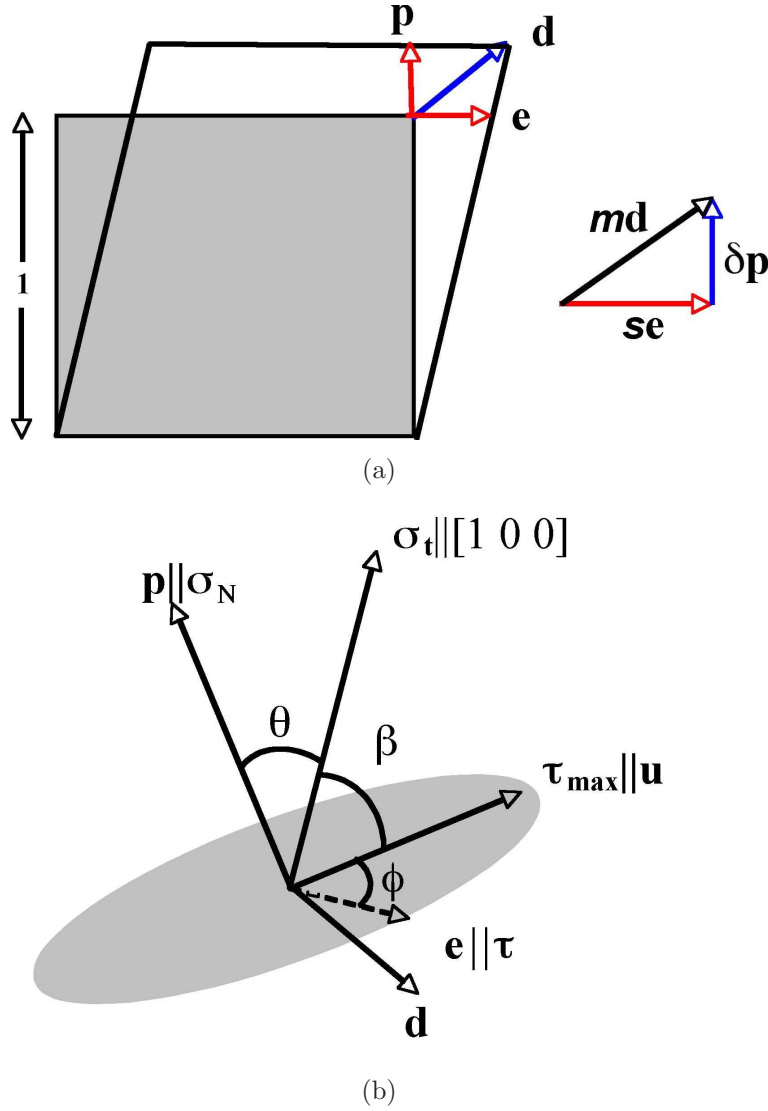


Figure 6.1: (a) Shape deformation associated with the martensite transformation. (b) State of stress on a habit plane.

$$\therefore \tau \parallel \mathbf{e}$$

$$\begin{aligned} \therefore U &= \delta\sigma p_1^2 + s\sigma p_1 e_1 \\ &= \sigma p_1 [\delta p_1 + s e_1] \\ &\equiv m d_1 p_1 \sigma \end{aligned} \tag{6.11}$$

This differs by a factor of 2 from equation 6.6, because the latter incorrectly assumes that the stress-strain relationship is elastic whereas in fact the transformation strain is plastic. The absolute value of the interaction energy is therefore wrong by a factor of exactly 2, as can be seen from Table 6.1. The proof presented here that the two approaches are equivalent other than the factor of 2 can be verified to be valid for a general stress tensor as follows:

$$\boldsymbol{\sigma}_t = \begin{pmatrix} \sigma_{11} & \sigma_{12} & \sigma_{13} \\ \sigma_{21} & \sigma_{22} & \sigma_{23} \\ \sigma_{31} & \sigma_{32} & \sigma_{33} \end{pmatrix} \begin{pmatrix} p_1 \\ p_2 \\ p_3 \end{pmatrix} = \begin{pmatrix} \sigma_{11}p_1 + \sigma_{12}p_2 + \sigma_{13}p_3 \\ \sigma_{21}p_1 + \sigma_{22}p_2 + \sigma_{23}p_3 \\ \sigma_{31}p_1 + \sigma_{32}p_2 + \sigma_{33}p_3 \end{pmatrix} \quad (6.12)$$

$$\begin{aligned} \sigma_N &= \boldsymbol{\sigma}_t \cdot \mathbf{p} \\ &= \sigma_{11}p_1^2 + \sigma_{12}p_1p_2 + \sigma_{13}p_1p_3 \\ &\quad + \sigma_{21}p_1p_2 + \sigma_{22}p_2^2 + \sigma_{23}p_2p_3 \\ &\quad + \sigma_{31}p_1p_3 + \sigma_{32}p_2p_3 + \sigma_{33}p_3^2 \\ &= \sum_{i=1}^3 \sum_{j=1}^3 \sigma_{ij}p_i p_j \end{aligned} \quad (6.13)$$

As $\boldsymbol{\sigma}_N \parallel \mathbf{p}$, $\therefore \boldsymbol{\sigma}_N = \sum_{i=1}^3 \sum_{j=1}^3 \sigma_{ij}p_i p_j \mathbf{p}$.

$$\boldsymbol{\sigma}_t - \boldsymbol{\sigma}_N = \boldsymbol{\tau}_{max}. \quad (6.14)$$

So $\boldsymbol{\tau}$ can be written as:

$$\boldsymbol{\tau} = \boldsymbol{\tau}_{max} \cdot \mathbf{e} = [\boldsymbol{\sigma}_t - \boldsymbol{\sigma}_N] \cdot \mathbf{e} = \boldsymbol{\sigma}_t \cdot \mathbf{e} \quad (6.15)$$

$$\therefore \boldsymbol{\tau} = \sum_{i=1}^3 \sigma_{1i}p_i \mathbf{e}_1 + \sum_{i=1}^3 \sigma_{2i}p_i \mathbf{e}_2 + \sum_{i=1}^3 \sigma_{3i}p_i \mathbf{e}_3$$

$$= \sum_{i=1}^3 \sum_{j=1}^3 \sigma_{ij} p_j e_i \quad (6.16)$$

Form here the interaction energy can be written as:

$$\begin{aligned} U &= \sum_{i=1}^3 \sum_{j=1}^3 [\delta \sigma_{ij} p_i p_j + s \sigma_{ij} e_i p_j] \\ &= \sum_{i=1}^3 \sum_{j=1}^3 \sigma_{ij} p_j [\delta p_i + s e_i] \\ &= \sum_{i=1}^3 \sum_{j=1}^3 \sigma_{ij} p_j m d_i \\ &\equiv \sigma_{ij} \epsilon_{ij} \end{aligned} \quad (6.17)$$

6.3 Texture prediction, single γ crystal

Humbert *et al.* reasonably assumed that the most favoured variant should correspond to the highest interaction energy. They argued that from a single ϵ variant it is possible to generate 6 α' variants of which only three variants are favoured when interacting with a uniaxial tensile stress. Fig. 6.2 shows their measured and model predicted pole figures for the α' transformation reaction. The poles are distributed in three different groups designated here as 'A', 'B' and 'C'. According to Humbert *et al.* 'C' corresponds to the "main variants", presumably on the basis of the observed intensities. Fig. 6.2b shows that the poles from region 'A' are not reproduced theoretically.

Humbert *et al.* assumed different variant selection criteria for $\gamma \rightarrow \epsilon$ and $\epsilon \rightarrow \alpha'$ reactions. For the first transformation a "strong" variant selection criteria was used. In this case all the variants having less than 90% of the highest interaction energy were considered to be not favourable. On the other hand for the $\epsilon \rightarrow \alpha'$ reaction variants having more than 20% of the highest interaction energy were assumed to be forming. Variant selection

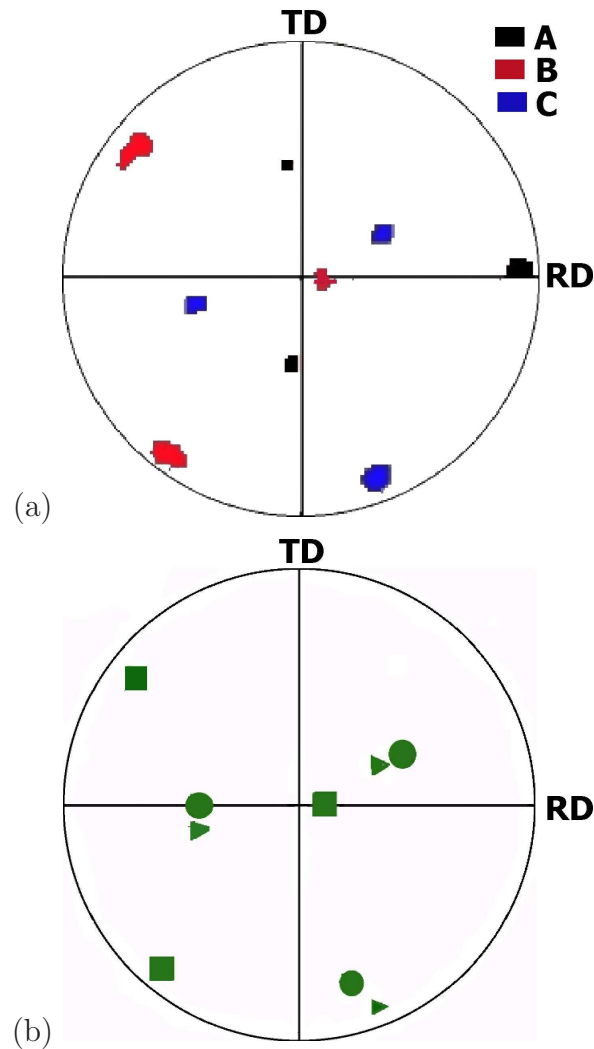


Figure 6.2: 1 0 0 pole figure of α' martensite for an austenite grain having orientation $g^\gamma = [128.99^\circ, 48.27^\circ, 24.27^\circ]$ (here the angles represent Euler angles), (a) measured (b) model by Humbert *et al.* [7].

criteria in this case was much “weaker” than the previous one. The reason behind choosing a different criteria for variant selection in two reactions are not clear.

The texture of α' phase from the same austenite grain has also been modelled here using the method described in Chapter 4 directly for the trans-

formation $\gamma \rightarrow \alpha'$, neglecting any intervention of ϵ martensite. Taking the parent austenite grain orientation from [7], the interaction energies associated with the 24 possible variants of martensite have been calculated as shown in Table 6.2. The crystallographic data used to define the α' are shown in Table 6.3, the data have been obtained following the procedure described in [13].

The first 13 most favoured variants listed in Table 6.2 are all assumed to form. Fig. 6.3 shows the comparison between experimental and model predicted $1\ 0\ 0_{\alpha'}$ pole figure. It is obviously possible to explain all the observed intensities.

6.4 Summary

The results show that it is not necessary to consider ϵ -martensite in order to predict the α' -martensite transformation texture in austenitic stainless steel. Furthermore, that the Patel and Cohen method, which correctly treats the transformation strain as plastic can be directly used to calculate the interaction energies. The two-step method in contrast requires additional assumptions.

Table 6.2: Calculation of interaction energy associated with $\gamma \rightarrow \alpha'$ transformation following Patel-Cohen [12].

Ranking	Variant No.	Interaction energy J mol^{-1}
1	2	110.64
2	10	108.68
3	21	100.36
4	20	88.80
5	3	79.43
6	8	72.52
7	23	61.11
8	18	60.21
9	19	59.17
10	24	41.87
11	17	37.87
12	22	23.94
13	11	5.70
14	4	-4.72
15	13	-9.68
16	5	-18.51
17	16	-22.90
18	14	-36.34
19	7	-45.22
20	6	-52.25
21	9	-74.18
22	12	-86.10
23	15	-106.72
24	1	-120.73

Table 6.3: Cryallographic data set for α' martensite in 304 stainless steel.

Habit plane	$(-0.183989 \ 0.596344 \ -0.781359)_\gamma$
Shape deformation matrix $(\gamma \ P \ \gamma)$	$\begin{pmatrix} 0.991342 & 0.028064 & -0.036770 \\ 0.028064 & 0.909040 & 0.119180 \\ 0.029429 & -0.095386 & 1.124979 \end{pmatrix}$
Coordinate transformation matrix $(\gamma \ J \ \alpha)$	$\begin{pmatrix} 0.579356 & 0.542586 & 0.102537 \\ 0.014470 & 0.133650 & -0.788984 \\ -0.552000 & 0.572979 & 0.086936 \end{pmatrix}$

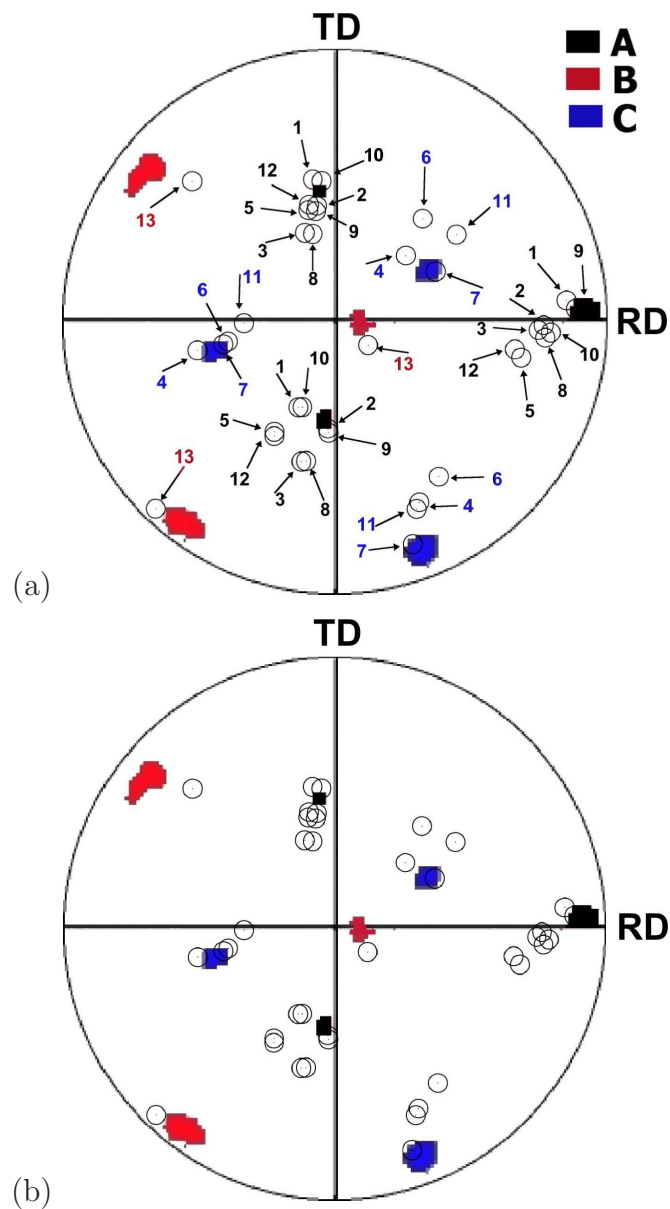


Figure 6.3: Model predicted $1\ 0\ 0_{\alpha'}$ pole figure for α' martensite. Coloured areas corresponds to experimental observation of Humbert *et al.*. Open circles represent model predictions. (a) Shows the details of predicted variants, (b) without detail.

Chapter 7

Alloy design

7.1 Introduction

Significant progress has been made in the development of welding alloys which lead to an improvement in the fatigue strength of welded structures [2, 48, 49]. The alloys exploit transformation plasticity, which compensates for thermal contraction stresses, thereby reducing the levels of residual stress in the welded construction as it reaches ambient temperature [4]. A low transformation temperature is essential in this process because if transformation becomes exhausted prematurely then residual stresses due to contraction strains are able to accumulate during subsequent cooling to ambient temperature. In some cases, a state of compressive stress is achieved at the end of the cooling process.

Previous welding alloys have achieved the required reduction in residual stress but have exhibited poor toughness [2, 48, 49]. The alloys are essentially martensitic; the achievement of a low M_S (martensite-start) temperature whilst maintaining toughness requires a difficult alloy design procedure; cost is another factor which must be considered. That aim of the present work was to optimise the composition of the weld metal without compromising

the toughness of the weld metal or the fatigue properties of welded joints. The search conducted to find appropriate weld metal compositions was much wider than reported here; only the narrow search-range associated with the final choices is documented.

7.2 Mechanical properties

The effects of various solutes and heat treatment on the mechanical properties of welds have been studied by Murugananth [88]. This work was used as a starting point for the present studies, although calculations were carried out over a much broader range of compositions in order to avoid bias. The alloy compositions selected for detailed study are listed in Table 7.1, based on the use of established neural network models to estimate toughness, yield strength, tensile strength, elongation and the martensite-start temperature [89]. The M_S temperatures were also calculated using a thermodynamic model [90, 91]. The heat treatment and other input parameters are listed in Table 7.2. The sequence A, B, and C in Table 7.1 represents an evolution of the input parameters towards an optimum composition.

Figs 7.1 and 7.2 show the calculated variation in toughness and M_S temperature with composition in the Series A alloys. It is clear from the contour plot that in the composition range where an acceptable impact toughness of 50 J is achieved, the M_S temperature is too high to take advantage of any transformation plasticity.

The results of Series B alloys are more promising. A reasonable amount of toughness is obtained along with a low M_S temperature. Figs 7.3 and 7.4 show that an alloy with 0.4 wt % Mo has an impact toughness of 55 J at -60°C with an M_S temperature of 240°C . The marked region shows the composition range of interest (12Ni,1Cr, wt %) where the desirable properties can be achieved. The uncertainty in the Charpy impact value is about 30-35

Table 7.1: The chemical compositions of trial alloys.

Alloy composition (wt%)	Series A	Series B	Series C
C	0.03	0.03	0.03-0.07
Mn	0.5	0.5	0.5
Si	0.4	0.65	0.4
Cr	0-2	0-2	0.25
Ni	1-10	2-14	6-18
Mo	0.25	0.4-1.0	0.4
V	0	0.011	0.011
Co	0	0.009	0.009
Al	0	0.02	0.02
W	0	0.005	0.005
Cu	0	0.03	0.03
Nb	0	0.001	0.001
Ti	0	0.008	0.008
B	0	0.0001	0.0001
N	0.005	0.018	0.018
O	0.038	0.038	0.038

Table 7.2: Details of heat treatment and testing conditions.

Condition	Value
Heat Input / kJ mm^{-1}	1.5
Interpass Temperature / $^{\circ}\text{C}$	250
Post weld heat treatment temperature / $^{\circ}\text{C}$	250
Post weld heat treatment time / h	16
Testing temperature for Charpy toughness / $^{\circ}\text{C}$	-60

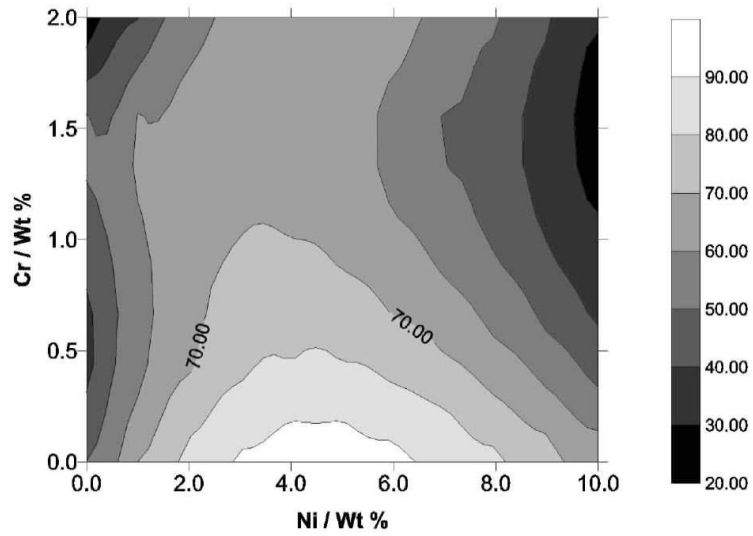


Figure 7.1: Effect of chromium and nickel on impact toughness (Joules) of Series A alloys at -60°C.

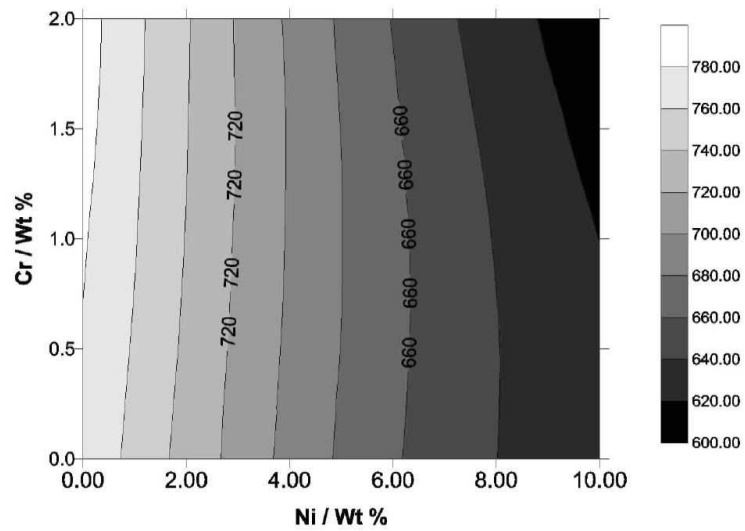


Figure 7.2: Effect of chromium and nickel on M_S temperature (K) of Series A alloys.

$J (\pm 1\sigma)$; the corresponding uncertainty in M_S is about ± 60 °C.

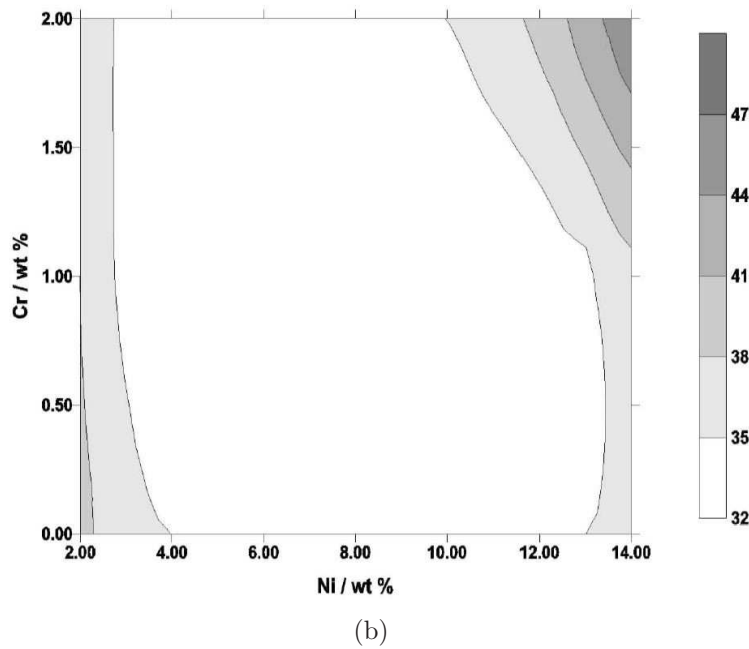
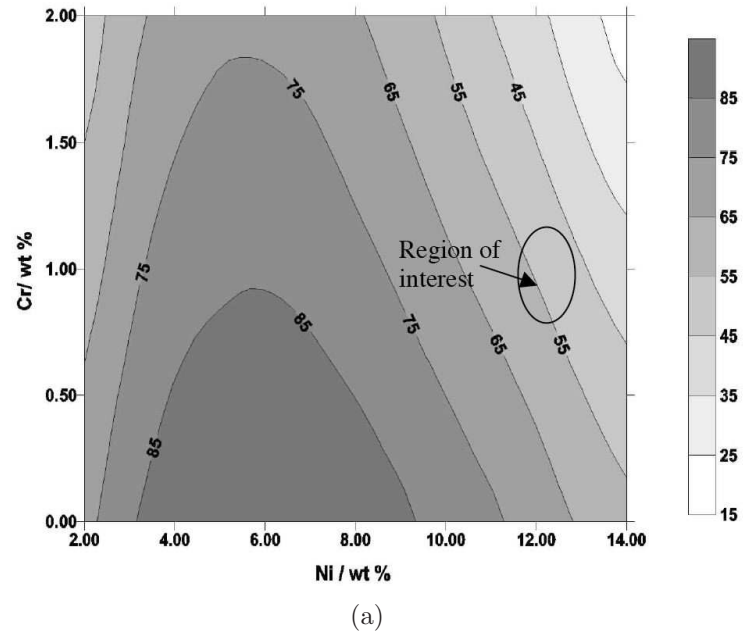
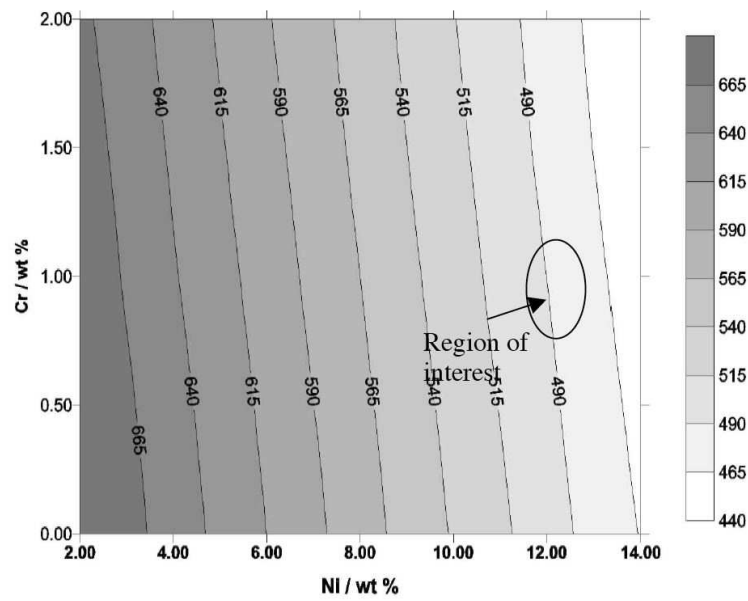
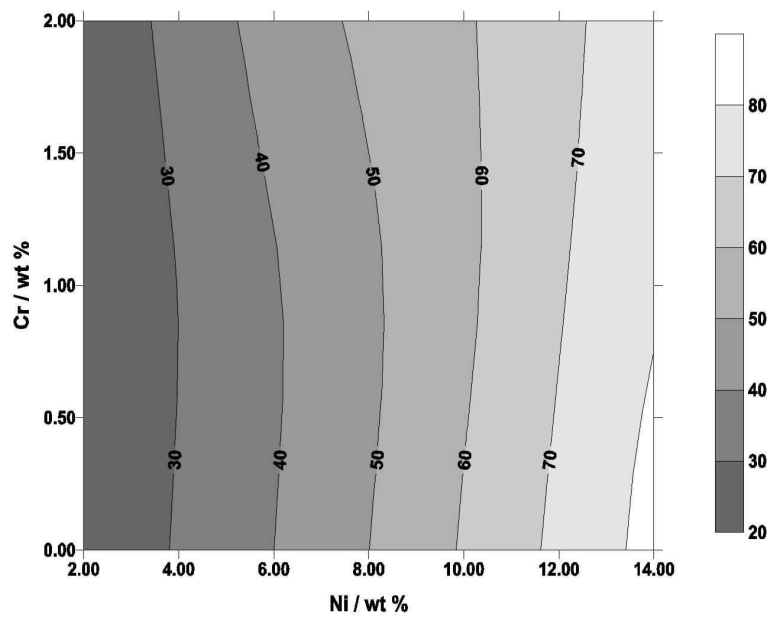


Figure 7.3: Effect of chromium and nickel on the Charpy toughness (Joules) of Series B alloys at -60°C. (a) Predictions (b) $\pm 1\sigma$ uncertainty.



(a)



(b)

Figure 7.4: Effect of chromium and nickel concentration on M_S temperature (K) of Series B alloys. (a) Predictions (b) $\pm 1\sigma$ uncertainty.

Fig 7.5 shows the variation of yield strength of the welded joints with

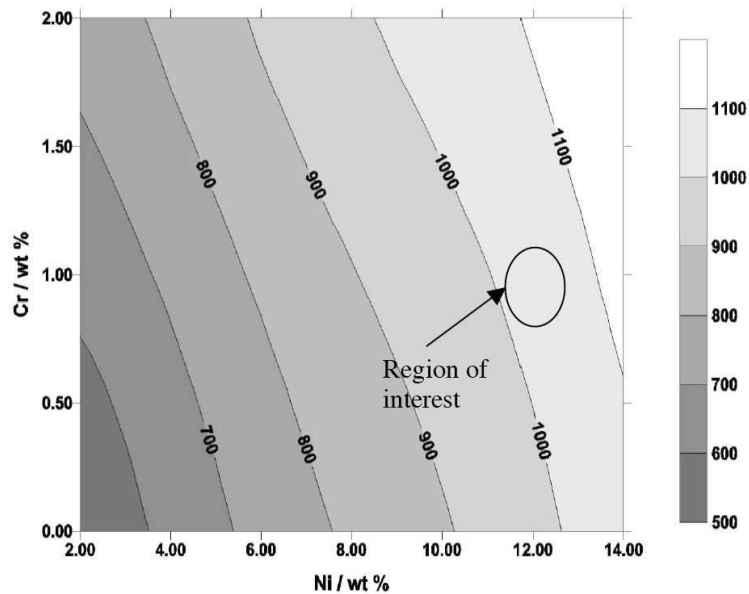


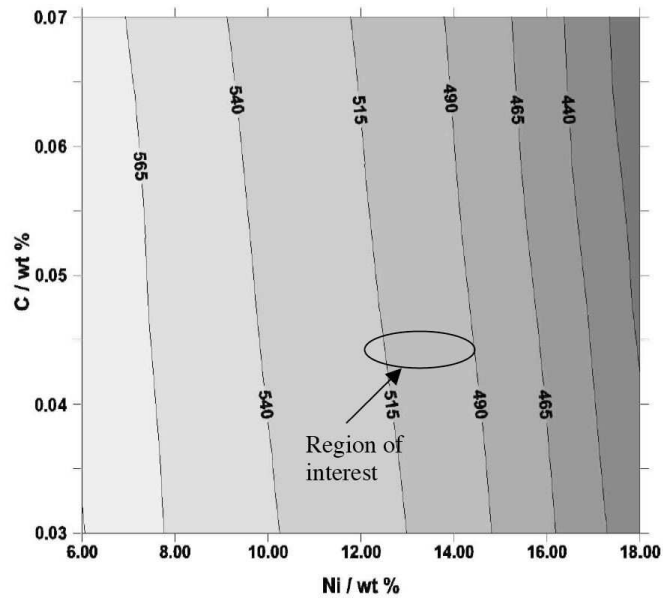
Figure 7.5: Effect of chromium and nickel concentration on the yield strength (MPa) of Series B alloys.

composition in series B alloy. It is seen that in the composition range of interest the yield strength is around 1000 MPa.

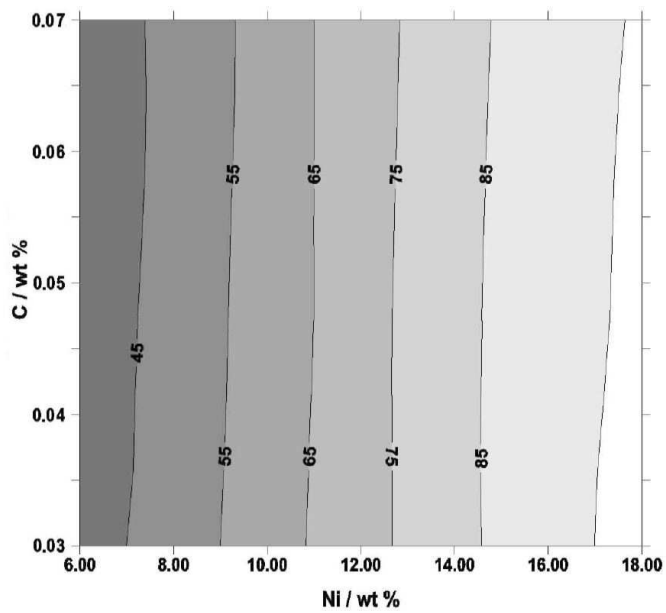
Series C is conceived on the basis of these results (Figs 7.6 and 7.7). The alloys with 0.045 wt % carbon and 14 wt % Ni, can achieve a Charpy toughness of $\sim 50 \pm 35$ J with an M_S temperature of $\sim 220 \pm 70^\circ\text{C}$.

The effect of alloying elements on the yield strength of the Series C alloys is also assessed in Fig. 7.8. As expected the yield strength increases with the Ni concentration. However, when the concentration exceeds 12 wt%, an increase in carbon causes a reduction in the yield strength. This might be caused by the retention of a greater amounts of austenite.

As the results of the M_S temperature predictions are associated with a large amount of uncertainty, the temperatures were calculated again for the Series B and C alloys using a thermodynamic model. Fig. 7.9 compares the two methods (neural network and thermodynamic); there is in general

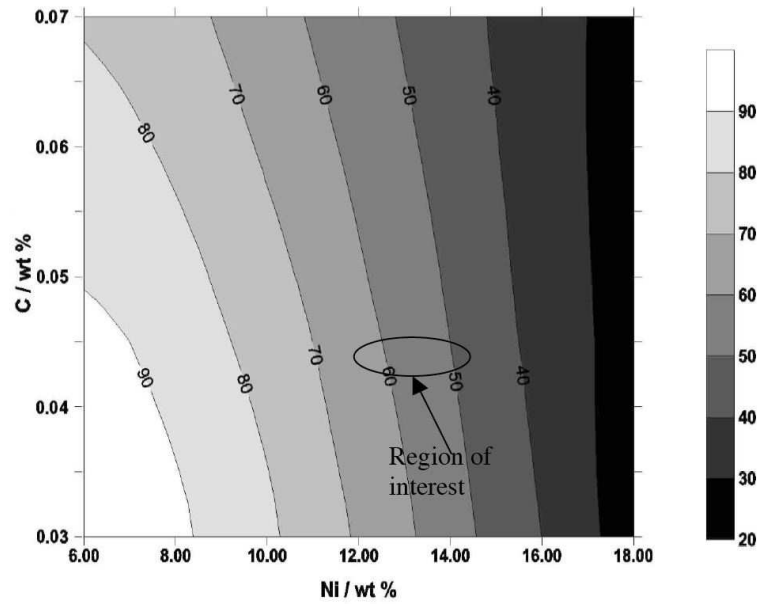


(a)

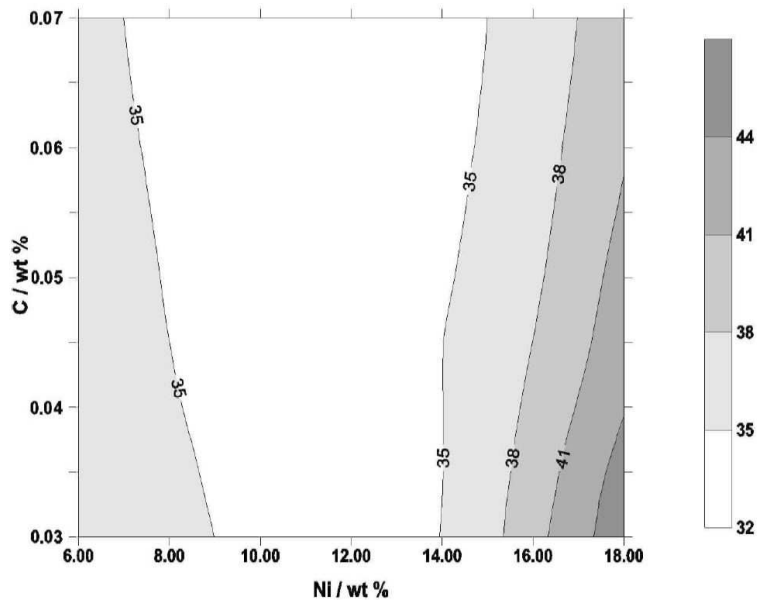


(b)

Figure 7.6: Effect of carbon and nickel concentration on M_S temperature (K) of Series C alloys. (a) Predictions (b) $\pm 1\sigma$ uncertainty.



(a)



(b)

Figure 7.7: Effect of carbon and nickel concentration on Charpy toughness (Joules) of Series C alloys at -60°C . (a) Predictions (b) $\pm 1\sigma$ uncertainty.

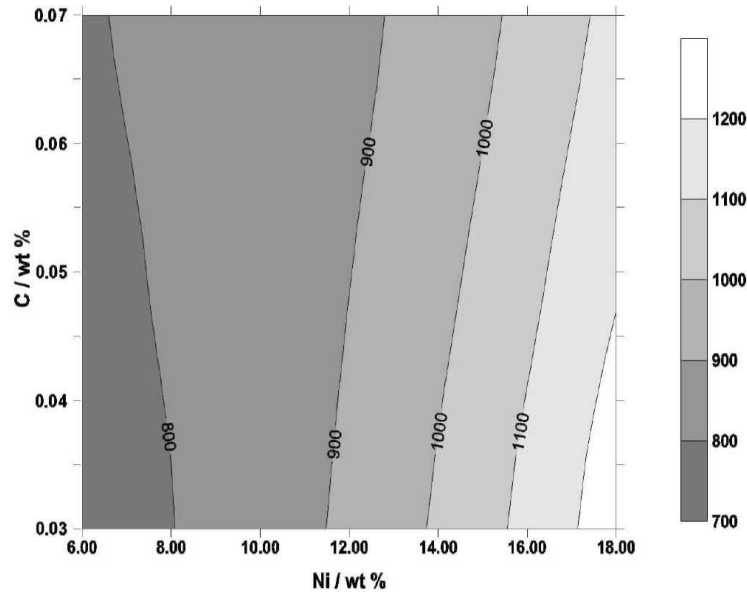
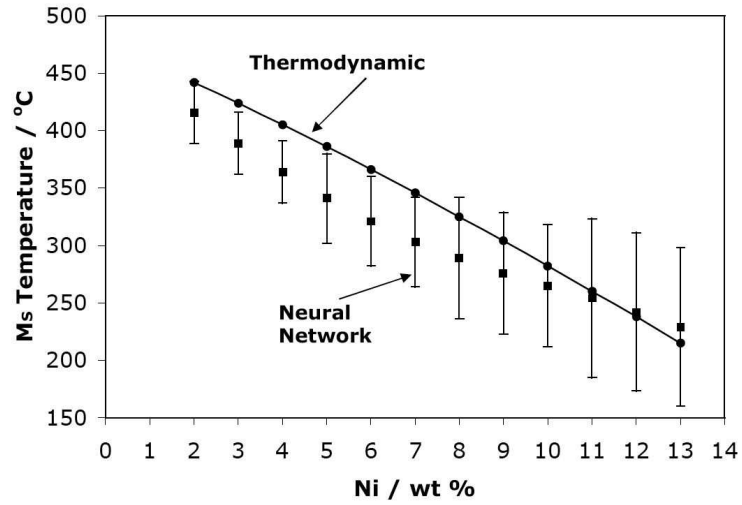


Figure 7.8: Effect of carbon and nickel concentration on yield strength (MPa) of Series C alloys.

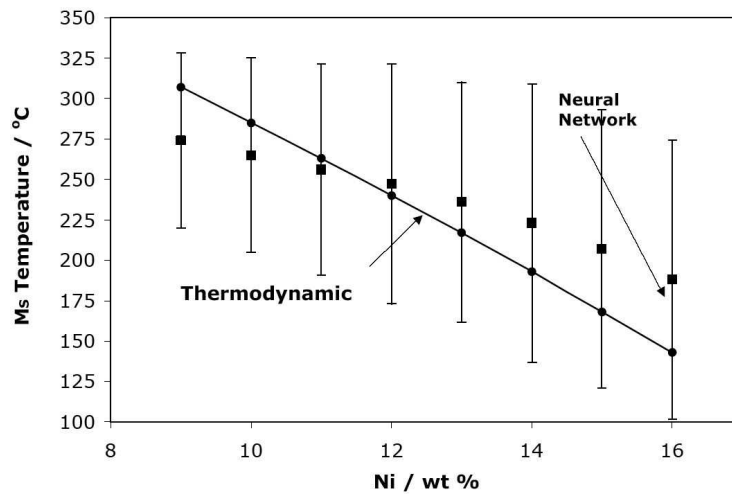
reasonable agreement, indicating that the large uncertainties associated with the network are simply warnings that the calculations are being conducted in regimes where knowledge is sparse, but that the predictions may nevertheless be reasonable.

The effect of welding heat input and the temperature for the Charpy test on the toughness values have been analysed. A greater heat input leads to a better toughness but the improvement is marginal. The analysis also shows that the Charpy value is insensitive to the test temperature (Fig 7.10). Fig 7.11 shows that as the interpass temperature increases so does the strength. An increased heat input slightly reduces the strength. For the last two analyses (Fig 7.10 and Fig 7.11) series C has been used.

From this discussion it can be concluded that both Series C and series B alloys seem to have a good combination of transformation temperature and toughness and may therefore enhance the fatigue life of the welded structures



(a)



(b)

Figure 7.9: Comparison of M_S temperature predicted using neural network model and thermodynamic model. (a) Series B alloys (b) Series C alloys.

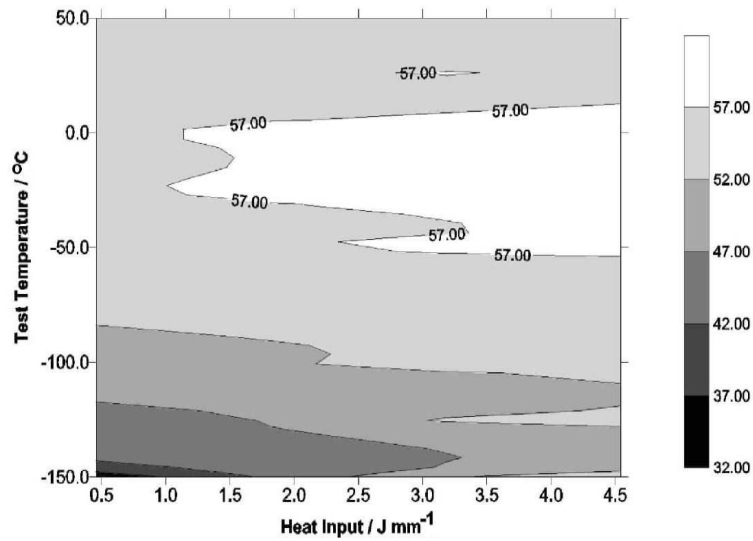


Figure 7.10: Effect of test temperature and heat input on the toughness (Joules) of the weld.

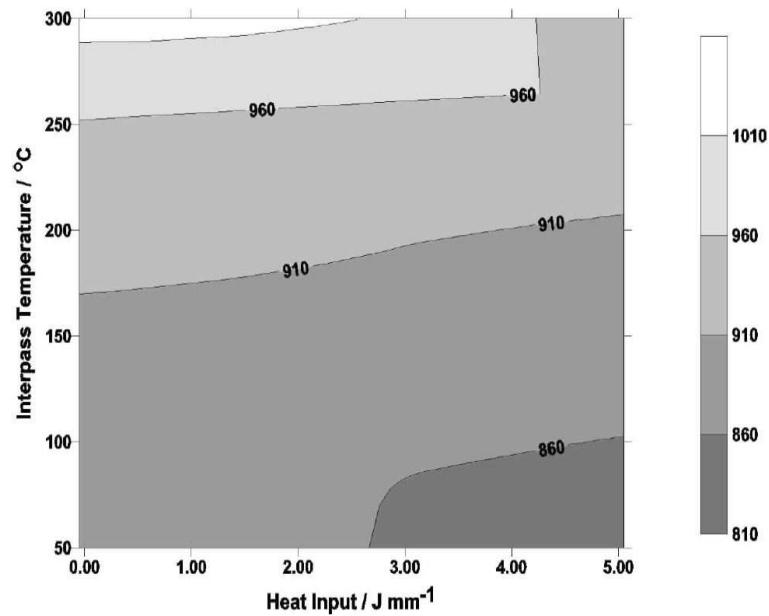


Figure 7.11: Effect of interpass temperature and heat input on the yield strength (MPa) of the weld.

whilst maintaining toughness. However, it is important to compare the properties of these materials with some alloys in which the low transformation temperature has already been exploited successfully with respect to fatigue properties [2, 48, 49, 92].

7.3 Comparison of properties

A comparison of the chemical composition and various mechanical properties of three recently developed welding alloys with the Series C and Series B alloy is presented in Table 7.3. In a few cases where the data have not been provided by the original authors, they have been calculated with the help of the neural network and/or the thermodynamic models used in the present study.

Although the composition of the alloy B206 is quite similar to that of alloy 13Cr/LC35, it has much higher impact toughness than the latter. This is because B206 is welded using a gas tungsten arc welding technique which keeps the oxygen concentration very low. Based on these model predicted results experimental welds have been made at ESAB AB (Sweden) and mechanical properties have been evaluated.

7.4 Restriction on the lowering of M_S temperature

From the above discussion it may appear that a low M_S temperature is better for the utilisation of transformation plasticity; however there may be a difficulty. The lowering of the M_S below a certain level may not allow the austenite to martensite transformation to be completed; the untransformed austenite clearly cannot contribute to transformation plasticity. The Table 7.4 shows the M_S temperature of the alloy along with the temperature

Table 7.3: Properties of various welding alloys developed to take advantage of transformation plasticity.

		Series C	Series B	Ohta [2]	B206 [50]	13Cr / LC35 [50]	OK 75.78
Comp- osition / wt%	C	0.045	0.03	0.025	0.01	0.04	0.05
	Si	0.4	0.65	0.32	0.4	0.5	0.29
	Mn	0.5	0.5	0.7	1.8	0.8	2.09
	Ni	14.0	12.0	10.0	6.7	12.3	3.04
	Cr	0.4	1.0	10.0	12.5	7.3	0.43
	Mo	0.4	0.5	0.13	2.5	2.2	0.59
	V	0.03	0.011				0.019
	N	0.018	0.018				0.01
	O	0.038	0.038				0.03
$M_S/^\circ\text{C}$	Neural Network	223 \pm 70	242 \pm 60				
	Thermo- dynamic	193	238	218	200	214	388
Charpy Tough- ness / J	Neural Network	50 at -60 $^\circ\text{C}$	55 at -60 $^\circ\text{C}$	39 at -20 $^\circ\text{C}$	100 at -40 $^\circ\text{C}$	30 at -40 $^\circ\text{C}$	65 at -60 $^\circ\text{C}$

Table 7.4: Variation of T_{90} with M_S .

$M_S / ^\circ\text{C}$	$T_{90} / ^\circ\text{C}$
400	175
350	125
300	75
250	25
200	-25
150	-75
100	-125

at which 90% martensite is obtained (T_{90}), assuming that the Koistinen-Marburger equation [51] applies. T_{90} should be as close as possible to room temperature, but not below it.

Note that the austenite, when constrained, plastically deforms prior to the martensitic transformation. It is possible that this can affect the development of the martensite, either by accelerating transformation (due to a greater number density of nucleation sites), or by retarding it through mechanical stabilisation [39]. It is also possible that martensite which forms in deformed austenite may not be randomly oriented [41], with consequences on the transformation plasticity. Fig. 7.12 represents schematically how transformation strain evolves with cooling.

The data presented in Table 7.4 show that an M_S temperature $\sim 250^\circ\text{C}$ would be ideal for the present purposes. The variation of residual stress with M_S temperature of the welding alloy is shown in Table 7.5. The data for the first two alloys (10Cr-10Ni and MSG-63B) are taken from the work done by Ohta *et al.* [2] and for the alloy 9CrMo data is taken from the work of Jones and Alberry [3]. It is clear that the residual stress at room temperature gradually decreases with lowering of the transformation temperature of the alloy. It is also clear from the trend that at sufficiently low transformation temperatures it is possible to have a residual stress which is compressive in

Table 7.5: Variation of residual stress (at room temperature) with M_S temperature as calculated by Ohta *et al.* [2] and Jones and Alberry [3].

Alloy	M_S or B_S / °C	Residual Stress / MPa
10Cr-10Ni	210	~-180
MGS-63B	620	~400
9CrMo	510	~220

nature. The reappearance of the tensile residual stress due to further lowering of M_S (T_{90} less than room temperature) could not be tested due to lack of data.

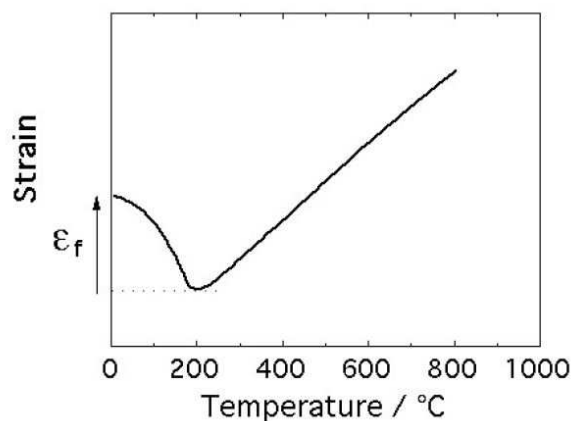


Figure 7.12: Definition of strain due to transformation.

7.5 Alloy preparation and properties

Based on the predicted properties presented in Table 7.3, three alloys have been prepared. The first two are the Series B and Series C as described earlier and the third one was prepared based on the work done by Wang *et al.* [92] and Lixing *et al.* [93], designated as LTTE3 in Table 7.6. A fourth alloy, which has been widely used as filler material with a mixed microstructure

(bainite and martensite) called OK75.78 has also been made. OK75.78 was prepared primarily to compare its properties with the newly designed alloys. All these alloys mentioned here are used as the electrode (filler) material. An ISO 2560 type joint has been prepared by welding a low carbon steel plate with the help of the newly developed filler materials. The composition of the welded plate (Weldox 960) and the chemical composition of filler alloys are given in the Table 7.6.

Table 7.6: Measured composition (wt%) of the filler material and the base plate.

Material	Name	Fe	C	Si	Mn	Cr	Ni	Mo
Plate	Weldox 960	bal.	0.2	0.5	1.6	0.7	2.0	0.7
Filler 1	OK75.78	bal.	0.05	0.19	2.01	0.41	3.14	0.63
Filler 2	LTTE3	bal.	0.07	0.2	1.25	9.1	8.5	-
Filler 3	seriesB	bal.	0.03	0.65	0.5	1.0	12.0	0.5
Filler 4	seriesC	bal.	0.03	0.55	0.57	0.34	12.3	0.48

The welding was done after buttering the sides and the base plate to avoid chemical dilution. After welding, a $15 \times 15 \times 150$ mm section was cut from the middle of the welded zone and used for preparing the samples for mechanical testing as well as for the synchrotron studies. The details are shown in Fig. 7.13.

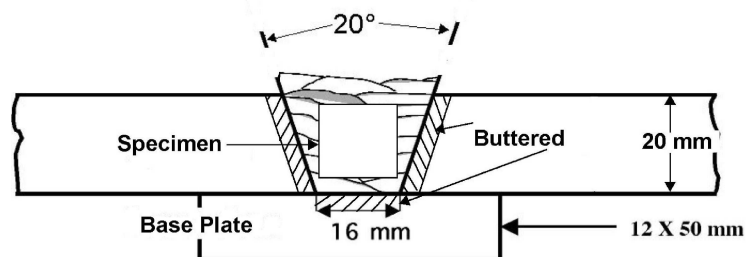


Figure 7.13: Preparation of the welded joints.

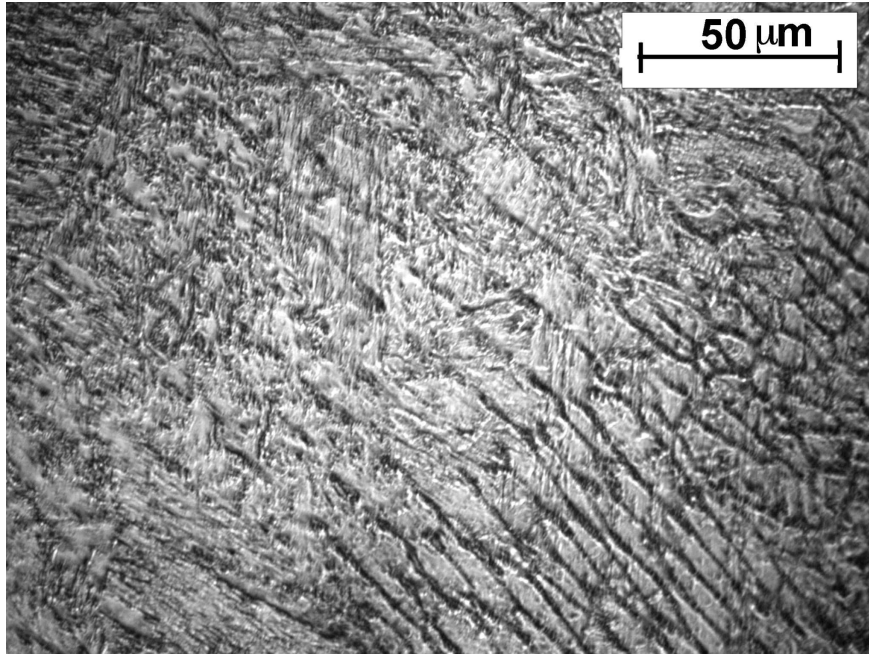
The microstructures of Series B, Series C and LTTE3 are quite similar

Table 7.7: Hardness value of Series-B alloy.

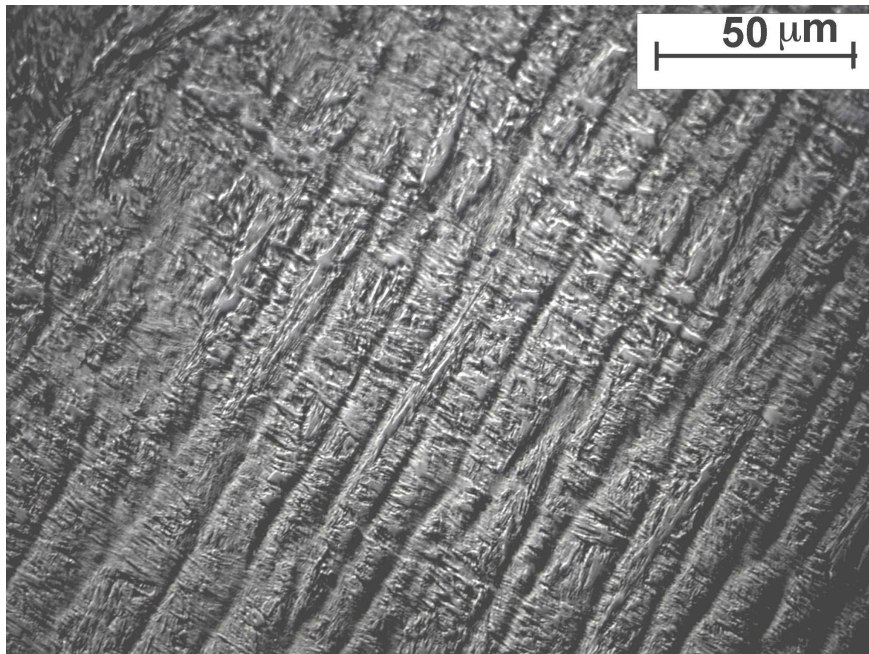
Alloy	Hardness /HV			Average hardness
Series-B (as received)	375 366	353 358	401 357	368
Series-B (quenched)	365 358	365 365	358 371	364

and shows typical dendritic structure containing very fine plates of martensite (Figs 7.14 and 7.15). Fig. 7.16 show the photograph obtained from a scanning electron microscope of the Series B alloy, at a higher magnification. It is clear from the figure that the microstructure consists of martensite plates. To further prove the presence of martensite in this alloy hardness values have been taken from the welded specimen made from Series-B filler metal and compared with the same obtained from a sample prepared from Series-B alloy after austenitising and quenching it in water. This heat treatment is certainly going to produce martensite and Table 7.7 shows the hardness obtained from the quenched Series-B alloy is almost the same as in the weld specimen. This proves that the new alloys are martensitic.

Tables 7.8 and 7.9 summarise the mechanical properties of the alloys. It shows that the newly developed alloys have satisfactory mechanical properties including a very low bending angle (described in Fig. 2.20 in Chapter 2) which is an indication of lower residual stress generation. The calculated transformation temperature values are presented in Table 7.8. The M_S temperatures were calculated following a thermodynamic model [91] and the B_S temperatures are calculated using an empirical equation [94]. It can be seen from Table 7.8 that apart from that of alloy OK75.78, all other alloys are having bainite start temperatures lower than the martensite start temperatures. It clearly indicates that these alloys are predominantly martensitic in nature, however for OK75.78 a mixed microstructure is expected, which has



(a)



(b)

Figure 7.14: Optical image of (a) Series B alloy. (b) Series C alloy.

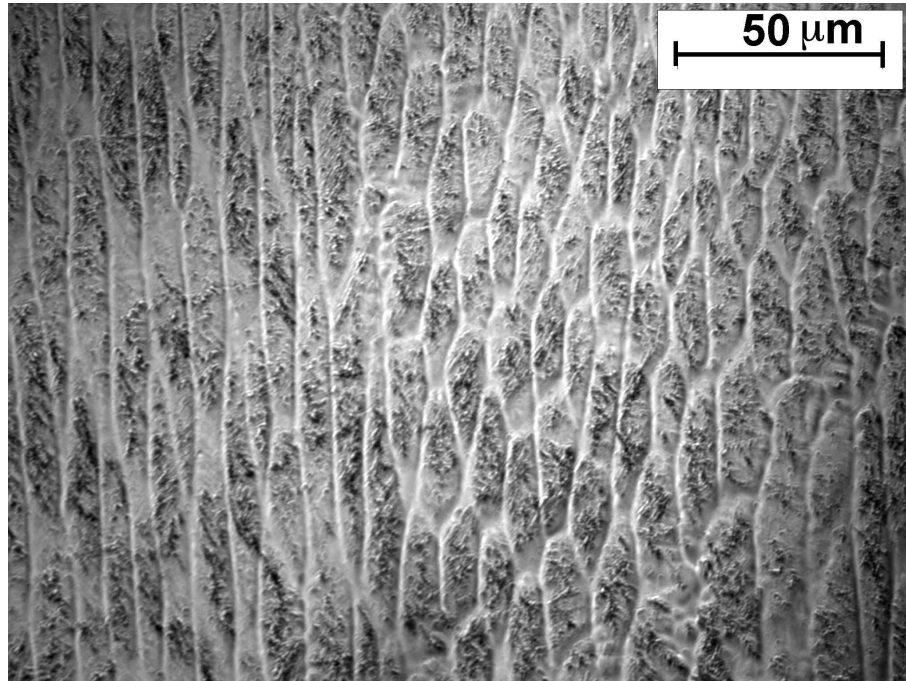


Figure 7.15: Optical image of LTTE3 alloy.

been experimentally observed by Lord [95]. It can be seen from the given data (in Tables 7.8 and 7.9) that although newly designed alloys (LTTE3, Series B and Series C) have got good properties in general but the toughness of these alloys are much lower than widely used welding alloys like OK75.78. The percentage elongation obtained for these alloys are also poor. The fractographs obtained for Series B and Series C alloy are presented in Fig. 7.17. Fractographs for both alloys show predominantly cleavage type fracture.

7.6 Summary

Neural network and thermodynamic models have been used to determine the chemical composition of welding alloys with sufficiently low transformation temperature and good toughness. Taking clues from the already published literature three different alloys have been proposed. Due to their low transfor-

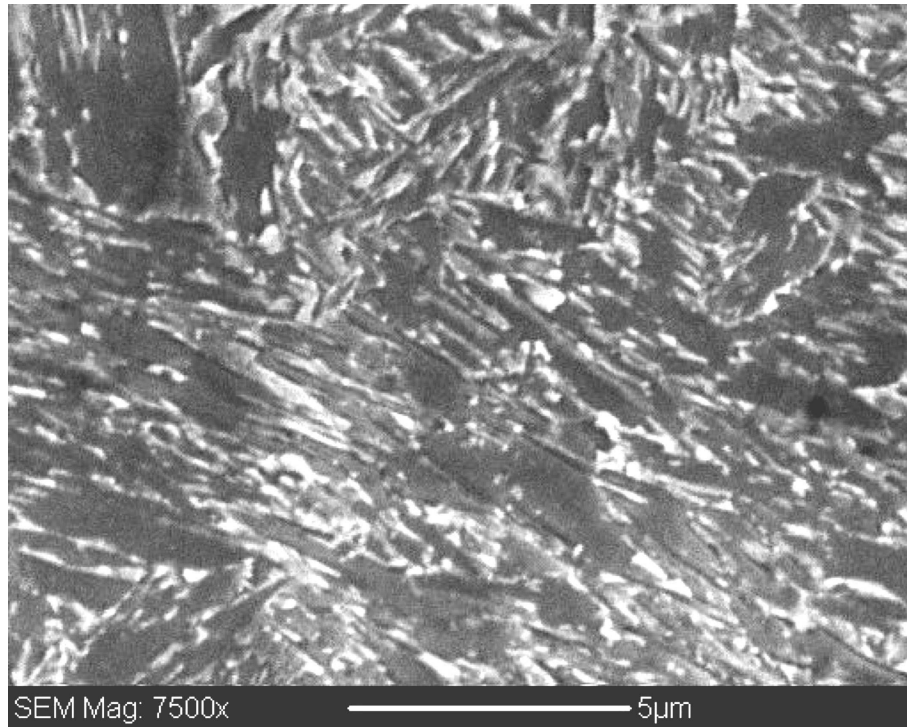
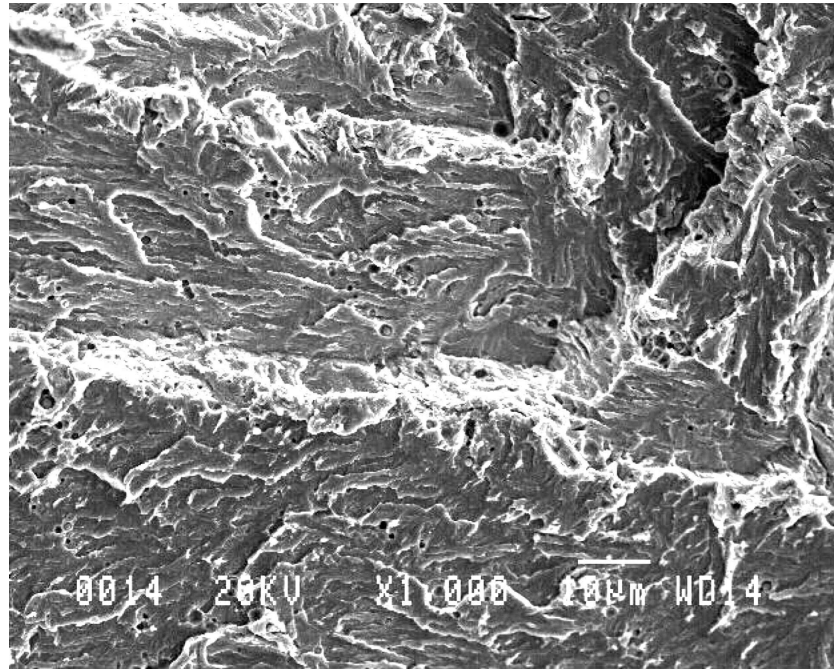


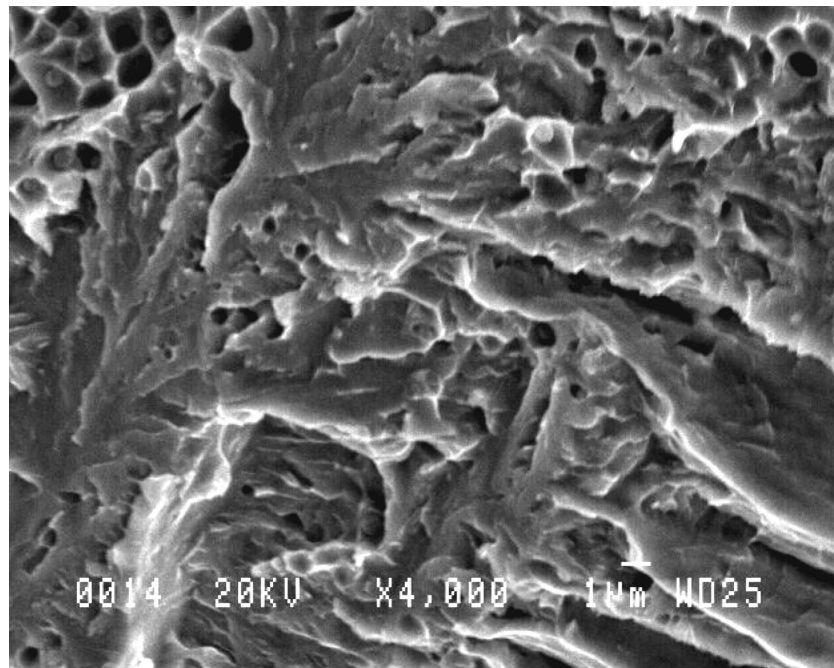
Figure 7.16: Scanning electron micrograph of Series B alloy.

Table 7.8: Mechanical properties and transformation temperature of various filler materials.

Alloy	$M_S/^\circ\text{C}$ (calculated)	$B_S/^\circ\text{C}$ (calculated)	Yield Strength / MPa	Tensile Strength / MPa	% Elongation
OK75.78	388	421	951	957	19
LTTE3	200	-264	1135	1287	6
Series C	193	169	790	958	3
Series B	238	214	600	600	0



(a)



(b)

Figure 7.17: Fractographs of (a) Series B alloy (b) Series C alloy.

Table 7.9: Charpy toughness and bending angle values for various filler materials.

Alloy	Charpy energy / J				Bending angle
	-60°C	-40°C	-20°C	+20°C	
OK75.78	65	79	90	96	6°
LTTE3	15	17	15	20	5°
Series C	28	30	32	37	3°
Series B	28	22	27	28	0-3°

mation temperatures these alloys are expected to give compressive residual stress in the welded joints and thereby improve the fatigue life. However, actual tests show that these alloys have relatively poor toughness and elongation, although better than previous low transformation temperature alloys [2]. The microstructure of these alloys are predominantly martensitic as expected from the calculated transformation temperature and hardness, the fracture surface of the broken tensile specimen for Series B and Series C alloy show cleavage type fracture.

The welded joints made with these alloys have been used for neutron diffraction and synchrotron studies as described in the following chapters.

Chapter 8

Interpretation of Debye rings from synchrotron X-rays

8.1 Introduction

Crystallographic texture can be revealed using many diffraction techniques. This Chapter deals with X-ray data from synchrotron experiments in which it is necessary to interpret Debye rings. The high intensity of synchrotron X-ray permits *in situ* experiments which makes it possible to obtain X-ray data at high temperatures. The experimental data come from alloy Series-B (Chapter 7) which is a weld metal with a martensite-start temperature of about 240°C. Both stress-free transformation, and transformation of constrained samples have been studied and modelled.

The synchrotron experiments have been done by Dr Howard Stone on an alloy designed by the author, who with Dr Stone's help performed the data analysis. The author also developed the computer model for simulating the experimental results.

8.2 Generation of diffraction pattern

Polycrystalline specimens when subjected to X-radiation, will have some crystals oriented to satisfy the Bragg condition for a variety of crystal planes. Fig. 8.1a shows an $\{h k l\}$ reflection from a Bragg oriented single-crystal; in a polycrystalline sample, this diffraction beam becomes a cone of diffracted beams as illustrated in Fig. 8.1b.

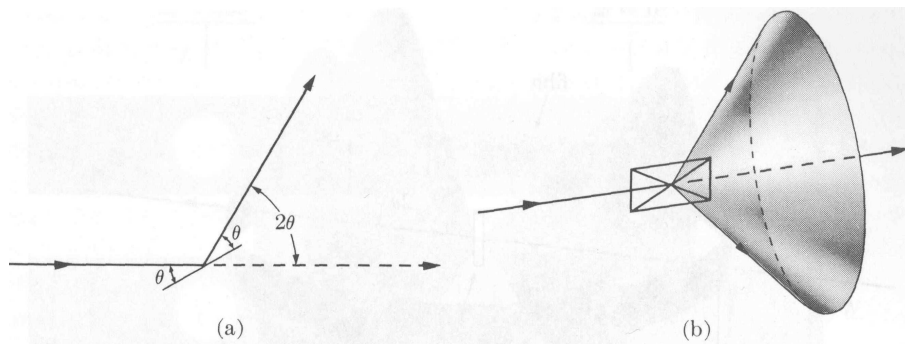


Figure 8.1: (a) Reflection from lattice plane of a single crystal. (b) The same reflection from a polycrystalline sample [24].

A flat photographic plate which is placed normal to the incident beam will reveal circles when exposed. These Debye circles will have uniform intensities along their circumferences if the crystal in the sample are randomly oriented, assuming there are sufficient crystals exposed to the incident beam. This will not be the case when sample is crystallographically textured (Fig. 8.2).

8.3 The Bragg law in reciprocal space

Fig. 8.3 shows the Ewald sphere of radius $\frac{1}{\lambda}$, where λ is the X-ray wavelength, constructed in reciprocal space. Here \mathbf{CO} is the incident beam, \mathbf{O} is the origin of the reciprocal space and \mathbf{P} defines a normal to a Bragg oriented plane.

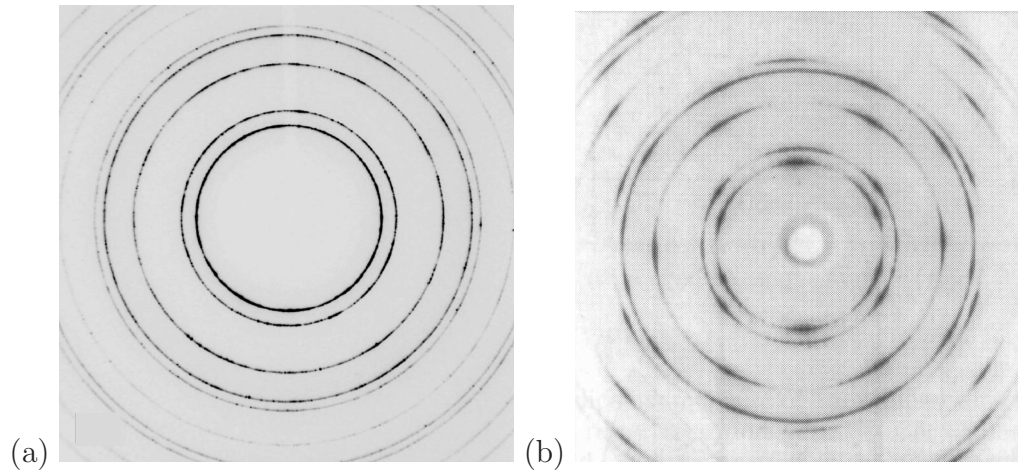


Figure 8.2: Debye rings obtained from synchrotron radiation impinging on a steel specimen. (a) A sample with negligible texture at 900°C. (b) From aluminium wire with strong crystallographic texture [96].

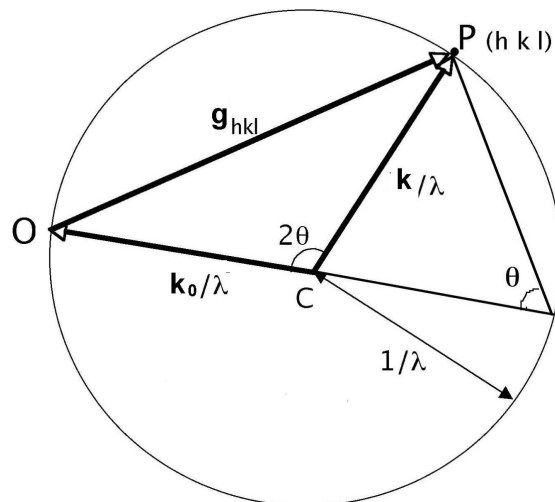


Figure 8.3: The Ewald construction to express Bragg's law in reciprocal lattice space. The Bragg angle is designated as θ .

OP thus has a magnitude of $1/d_{hkl}$ as P is a lattice point in reciprocal space.

The Bragg law is satisfied when \mathbf{OP} is also a reciprocal lattice vector since,

$$\sin\theta = \frac{OP/2}{(1/\lambda)} \equiv \frac{(1/2d)}{1/\lambda} \quad (8.1)$$

which on rearrangement gives $\lambda = 2d\sin\theta$. In vector form Bragg law is satisfied when

$$\frac{\mathbf{k}}{\lambda} = \frac{\mathbf{k}_0}{\lambda} + \mathbf{g} \quad (8.2)$$

where \mathbf{k} and \mathbf{k}_0 are unit vectors along the diffracted and incident beams respectively and $\mathbf{g} \equiv \mathbf{OP}$ is the reciprocal lattice vector representing the diffracting planes.

8.4 Construction of the model

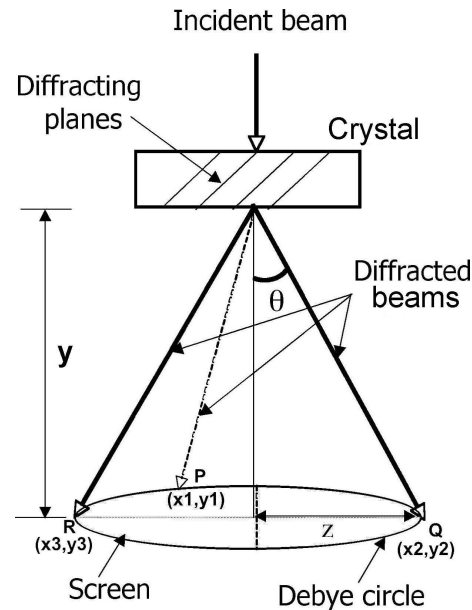


Figure 8.4: Sample orientation with respect to the incident beam and formation of the Debye circle .

In Fig. 8.4, z is the radius of the circle, y is the distance of the sample

from the receiving screen and θ is the Bragg angle. The incident beam \mathbf{k}_0 is assumed to always be parallel to the $[0\ 0\ 1]_S$ direction of the sample reference frame identified with the basis symbol ‘S’. Its components can be transformed into the crystal reference frame of a grain of austenite using $(S\ J\ \gamma)$,

$$(\mathbf{k}_0; \gamma^*) = (\mathbf{k}_0; S^*)(S\ J\ \gamma) \quad (8.3)$$

Here the symbol ‘*’ refers to the reciprocal basis. Given \mathbf{k}_0 and \mathbf{g}_{hkl} , equation 8.2 can be used to calculate \mathbf{k} . In the computer program equation 8.2 is assumed to be satisfied if the diffracting vector \mathbf{CP} has a magnitude within $\pm 2\%$ of the value of $1/\lambda$. The diffracted beam is then expressed in the sample reference frame:

$$(\mathbf{k}; S^*) = (\mathbf{k}; \gamma^*)(S\ J\ \gamma) \quad (8.4)$$

The locus (x,y) of the points like P, Q, R etc have been calculated following the simple geometry shown in Fig. 8.4. This is done for all the austenite crystal to generate points which form the Debye ring. For diffraction from martensite, the diffracted beam is first transformed into the γ reference frame and then into that of the sample.

$$(\mathbf{k}; S^*) = (\mathbf{k}; \alpha^*)(\alpha\ J\ \gamma)(\gamma\ J\ S) \quad (8.5)$$

For each austenite grain there are 24 possible $(\alpha\ J\ \gamma)$ matrices originating from 24 possible martensite variants.

8.5 Experimental procedure

Samples were tested using a thermo-mechanical testing rig mounted on the ID11 beam line at the European Synchrotron Radiation Facility in Grenoble,

France. The sample is heated via a direct current applied across it through water-cooled brass grips. With a uniform volumetric heat generation rate, this should produce a parabolic temperature distribution along the 16 mm length of the exposed sample.

To control the temperature, a type-R thermocouple was ball-ended with an oxy-acetylene torch and spot welded on to the surface at its mid-length. This is the position at which the peak temperature occurs. To limit the effect of temperature gradients across the diffraction gauge volume slits positioned in the incident beam path were used to define a 400 micrometer wide beam at the centre of the sample, giving an anticipated 2°C variation in the region illuminated by the X-ray beam at a mean temperature of 900°C.

To further ensure correspondence between the measured temperature and that encountered in the diffraction gauge volume the sample, the test rig was translated horizontally across the beam until the centre of the thermocouple bead was located from the observed diffraction patterns. The sample was then translated vertically such that the diffraction gauge volume was immersed in the sample directly below the centre of the thermocouple bead, at a point at which no further diffraction signal was detected from the thermocouple.

A nominal photon energy of 50.5 keV was selected using a double Si{111} monochromator. Diffraction data were acquired with a FReLoN (Fast-Readout Low-Noise) camera system possessing 2048 × 2048 channels of 46.8 × 48.1 μm. The camera was mounted downstream of the sample with its centre roughly aligned with the transmitted beam. In this position the full Debye-Scherrer rings could be captured for reflections with 2θ diffraction angles less than 13°. This range covered the first four reflections from ferrite and the first five from austenite. Incomplete diffraction data was also acquired towards the corners of the field of view of the camera to a 2θ diffraction angle of 19°.

To eliminate contributions from the background signal, a long exposure image was acquired in the absence of a sample and the recorded intensities scaled for direct subtraction from the subsequent diffraction images acquired.

The camera length and incident beam wavelength were determined to be 188.1 mm and 0.2453 Å respectively through calibration against a lanthanum hexaboride standard powder sample of known lattice parameter, in a glass capillary positioned in place of the sample in the testing rig. This also enabled the centre of the diffraction pattern on the detector to be unambiguously determined.

To monitor the effect of applied loads on the development of texture, samples were subjected to a thermal cycle consisting of a heating to 900°C at 10°C s⁻¹, an isothermal dwell of 60 s at 900°C and continuous cooling back to ambient at 10°C s⁻¹. During the first part of this thermal cycle, the mechanical stage was run under load control with a set point of zero load thereby permitted free thermal expansion and contraction of the samples. During cooling the mechanical stage switched to load control and a load of between 90 MPa and 311 MPa was applied to the sample (at ~ 410°C). This temperature is sufficiently above the martensite start temperature to avoid initiating a stress-induced transformation during loading and sufficiently low to limit any plasticity in the austenite.

Diffraction images were acquired in 1 s intervals with 0.5 s exposures. Processing of the raw diffraction images were done using the Fit2D image processing software [97, 98], correcting for spatial distortion inherent in the camera system [99, 100] and the efficiency of the detector pixels. The background signal was removed by subtraction of the scaled image gathered in the absence of the sample.

8.6 Results and Discussion

Experimental results show that there is no texture formation in austenite or martensite at zero load. This is expected as without loading there is no chance of any deformation texture formation in austenite. Martensite will also not have any texture as the texture of martensite originates from the bias in the orientation of austenite or due to variant selection due to externally applied load. A similar result, as observed in the sample transformed without external load, has been obtained for the sample transformed under a constant stress of 222 MPa. The Debye circles obtained from austenite and martensite (at 400°C and room temperature respectively) are shown in Fig. 8.5, it is clear from this figure that no texture is present in austenite, possible reason behind this is the applied stress is below the yield strength of the material. However when a 311 MPa stress is applied austenite develops deformation texture and subsequently the martensite also developed texture as shown in Fig. 8.6. The stress in this case is beyond the yield stress and plastic deformation leads to formation of deformation texture in austenite. Martensite, when it transforms from textured austenite also has a bias in orientation.

Deformation texture of austenite is a mixture of various texture components and for predicting the martensite texture it is necessary to know the percentage of each texture component in austenite. Copper, Goss, Brass, Cube are the common texture components of austenite, for these components the orientation relationship between the sample and the crystal axes are also well known. However it is not known how the Debye circle should appear if it forms from austenite having any one of the texture components mentioned above.

Fig. 8.7 shows the model predicted Debye rings for austenite containing either Copper or Goss or Brass or Cube component only. It is clear from this figure that none of these components can fully describe the experimentally

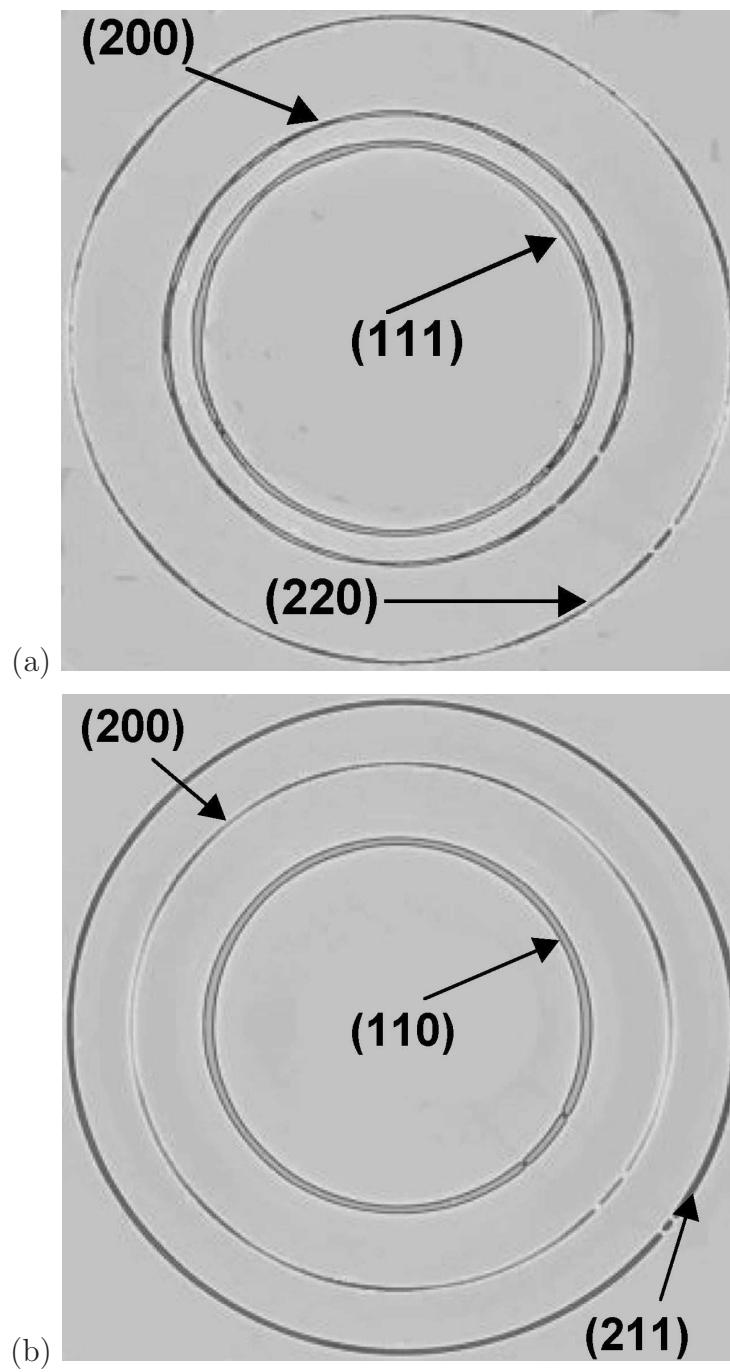


Figure 8.5: Debye rings of austenite and martensite obtained at 400°C and room temperature respectively with a load of 222 MPa. (a) Austenite. (b) Martensite.

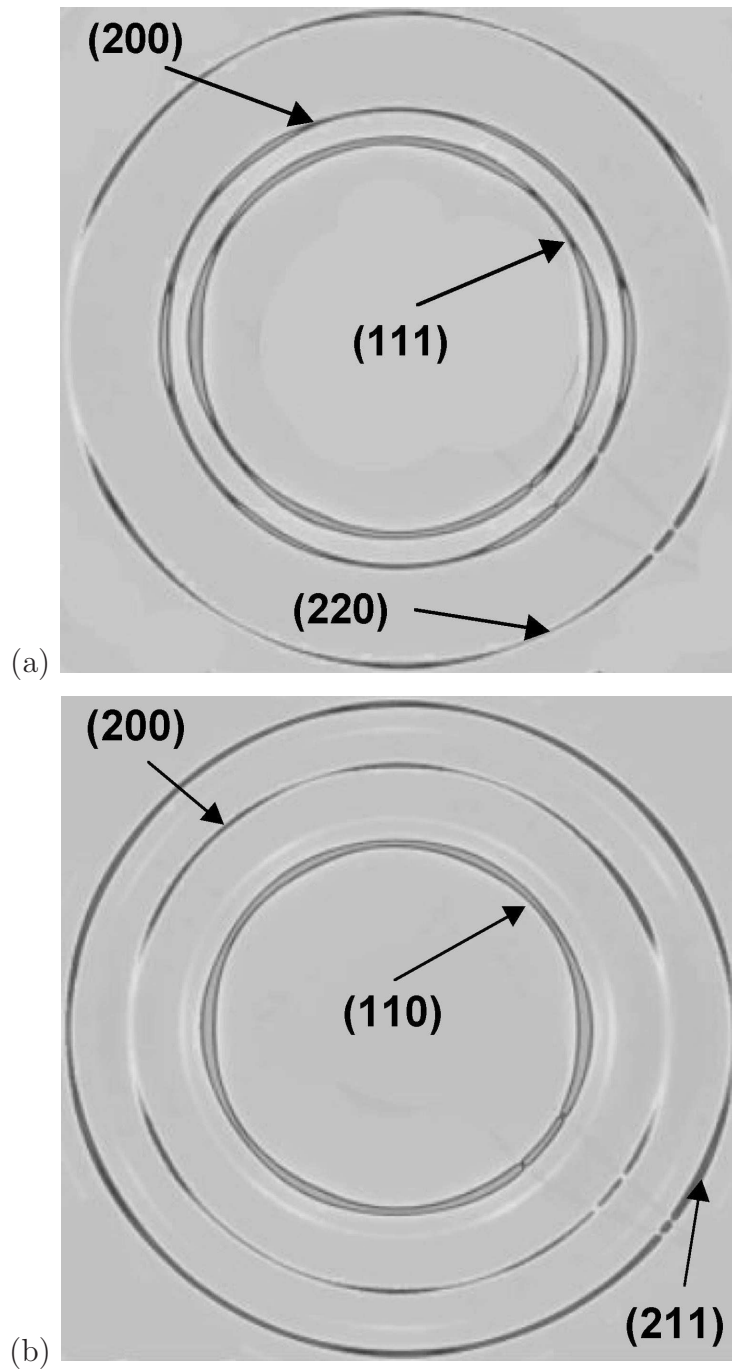


Figure 8.6: Debye rings of austenite and martensite phase obtained at 400°C and room temperature respectively with a load of 311 MPa. (a) Austenite. (b) Martensite.

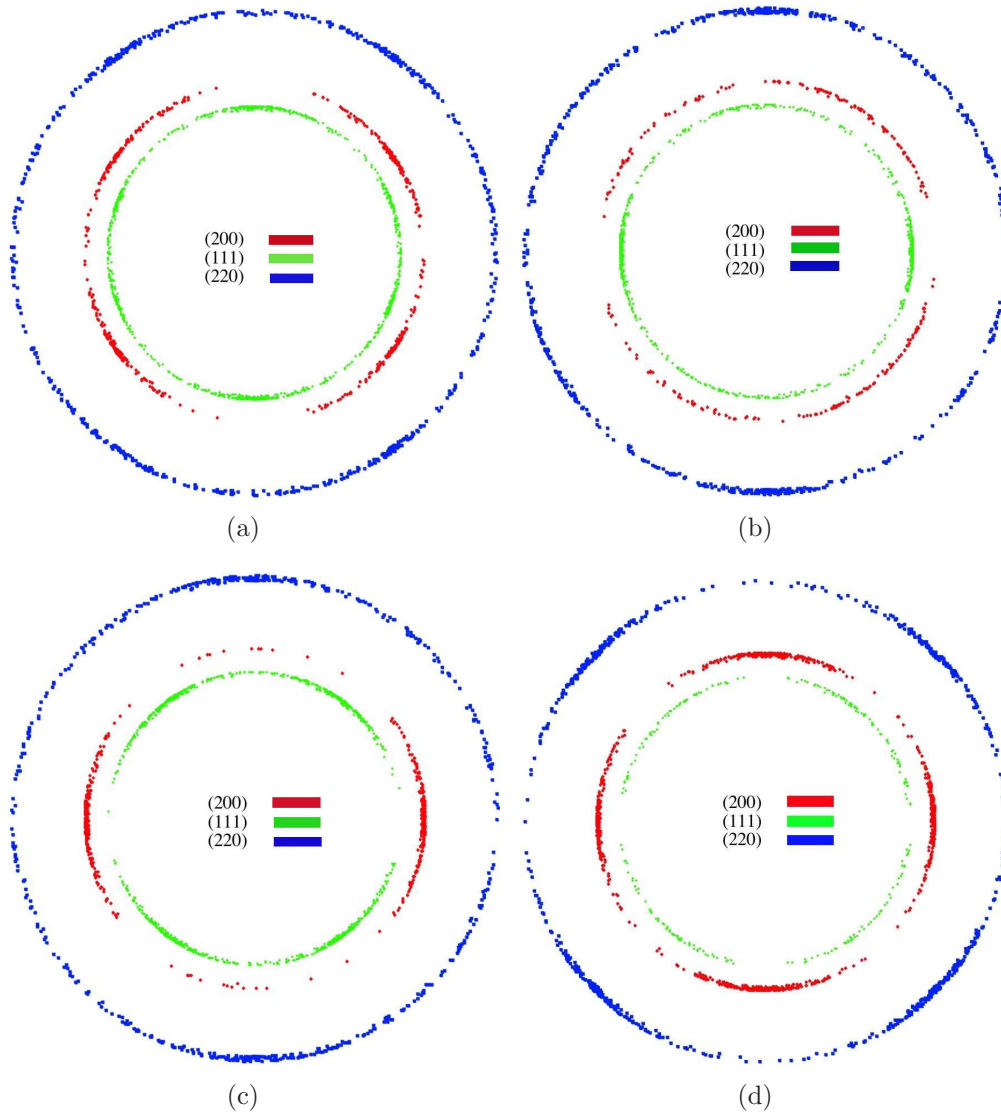


Figure 8.7: Model generated Debye ring for austenite having (a) Brass (b) Copper (c) Goss and (d) Cube texture.

observed austenite texture. This is because the austenite texture is a mixture of various possible texture components. As in this work the deformation texture of austenite is not modelled, to get the match between the experimental and the model predicted Debye circle for the austenite phase, many possible combination of texture component were tried. It can be seen that

the experimentally observed texture matches well with the model prediction (Fig. 8.8) when the austenite texture is assumed to have a combination of 70% copper and 30% Goss component.

This observation is similar to what has been found by Grigull [101] in a AISI 304 stainless steel. Taking this as the initial austenite texture, prediction has been made for the martensite phase. The variant selection model follows Patel-Cohen [12] as described in Chapter 3. From Fig. 8.9 it is clear that the model predicted Debye circle for martensite has reasonable match with the experimental one.

From Table 8.1 it can be seen that in most of the grains first 7/8 variants have mechanical free energies which is within 45% of the highest mechanical free energy available for that grain. So it was decided that in the simulation first eight most favoured variants will be considered to form in each γ grain.

There is an interesting observation. As there is no texture in the austenite loaded up to 222 MPa, it can be argued that the yield strength of austenite at 400°C is at least 222 MPa. Transformation then is stress induced with texture formation due to variant selection. However that is not observed. The reason behind this is twofold. Firstly, the texture from stress induced martensite in randomly oriented austenite will be weak, and secondly the technique is not sensitive enough to measure such weak textures. But when the austenite has some deformation texture and martensite forms under the influence of both stress and strain there should be a stronger transformation texture, which is visible from the Debye rings formed at 311 MPa load. Theoretical evidence in favour of this argument has also been shown in section 5.6.

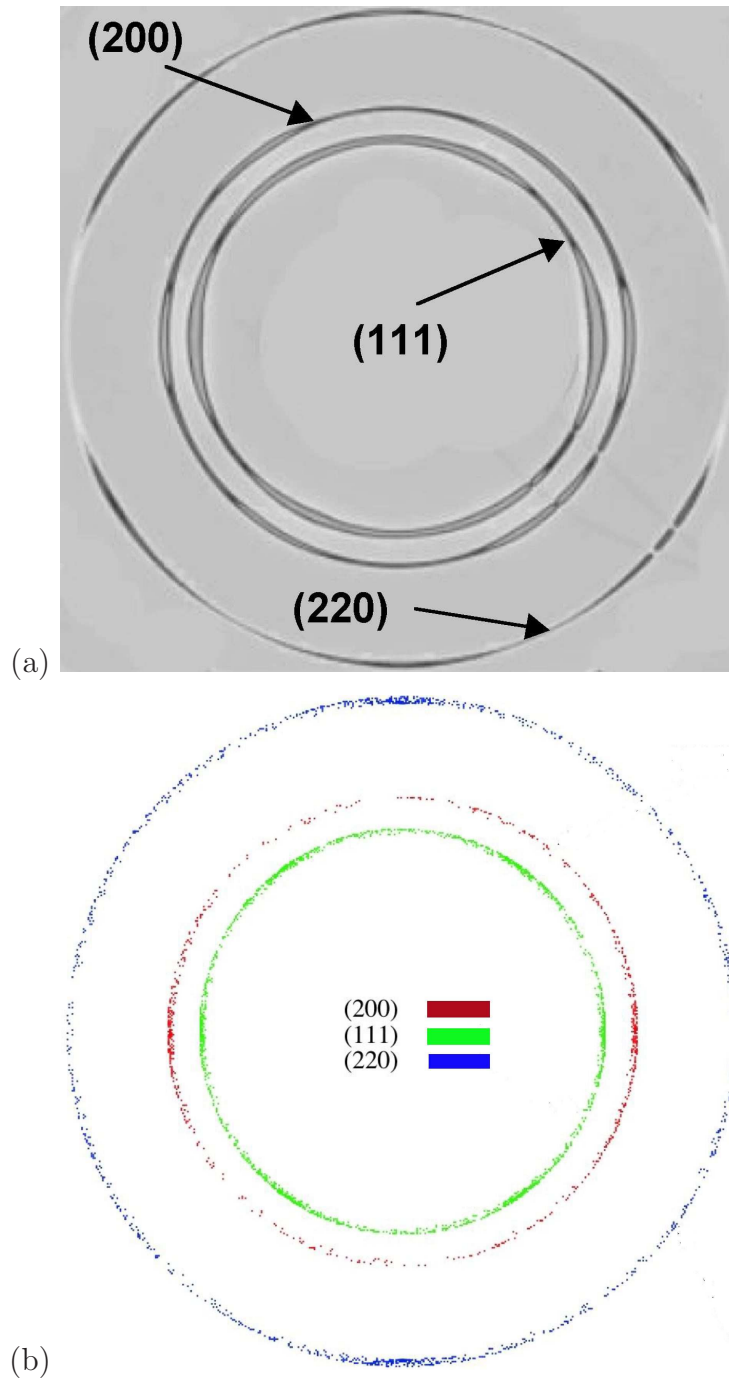


Figure 8.8: (a) Experimental and (b) model generated Debye ring for austenite having 70% Copper and 30% Goss component.

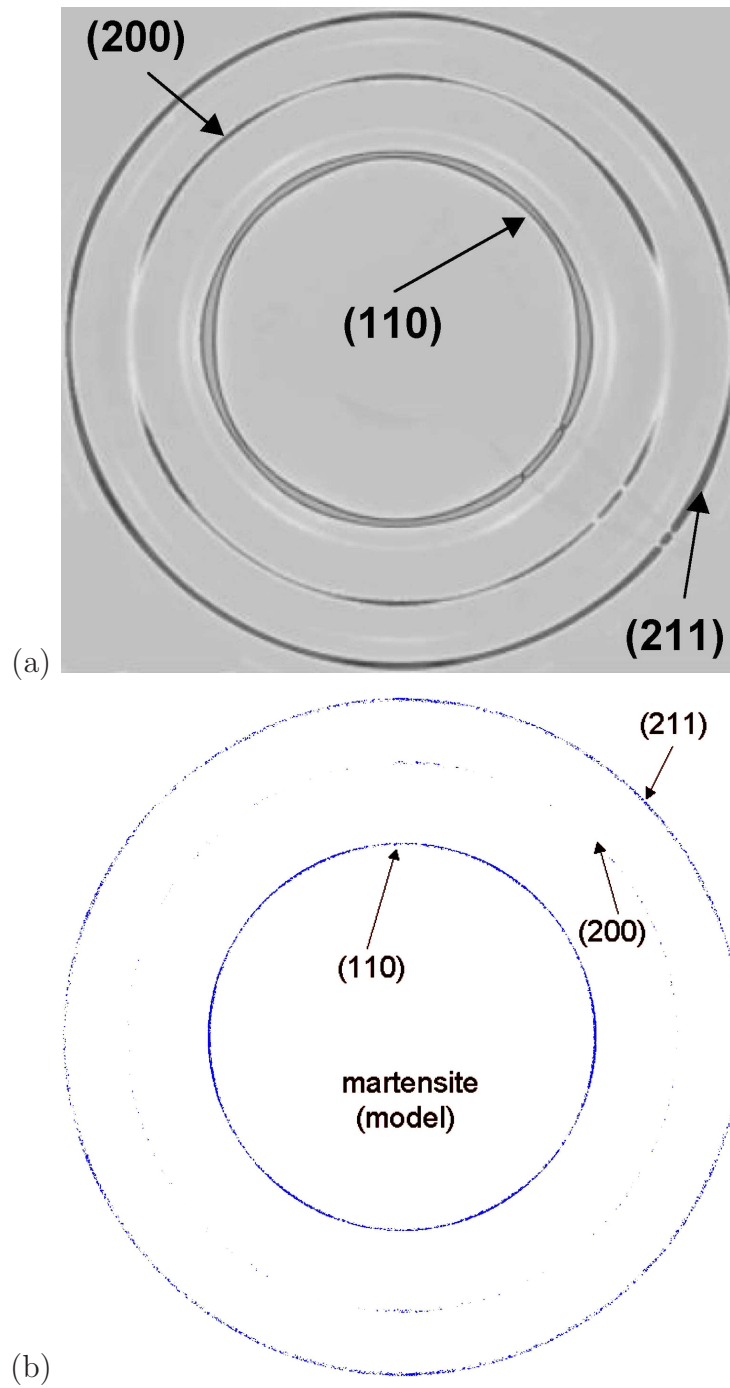


Figure 8.9: (a) Experimental and (b) model generated Debye ring for martensite transformed from austenite having 70 %Copper and 30% Goss component.

Table 8.1: Interaction energy U (J mol^{-1}) for a uniaxial tensile stress of magnitude 311 MPa, for each of the 24 possible variants of martensite in four grains of austenite chosen arbitrarily from an aggregate of 500. The energies are arranged in descending order, with positive values corresponding to a favourable interaction with the applied stress and *vice versa*.

Grain 1		Grain 2		Grain 3		Grain 4	
Variant	U	Variant	U	Variant	U	Variant	U
16	235.6	20	109.7	20	117.8	19	140.8
14	235.5	2	102.4	4	107.7	7	139.1
7	227.3	21	85.8	21	101.9	17	115.2
19	220.4	4	75.7	5	93.1	16	112.1
6	219.7	10	74.1	2	86.3	24	94.4
24	217.6	5	57.4	1	70.1	14	92.4
17	181.9	19	55.6	18	65.5	2	59.9
22	176.9	18	51.0	11	52.4	1	55.1
12	39.0	1	48.4	10	51.0	10	46.8
9	31.9	3	42.7	12	34.4	22	45.4
1	28.5	17	36.3	3	29.4	6	42.7
15	18.2	7	35.6	23	22.6	12	41.7
2	-2.6	12	18.3	19	20.4	20	10.4
10	-3.1	16	8.9	7	14.3	4	7.3
3	-94.3	11	3.6	13	10.8	3	-15.8
8	-97.1	23	3.2	9	9.9	21	-20.4
4	-102.5	8	-7.5	17	1.2	5	-22.4
11	-110.7	24	-25.4	16	-6.5	9	-23.2
20	-126.8	9	-26.4	8	-23.8	8	-52.2
21	-130.0	13	-38.5	15	-42.9	15	-59.4
5	-141.6	14	-47.1	24	-74.3	18	-69.4
13	-150.9	22	-66.5	14	-80.7	11	-74.9
18	-219.1	15	-74.8	22	-111.3	23	-115.3
23	-223.3	6	-92.2	6	-118.6	13	-119.7

8.7 Summary

A modelling method to predict the Debye rings obtained from X-ray diffraction has been presented. The model is capable of predicting the transformation texture of martensite from a given austenite texture. The variant selection has been modelled following the Patel and Cohen theory. The results obtained from the model tally well with the experimental findings. This modelling technique is new and can be of very good use for primary and quick analysis of texture with synchrotron X-ray. Debye rings obtained from common deformation textures have been modelled and presented which might be used as a data base for future studies. The experimental result indicates that Debye rings are not good enough for presenting weak texture that might form due to variant selection in martensite. For such textures it is also necessary to obtain the pole figure or orientation distribution function from the synchrotron X-ray data.

Chapter 9

Conclusions and future work

Models have been developed to show how variant selection during transformation can lead to transformation plasticity on a macroscopic scale under different types of loading conditions. It is thus possible to calculate both the development of crystallographic texture and the macroscopic strains due to selective transformation, in a manner consistent with the crystallographic theory of martensite and various criteria for the interaction of stress with crystallographic texture. These models have been validated with measured strains in a bainitic alloy transforming under uniaxial compressive stress. The influence of austenite texture on the strain developed has been discussed in detail. It has been shown that transformation strain is equal to the volume strain when all the possible variants form but that the shear strain manifests when there is variant selection.

In both polycrystalline and single crystal samples of austenite, variant selection occurs in a manner consistent with Patel and Cohen's theory [12] which emphasises a mechanical component of free energy. A partly empirical method has been proposed to estimate the extent of variant selection, which shows that the severity of variant selection is a function of the ratio of the mechanical to the chemical free energy change.

To predict the crystallographic texture and transformation strain in a

self-consistent manner a crystallographic data set is required which includes the precise orientation relationship, shape deformation, habit plane and displacements associated with the transformation. These data are mathematically related and a neglect of one or more of these parameters, or of the relationship between them, leads to an improvised analysis. The required data can be measured or generated using established martensite crystallography. It is interesting that some aspects of resulting predictions are not sensitive to whether the transformation product is martensite or bainite, in the context of inaccuracies in measurements based on the orientation imaging technique.

An effort has been made to separate out the effects of stress and strain on the texture and variant selection during displacive transformation. Variant selection can be governed by stress either externally applied or which resides in the material as a consequence of inhomogeneous plastic deformation of the austenite. Strain can have a separate influence by developing an orientation bias in austenite.

Transformation texture is naturally sensitive to the nature of the applied stress-tensor acting on the austenite and its orientation relative to the austenite. So for complex rolling conditions a complete model must be developed which is capable of realising the effective stress state at any point during rolling. Only then it is possible to predict the final texture correctly.

There have been suggestions that the transformation of austenite should be caused in two stages, first involving the formation of ϵ -martensite, followed by its decomposition into α' martensite. It has been demonstrated that this is not necessary and that only the austenite and final α' need to be considered in the calculations. This has the advantage of reducing the complexity of the problem and at the same time reducing arbitrary choices in variant selection procedures.

The infinitesimal elastic deformation approach [7] for calculating an

interaction energy between martensite and applied stress has been shown to be identical with the Patel-Cohen approach with the proviso that the former is incorrect by a factor of 2 since the strains are assumed to be elastic.

Consistent with the published results, welding alloys with low transformation temperature have been found to be capable of compensating for thermal contraction strains. Further work is necessary to improve their toughness.

Synchrotron data have been obtained for martensite transformation under stress. The resulting texture has been shown to be consistent with model predictions.

Appendix A

Residual stress measurement

A.1 Introduction

It was possible to reduce the harmful residual stress formation during welding using low transformation temperature weld filler metals designed by Ohta *et al.* [2, 48, 49] and others [92, 93]. Two new alloys have also been designed during the course of this project (Series-B and Series-C, as mentioned in Chapter 7) to take full advantage of transformation plasticity in order to reduce the residual stress formation during welding. Experimental welds have been prepared using filler metals having a variety of transformation temperatures and the residual stress was measured with the help of neutron diffraction technique. The results give a detailed insight of the nature of residual stress generation in welded joints.

The experiments were done in collaboration with the University of Manchester on three alloys, one of which was designed by the author (other two are well established welding alloys). Drs Howard Stone and John Francis carried out all the experiments and assisted the author in the analysis of data.

A.2 Experimental details

A.2.1 Filler metals

Three filler metals were chosen so that their martensite-start (M_S) temperatures varied significantly. The first filler metal, OK75.78; is a relatively low-alloy product that is available commercially [95], which should complete transformation before ambient temperature is reached. The second filler metal, LTTE3, was recently proposed by Wang *et al.* [92] as being suitable to achieve a low M_S temperature [3]. Finally, the third filler metal, designated Series-B, was designed during the course of this study as an alternative to the LTTE3 filler metal having an intermediate transformation temperature. The approximate composition of each filler metal is summarised in Table A.1 below. The transformation temperatures of these alloys are given in Table 7.7.

Table A.1: Composition (wt%) of the filler metals and the base plate.

Material	Name	Fe	C	Si	Mn	Cr	Ni	Mo	Cu
Plate	Weldox 960	bal.	0.2	0.5	1.6	0.7	2.0	0.7	0.3
Filler 1	OK75.78	bal.	0.05	0.19	2.01	0.41	3.14	0.63	-
Filler 2	LTTE3	bal.	0.07	0.2	1.25	9.1	8.5	-	-
Filler 3	Series-B	bal.	0.03	0.65	0.5	1.0	12.0	0.5	-

Bainite does not occur in the LTTE and Series B alloys which are martensitic. Note that the shape deformations due to bainite and martensite are essentially identical so for the present purposes it is only important to focus on the transformation temperatures.

A.2.2 Manufacture of the welded plates

Three rectilinear plates ($375 \times 200 \times 12$ mm) were prepared from the high strength ferritic steel, Weldom 960. Along the centre of each plate, a 5 mm deep V-groove was machined with an included angle of 60° , and in each case a single weld bead was subsequently deposited in the machined groove by manual-metal arc welding. On one of the plates the commercial filler alloy OK 75.78 was used, on another the LTTE3 alloy was used, while on the third one the new candidate filler alloy (series B) was employed. In all cases welding was undertaken in the down-hand position and the heat input was maintained between 1.1 and 1.4 kJ/mm. A preheat temperature of 125°C was used and the plates were restrained by clamping during welding.

Macrographs were prepared so that the measured residual stress distributions could be correlated with the different metallurgical zones in each of the welded plates. One 5mm thick slice was removed from the end of each plate by electro-discharge machining (Fig. A.1). Each slice was then ground and polished to a $1 \mu\text{m}$ finish prior to etching in 2% nital for 15 seconds. The macrographs for each weld are shown in Fig. A.2.

It can be seen from Fig. A.2 that the weld bead penetrations are close to 6 mm, equivalent to half the plate thickness. Whilst there are minor variations from one weld to another, the extent of the fusion zone and HAZ in each weld is similar, as the same nominal welding parameters were used in each case. The heat-affected zone (HAZ) reveals two distinct bands. The inner band, which is the darker of the two in the figure, corresponds to the coarse-grained heat-affected zone (CGHAZ), while the outer band is dominated by the fine-grained heat-affected zone (FGHAZ). The fact that the HAZ is quite extensive when compared with the fusion zone (at least in the context of the specimen configuration and welding parameters selected for this study) means that the phase transformations that occur within the HAZ will also have a significant effect on the resulting stress distributions. Full

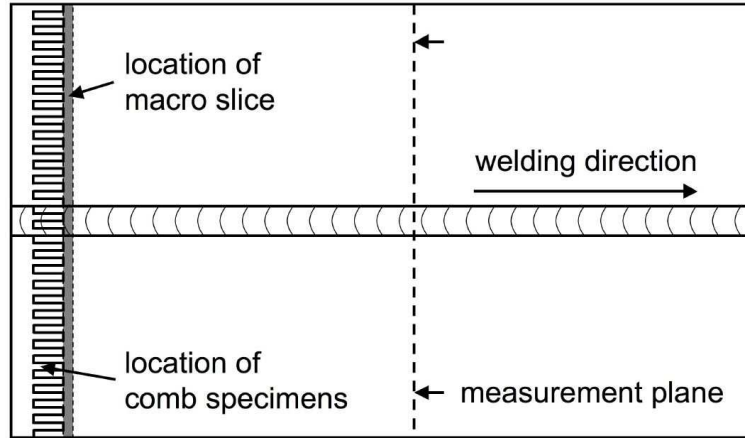
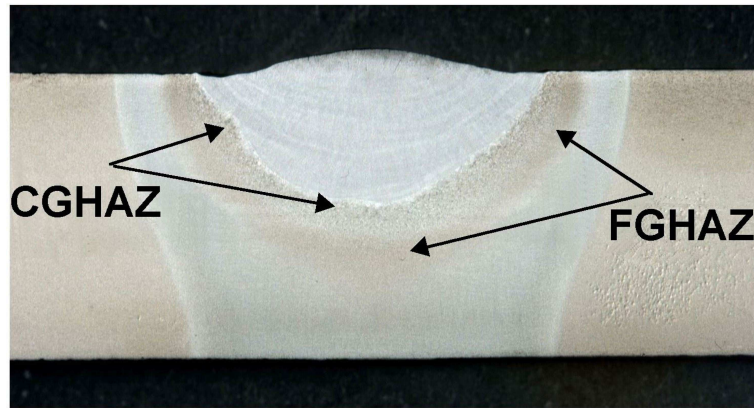


Figure A.1: Schematic representation of welded plate showing location of reference combs, slice extracted for macrograph and location of measurement plane.

austenitisation will occur in the CGHAZ and FGHAZ, and there will also be an intercritical region (ICHAZ) that experiences only partial austenitisation. Of course, the different regions within the HAZ will transform at temperatures that are determined by the composition of the parent material.

A.2.3 Neutron diffraction

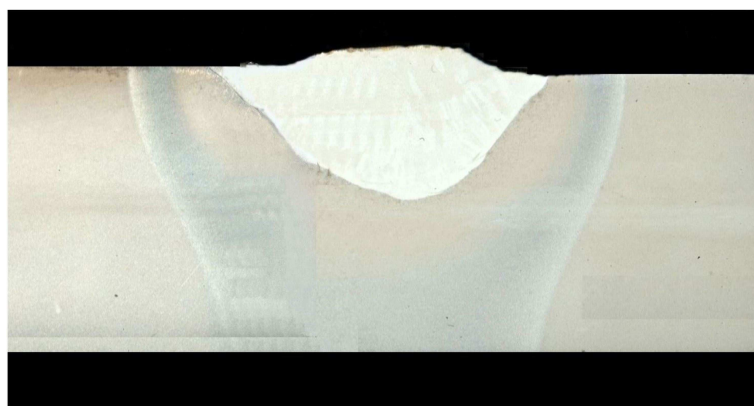
Measurements of the residual stresses in the welded plates were conducted by neutron diffraction on the L3 spectrometer, which is part of the National Research Council of Canada facility at the NRU reactor, Chalk River. Monochromation of the neutron beam was achieved through diffraction from the $\{\bar{1}\bar{1}5\}$ planes of a germanium monochromator crystal at 92° . The wavelength of the neutrons was determined to be $1.5651 \pm 0.0001 \text{ \AA}$ from calibration measurements of the first four diffraction peaks from a nickel standard powder sample. With this wavelength, the $\{112\}$ peaks from the ferritic and martensitic material in the welded plates could be observed at an angle of $2\theta \approx 84^\circ$ which, being close to 90° , provided optimal spatial resolution and



OK75.78



LTTE



Series B

Figure A.2: Macrostructure of the welded joints.

avoided peak asymmetry arising as a result of axial divergence.

Positioning of the sample in the neutron beam was accomplished with an XYZ translation stage attached to a 360° rotational drive. With these drives, the sample could be positioned with an accuracy of 0.1 mm in X, Y and Z and 0.1° in rotational angle. Spatial resolution within the sample was achieved with cadmium slits inserted in the incident and diffracted beam paths. For all of the measurements, the slits were positioned within 20 mm of the sample surface to avoid penumbra effects.

Determination of the full strain tensor at each measurement position requires the measurement of the lattice strain in at least six independent directions. However, the orientation of one or more of the principal axes may be assumed from inspection of the geometry of the component. As is typical for measurements of this type, it was assumed that the principal axes were coincident with the axes of the plate. Whilst it may be reasonable to assume that one of the principal axes lies along the welding direction, the asymmetry of the weld fusion zone may be expected to lead to rotations of the principal axes from the transverse and normal directions in this plane. To test this assumption, additional measurements were made at an intermediate angle in this plane.

Measurements of the lattice strains were made in the plane perpendicular to the direction of the weld across the centre of each plate. For measurements in the transverse and normal directions, the samples were orientated on the translation stage with the welds vertical. Slits 1 mm wide and 10 mm long were employed, providing a gauge volume of $1 \times 1 \times 10$ mm in the sample. The use of these slits presupposes that the strains are invariant over the length of the slits. For the measurement of the longitudinal strains the samples were orientated with the transverse direction vertical and the welds parallel to the scattering vector. For these measurements, slits 1 mm wide and 2 mm long were used.

A.2.4 Determination of stress-free lattice spacing

As the composition of the filler material is different from that of the base metal the lattice spacing is expected to vary at different depths in any welded joint. To eliminate this effect from the measurement of the residual stress, stress-free samples were cut from the weld so that the reference lattice parameters could be determined. The samples were cut by electro-discharge machining from the last 30mm of each welded plate as a series of combs with teeth 2mm by 2mm in section and 20mm long (Fig. A.1). The dimensions of the teeth were chosen to allow the diffraction gauge volume to be fully immersed in the sample. The long direction of the teeth was aligned parallel with the welding direction in order to avoid incomplete stress relaxation as a result of stress gradients in the plane perpendicular to the weld. This also provided maximum spatial resolution of lattice parameter variations in the transverse plane. Combs were extracted from each plate at depths of 1, 3.5, 5, 8.5 and 11mm from the top surface of the plate. Measurements of the lattice parameter (designated as d_o) were made on these samples to a distance of approximately 60 mm from the weld centre-line, beyond which no further variation in lattice parameter was observed.

A.3 Results

A.3.1 Calculations of strains and stresses

The measured diffraction peaks were fitted with a Gaussian function on a constant background. From the Bragg angle, $\theta_{\{112\}}$, determined, the lattice spacings, $d_{\{112\}}$ were obtained from the Bragg equation

$$\lambda = 2d_{\{112\}} \sin \theta_{\{112\}} \quad (\text{A.1})$$

With these lattice spacings, the corresponding strains $\varepsilon_{\{112\}}$ were obtained with reference to the measured stress- free lattice parameter from

$$\varepsilon_{\{112\}} = (d_{\{112\}} - d_o)/d_o \quad (\text{A.2})$$

The measured lattice strain is the resolved component of the strain component, ε_{ij} onto the measurement direction

$$\varepsilon_{\{112\}} = \sum_{\text{all } i,j} \varepsilon_{ij} \alpha_i \alpha_j \quad (\text{A.3})$$

where α_i and α_j are the direction cosines between the measurement direction and the principal axes.

With the principal strains acquired by matrix diagonalisation the stresses may be obtained from

$$\sigma_i = \frac{E_{\{112\}}}{(1 + \nu_{\{112\}})} \varepsilon_i + \frac{\nu_{\{112\}} E_{\{112\}}}{(1 + \nu_{\{112\}})(1 - 2\nu_{\{112\}})} \sum_{\text{all } j} \varepsilon_j \quad (\text{A.4})$$

where σ_i is the principal stress in the i direction and $E_{\{112\}}$ and $\nu_{\{112\}}$ are the plane specific Young's modulus and Poisson's ratio.

A.3.2 Results and discussion

Figs A.3 to A.8 show the results of the residual stress analysis in three welded joints made using three different filler metals. There is a general trend observed in all these plots, that is, the value of the stress is lowest in the fusion zone, it reaches its peak at the end of the HAZ and then it decreases again. The reason behind this is, the fusion zone or the HAZ undergoes phase transformation and as a result there is a transformation strain. This reduces the thermal contraction stress in this region. However outside the HAZ there is very little or no thermal contraction nor any transformation strain due

to phase transformation so the residual stress remains close to zero. At the border of these two zones the residual stress is maximum due to strain misfit.

It is clear that the nature of the residual stress in welded joints made with OK75.78 filler metal is quite different from that of weld joints made with low transformation temperature filler metals LTTE3 and Series-B.

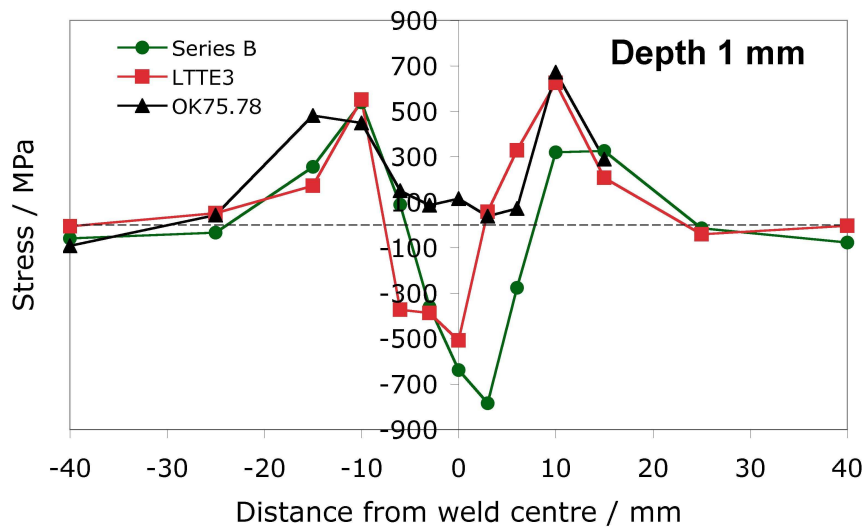


Figure A.3: Variation of residual stress in the longitudinal direction in welded joints made at a depth of 1 mm from the surface.

It can be seen from Figs A.3 to A.8 that for OK75.78 filler metal, the residual stress remains almost constant as the depth varies although substantial change occurs in the lateral direction. The stress is low at the centre-line region but increases rapidly and reaches its peak at the boundary of the HAZ. This filler metal is having a transformation temperature which is much higher than the room temperature. So the transformation exhaust long before the room temperature is reached and as a result the transformation strain can not be utilised fully to reduce the tensile residual stress.

For Series-B and LTTE3 filler metals, however, the nature of residual stress within the fusion zone is very different (Figs A.3 to A.8). As

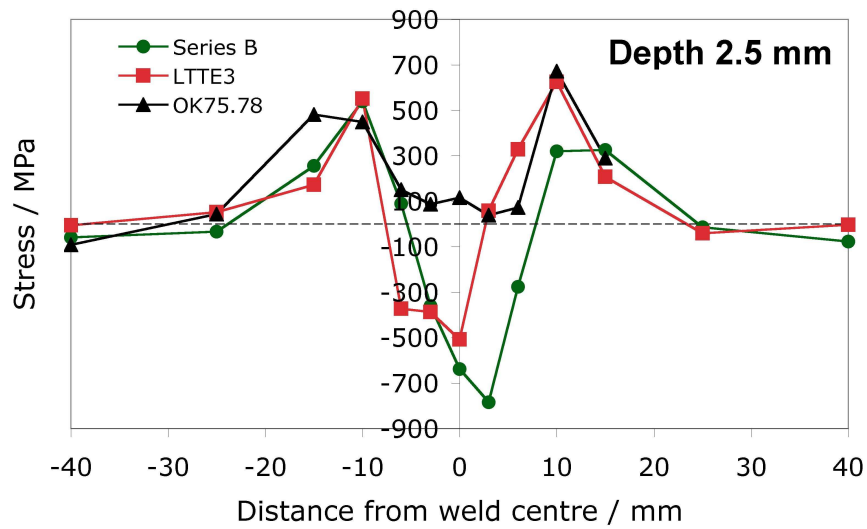


Figure A.4: Variation of residual stress in the longitudinal direction in welded joints made at a depth of 2.5 mm from the surface.

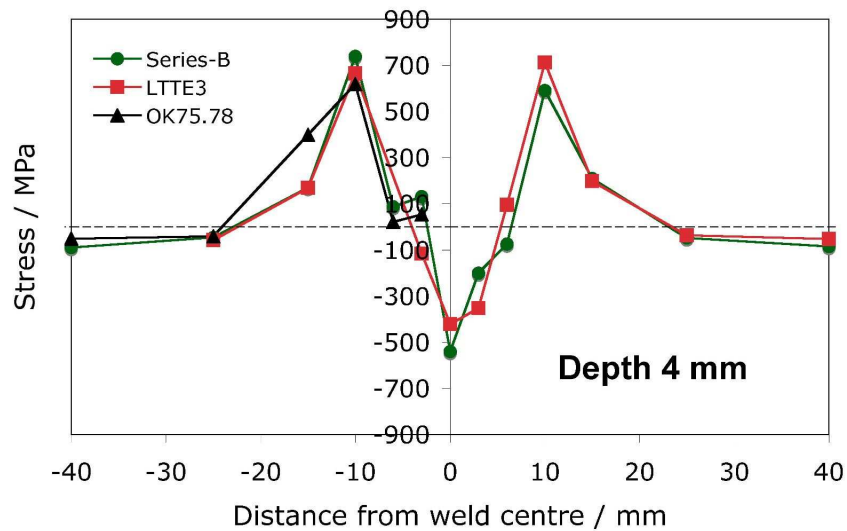


Figure A.5: Variation of residual stress in the longitudinal direction in welded joints made at a depth of 4 mm from the surface.

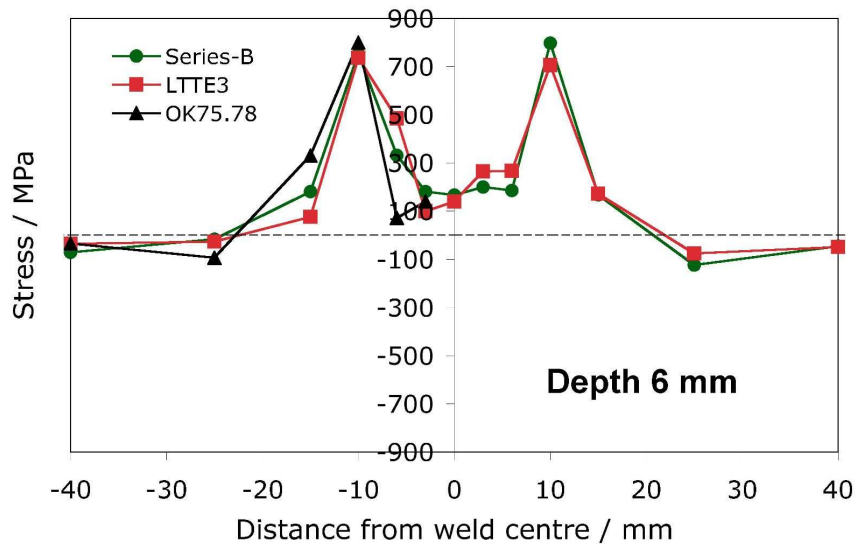


Figure A.6: Variation of residual stress in the longitudinal direction in welded joints made at a depth of 6 mm from the surface.

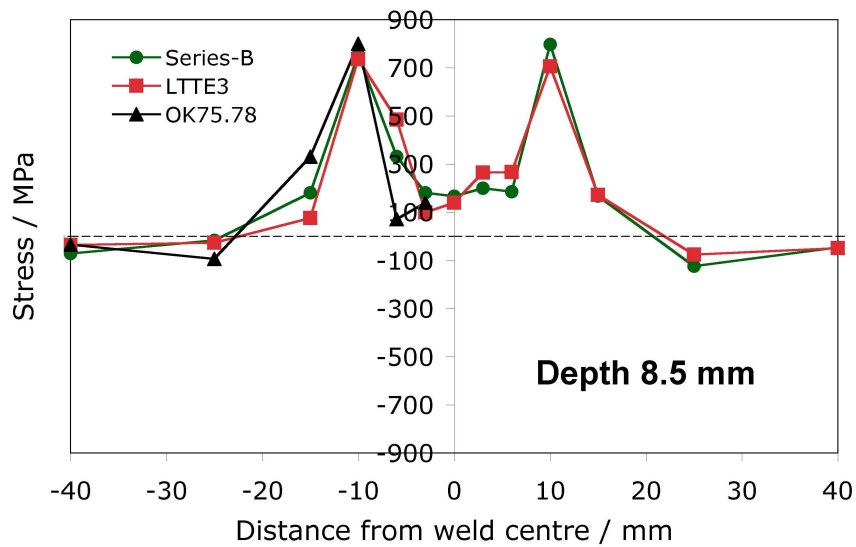


Figure A.7: Variation of residual stress in the longitudinal direction in welded joints made at a depth of 8.5 mm from the surface.

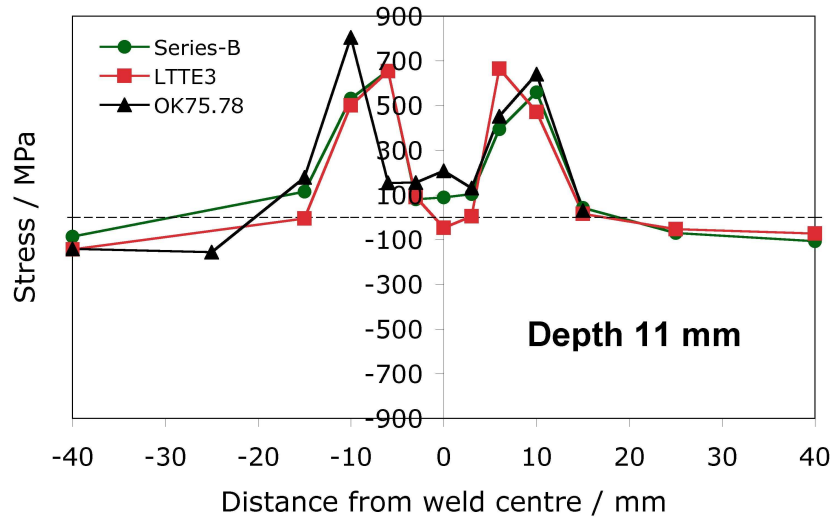


Figure A.8: Variation of residual stress in the longitudinal direction in welded joints made at a depth of 11 mm from the surface.

these alloys are having far low transformation temperatures they suppress the harmful tensile residual stress to a much higher degree and as a result the stress in the fusion zone becomes compressive. But the nature of the stress changes with the depth unlike in the case of weld made with OK75.78. The compressive stress is observed at lower depths (in the fusion zone, A.3 to A.5), however outside fusion zone the stress becomes tensile again (A.6 to A.8). This is because below 5/6 mm from the surface it is the base metal that cools after welding which has a much higher transformation temperature than the filler metal. However, even for these low transformation temperature filler metals stress in the HAZ remains tensile, peak value of which might reach more than 700 MPa which is just about 100 MPa less than that for OK75.78.

It is evident from these results that the transformation temperature of the filler metal does not have any significant effect on the residual stress development outside the fusion zone. Although the harmful tensile residual

stress is somewhat less in the case of a low transformation temperature filler metal. However the newly developed filler metal could be more useful for multi-pass welding. In such joints, the characteristics of the filler metal may take on increased significance. Firstly, with more substantial substrates the extent of the HAZ for each weld pass reduces. Perhaps more importantly though, the HAZ for many of the weld passes will be located within previously deposited weld metal, and thus will have a transformation temperature more closely aligned with the filler metal than that of the substrate material. Whether or not this is likely to translate to increased reductions in the peak tensile residual stresses is still unclear.

There could be another situation in which solid state phase transformations may provide an avenue for significant reductions in welding residual stresses, this is during welding of components made from austenitic stainless steels. If, for example, it were possible to use a ferritic-martensitic low transformation temperature filler metal for austenitic alloys, then the associated benefits for residual stresses would not be masked by any solid-state transformations occurring within the HAZ.

A.4 Summary and future work

1. It has been shown that for all filler metals where transformation takes place during welding residual stress decreases. For low transformation temperature filler rods, residual stress in the fusion zone could be compressive.
2. Although low transformation temperature of the filler metals reduces the residual stress in HAZ but the effect is not as significant as in the fusion zone.
3. The transformation strain might be more effectively utilised in case

of multipass welds as in this case the HAZ for a particular pass will reside within the fusion zone of the previous pass. However further experimental evidence is required in this aspect.

4. In case of a base metal where there is no transformation taking place during welding, transformation strain can be better utilised. This is because in such cases the HAZ will not mask the transformation behaviour of the fusion zone.
5. The modelling of residual stress development in ferritic alloys would require a coupled stress and heat-transfer model with a phase transformation model.

Appendix B

Computer programs

These programs can be obtained from

<http://www.msm.cam.ac.uk/map/mapmain.html>

B.1 Subroutine MAP_STEEL_BAIN_STRAIN

- (a) Provenance of code.
- (b) Purpose of code.
- (c) Specification.
- (d) Description of subroutine's operation.
- (e) References.
- (f) Parameter descriptions.
- (g) Error indicators.
- (h) Specification.
- (i) Accuracy estimate.
- (j) Any additional information.

- (k) Example of code
- (l) Auxiliary subroutines required.
- (m) Keywords.
- (n) Download source code.

Provenance of Source Code

Saurabh Kundu and H. K. D. H. Bhadeshia

Materials Science and Metallurgy, University of Cambridge, U. K.

E-mail: sk459@cam.ac.uk

Added to MAP: March, 2007.

Purpose

Calculation of habit plane and displacement direction during displacive transformation. It also calculates the orientation relationship matrix between gamma and the ferrite phase.

Specification

Language: FORTRAN

Description

This program takes the lattice parameters of ferrite and austenite as the inputs. It also takes the correspondence matrix, lattice invariant plane and lattice invariant directions as inputs. It follows the phenomenological theory of martensite crystallography and calculates the crystallographic set for any transformation.

Inputs when running the program

PUT THE AUSTENITE LATTICE PARAMETER:

3.619092

PUT THE FERRITE LATTICE PARAMETER:

2.882

Name

bain_strain.for. This is a source code of this program. For the execution, it needs to be compiled.

Compile example : `g77 bain_strain.for -o name.out`

References

H. K. D. H. Bhadeshia, Worked examples in the geometry of crystals , University of Cambridge.

Parameters

HABIT: double precision array of dimension 24×3 , Matrix that stores 24 habit planes.

DIRECTION: Double precision array of dimension 24×3 . Matrix that stores 24 displacement directions for 24 variants of martensite.

GM_J_AL: Double precision array of dimension 72×3 . It contains 24 matrix representing orientation relationship between martensite and austenite, following Bowles and MacKenzie notation can be written as $(\gamma \text{ J } \alpha)$.

AL_J_GM: Double precision array of dimension 72×3 . It contains 24 matrix representing orientation relationship between martensite and austenite, following Bowles and MacKenzie notation can be written as $(\alpha \text{ J } \gamma)$.

CORRSP_MAT: Double precision array of dimension 3×3 . This is the correspondence matrix.

BAIN: Double precision array of dimension 3×3 . Matrix represents the bain strain.

INV_LN_STRN: Double precision array of dimension 3×3 . This matrix represents the invariant line strain.

ROT_MAT: Double precision array of dimension 3×3 . This matrix represents rigid body rotation.

LAT_INV_PL: Double precision array of dimension 3×1 . Stores the indices of the plane for lattice invariant deformation.

LAT_INV_DI: Double precision array of dimension 1×3 . Stores the indices of the direction for lattice invariant deformation.

Error Indicators

None.

Accuracy

No information.

Further Comments

None.

Example

None.

Auxiliary Routines

No auxiliary routines.

Keywords

Martensite crystallography, martensite, steels.

Download

Download source code.

B.2 Subroutine MAP_STEEL_TRANS_PLAST

- (a) Provenance of code.
- (b) Purpose of code.
- (c) Specification.
- (d) Description of subroutine's operation.
- (e) References.
- (f) Parameter descriptions.
- (g) Error indicators.
- (h) Specification.
- (i) Accuracy estimate.
- (j) Any additional information.
- (k) Example of code
- (l) Auxiliary subroutines required.
- (m) Keywords.
- (n) Download source code.

Provenance of Source Code

Saurabh Kundu and H. K. D. H. Bhadeshia.

Materials Science and Metallurgy, University of Cambridge, U. K.

E-mail: sk459@cam.ac.uk

Added to MAP: March, 2007.

Purpose

Calculation of transformation strain when austenite transforms into martensite/bainite.

Specification

Language: FORTRAN

Description

This program has the inputs consisting of the habit planes, displacement direction and the crystallographic orientation relationship between various gamma grains.

- (a) It assumes three unit vectors in the principle directions of the applied stress.
- (b) It calculates the interaction energies for each variant in every grain and rank all the variants according to the interaction energies.
- (c) Assuming n number (n vary from 1 to 24) of variants forming in each grain it allows the unit vectors to get deformed by the shape deformation matrix of each variant.
- (d) The final vector is calculated.
- (e) The ratio between the final and initial length of the vectors give the strain.
- (f) User can change the number of grains and amount of martensite / bainite.

Inputs when running the program

WRITE THE NUMBER OF GRAINS:

500

FRACTION OF MARTENSITE/BAINITE:

0.63

INITIAL TEXTURE:

0=RANDOM

1=COPPER

2=BRASS

3=GOSS

4=CUBE

5={110}<111>

6=MIXTURE

0 FIRST ELEMENT OF THE STRESS TENSOR:

200.0

Name

trans_plast_tensor.for. This is a source code of this program. For the execution, it needs to be compiled.

compile example : `g77 trans_plast_tensor.for -o name.out`

References

S. Kundu, *PhD Thesis*, University of Cambridge.

Parameters

HABIT: double precision array of dimension 24×3 , Matrix that stores 24 habit planes.

DIRECTION: Double precision array of dimension 24×3 . Matrix that stores 24 displacement directions for 24 variants of martensite.

GM_J_AL: Double precision array of dimension 72×3 . It contains 24 matrix representing orientation relationship between martensite and austenite, following Bowles and MacKenzie notation can be written as $(\gamma \text{ J } \alpha)$.

AL_J_GM: Double precision array of dimension 72×3 . It contains 24 matrix representing orientation relationship between martensite and austenite, following Bowles and MacKenzie notation can be written as $(\alpha \text{ J } \gamma)$.

DEF_MAT: Double precision array of dimension 3×3 . This matrix stores stress tensor of the applied stress in the crystal axis.

STRESS_TENSOR: Double precision array of dimension 3×3 . Matrix represents the stress tensor in the sample axis.

TRANS_MATRIX: Double precision array of dimension 3×3 . Rotational matrix representing the orientation relationship between any austenite grain with the sample axis.

SH, VOL, TOT : Double precision. The shear, volume and total strain associated with any martensite/bainite variant.

Error Indicators

None.

Accuracy

No information.

Further Comments

None.

Example

None.

Auxiliary Routines

No auxiliary routines.

Keywords

Transformation strain, martensite, steels, crystallography.

Download

Download source code.

B.3 Subroutine MAP_STEEL_TEXTURE

- (a) Provenance of code.
- (b) Purpose of code.
- (c) Specification.
- (d) Description of subroutine's operation.
- (e) References.
- (f) Parameter descriptions.
- (g) Error indicators.
- (h) Specification.
- (i) Accuracy estimate.
- (j) Any additional information.
- (k) Example of code
- (l) Auxiliary subroutines required.
- (m) Keywords.
- (n) Download source code.

Provenance of Source Code

Saurabh Kundu and H. K. D. H. Bhadeshia.

Materials Science and Metallurgy, University of Cambridge, U. K.

E-mail: sk459@cam.ac.uk

Added to MAP: March, 2007.

Purpose

Calculation of the crystallographic texture obtained when austenite transforms into martensite. The austenite itself can be textured.

Specification

Language: FORTRAN

Description

This program has the inputs consisting of the habit planes, displacement direction and the crystallographic orientation (γ J α).

- (a) It first calculates the angle theta (between applied stress and habit plane normal and beta (between the maximum shear stress and the shear stress component resolved on the habit plane).
- (b) Then it calculates the mechanical free energy available for each martensite variant.
- (c) It also measures the angle between trace of habit plane on the plane of observations with the applied stress direction. It must be noted that by default the sample X-Y plane is taken to be the plane of observations.
- (d) The plot is made with respect to the principle sample axis which are taken as (100),(010) and (001).
- (e) This program plots the martensite pole figure and also the pole figure for the habit planes active.
- (f) User can plot as many variants as desired.

Inputs when running the program

IF AUSTENITE PUT 0 IF FERRITE PUT 1:

1

WHAT IS THE STARTING TEXTURE OF AUSTENITE:

0=RANDOM

1=COPPER

2=BRASS

3=GOSS

4=CUBE

5={110}<111>

6=MIXTURE

3

HOW MANY VARIANTS WORKING?

8

FIRST ELEMENT OF THE STRESS TENSOR:

200.0

FOR (100) POLE FIG PUT 100 :

FOR (111) POLE FIG PUT 111 :

FOR (110) POLE FIG PUT 110 :

100

HOW MANY GRAINS?

500

Name

crystal_habit_poly.for. This is a source code of this program. For the execution, it needs to be compiled.

Compile example : `g77 crystal_habit_poly.for -o name.out`

References

S. Kundu and H.K.D.H. Bhadeshia, *Transformation Texture in Deformed Stainless Steel*, Scripta Materialia, 55 (2006), 779-781.

Parameters

HABIT: double precision array of dimension 24×3 , Matrix that stores 24 habit planes.

DIRECTION: Double precision array of dimension 24×3 . Matrix that stores 24 displacement directions for 24 variants of martensite.

GM_J_AL: Double precision array of dimension 72×3 . It contains 24 matrix representing orientation relationship between martensite and austenite, following Bowles and MacKenzie notation can be written as $(\gamma \text{ J } \alpha)$.

AL_J_GM: Double precision array of dimension 72×3 . It contains 24 matrix representing orientation relationship between martensite and austenite, following Bowles and MacKenzie notation can be written as $(\alpha \text{ J } \gamma)$.

DEF_MAT: Double precision array of dimension 3×3 . This matrix stores stress tensor of the applied stress in the crystal axis.

AL: Double precision array of dimension 30×3 . It stores all the plane indices for plotting pole figure.

STRESS_TENSOR: Double precision array of dimension 3×3 . Matrix represents the stress tensor in the sample axis.

TRANS_MATRIX: Double precision array of dimension 3×3 . Rotational matrix representing the orientation relationship between any austenite grain with the sample axis.

X_ST, Y_ST: Double precision. X and Y coordinate of any point in the pole figure.

Error Indicators

None.

Accuracy

No information.

Further Comments

None.

Example

None.

Auxiliary Routines

No auxiliary routines.

Keywords

Transformation texture, martensite, stainless steels, crystallography.

Download

Download source code.

Bibliography

- [1] H. K. D. H. Bhadeshia. *Bainite in Steels, 2nd edition*. Institute of Materials, London, 2001.
- [2] A. Ohta, K. Matsuoka, N. T. Nguyen, Y. Maeda, and N. Suzuki. *American Welding Journal*, 82:s78–s83, 2003.
- [3] W. K. C. Jones and P. J. Alberry. *Materials Science and Technology*, 11:557–566, 1977.
- [4] H. K. D. H. Bhadeshia. *Materials Science and Engineering A*, 378:34–39, 2005.
- [5] H. N. Han, C. G. Lee, C.-S. Oh, T.-H. Lee, and S.-J. Kim. *Acta Materialia*, 2004:5203–5214.
- [6] H. N. Han and D. W. Suh. *Acta Materialia*, 51:4908–4917, 2003.
- [7] M. Humbert, B. Petit, B. Bolle, and N. Gey. *Materials Science and Engineering A*, doi:10.1016/j.msea.2006.11.12, 2007.
- [8] N. Gey, B. Patit, and M. Humbert. *Metallurgical and Materials Transactions A*, 36:3291–3299, 2005.
- [9] H. Miyaji, M. Nobuki, N. Sakuma, T. Mitsui, H. Nakajima, and E. Furubayashi. In I. Tamura, editor, *Proceedings of International Conference on ‘Physical metallurgy of thermomechanical*

- processing of steels and other metals*', volume 2, pages 815–822. The Iron and Steel Institute of Japan, 1988.
- [10] J. S. Bowles and J. K. MacKenzie. *Acta Metallurgica*, 2:129–137, 1954.
- [11] J. K. MacKenzie and J. S. Bowles. *Acta Metallurgica*, 2:138–147, 1954.
- [12] J. R. Patel and M. Cohen. Criterion for the action of applied stress in the martensitic transformation. *Acta Metallurgica*, 1:531–538, 1953.
- [13] H. K. D. H. Bhadeshia. *Geometry of Crystals*. 2nd edition, Institute of Materials, 2001.
- [14] J. W. Christian. Deformation by moving interfaces. *Metallurgical Transactions A*, 13:509–538, 1982.
- [15] P. H. Shipway and H. K. D. H. Bhadeshia. *Materials Science and Engineering A*, A201:143–149, 1995.
- [16] A. Matsuzaki, H. K. D. H. Bhadeshia, and H. Harada. *Acta Metallurgica and Materialia*, 42:1081–1090, 1994.
- [17] L. Kestens, R. Decocker, and R. Petrov. *Materials Science Forum*, 408–412:1173–1178, 2002.
- [18] L. Kestens, R. Petrov, and Y. Houbaert. *ISIJ International*, 43:1444–1452, 2003.
- [19] B. Brückner and G. Gottstein. *ISIJ International*, 41:468–477, 2001.
- [20] P. Bate and B. Hutchinson. *Acta Materialia*, 48:3183–3192, 2000.

- [21] M. S. Wechsler, D. S. Lieberman, and T. A. Read. *Trans. AIME Journal of Metals*, 197:1503–1515, 1953.
- [22] G. Nolze. *Zeitschrift für Metallkunde*, 95:744–755, 2004.
- [23] J. W. Christian and A. G. Crocker. *Dislocations in Solids*, chapter 3, page 165. North Holland, 1980.
- [24] B. D. Cullity and S. R. Stock. *Elements of X-ray diffraction*. Prentice-Hall, 2001.
- [25] R. K. Ray and J. J. Jonas. *International Materials Reviews*, 35:1–37, 1990.
- [26] J. C. Bokros and E. R. Parker. *Acta Metallurgica*, 11:1291–1301, 1963.
- [27] T. N. Durlu and J. W. Christian. *Acta Metallurgica*, 27:663–666, 1979.
- [28] S. Chatterjee, H. S. Wang, J. R. Yang, and H. K. D. H. Bhadeshia. *Materials Science and Technology*, 22:641–644, 2006.
- [29] Y. Higo, F. Lecroisey, and T. Mori. *Acta Metallurgica*, 22:313–323, 1974.
- [30] A. J. Bogers and W. G. Burgers. *Acta Metallurgica*, 12:255–261, 1964.
- [31] M. Kato and T. Mori. *Acta Metallurgica*, 24:853–860, 1976.
- [32] M. Kato and T. Mori. *Acta Metallurgica*, 25:951–956, 1977.
- [33] E. Furubayashi. *Tetsu-to-Hagane*, 71:1355–1366, 1985.

- [34] P. C. Maxwell, A. Goldberg, and J. C. Shyne. *Metallurgical Transactions*, 5:1305–1318, 1974.
- [35] F. Lecroisey and A. Pineau. *Metallurgical Transactions*, 3:387–396, 1972.
- [36] I. Tamura, T. Maki, and H. Hato. *Transactions of Japan Iron and Steel Institute*, 10:163–172, 1970.
- [37] K. Hase, C. Garcia Mateo, and H. K. D. H. Bhadeshia. *Materials Science and Technology*, 20:1499–1505, 2004.
- [38] T. Maki, S. Shimooka, M. Umemoto, and I. Tamura. *Transaction of Japan Iron and Steel Institute*, 13:400–, 1972.
- [39] G. Ghosh and V. Raghavan. *Materials Science and Engineering A*, 80:65–74, 1986.
- [40] S. B. Singh. PhD thesis, University of Cambridge, 1998.
- [41] T. N. Durlu. *Acta Metallurgica*, 26:1855–1861, 1978.
- [42] M. Umemoto and I. Tamura. In J. M. T. Gray, T. K0, Z. Shouhuma, W Boarong, and X. Xishan, editors, *HSLA Steels: Metallurgy and Applications*, pages 373–382, 1986.
- [43] J. Lu. *ASM Handbook*, pages 11–26. ASM International, Materials Park, Ohio, USA, 2002.
- [44] P. J. Withers and H. K. D. H. Bhadeshia. *Materials Science and Technology*, 17:355–365, 2001.
- [45] P. J. Withers and H. K. D. H. Bhadeshia. *Materials Science and Technology*, 17:366–375, 2001.
- [46] C. Laird. *Metallurgical Transactions A*, 8A:851–860, 1977.

- [47] H. R. Sander and M. Hempel. *Arch. Eisenhuettenw*, 23:299–320, 1952.
- [48] A. Ohta, N. Suzuki, Y. Maeda, K. Hiraoka, and T. Nakamura. *International Journal of Fatigue*, 21:s113–s118, 1999.
- [49] A. Ohta, N. Suzuki, and Y. Maeda. *Properties of Complex Inorganic Solids 2*, pages 401–408. Kluwer Academic/Plenum Publishers, 2000.
- [50] J. Eckerlid, T. Nilsson, and L. Karlsson. *Science and Technology of Welding and Joining*, 8:353–359, 2003.
- [51] D. P. Koistinen and R. E. Marburger. *Acta Metallurgica*, 7:59–60, 1959.
- [52] T. G. Digges. *Transaction of American Society for Metals*, 28:575–, 1940.
- [53] A. B. Ggreninger. *Transaction of American Society for Metals*, 30:1–, 1942.
- [54] W. J. Harris and M. Cohen. *Transactions of American Institute of Mining (Metallurgical) Engineers.*, 180:447–470, 1949.
- [55] C. L. Magee. The nucleation of martensite. In H. I. Aaronson and V. F. Zackay, editors, *Phase Transformations*, pages 115–156. ASM, Metals Park, Ohio, USA, 1970.
- [56] R. Brook, A. R. Entwisle, and E. F. Ibrahim. *Journal of the Iron Steel Institute*, 195:292–298, 1960.
- [57] S. M. C. van Bohemen, J. Siestma, M. J. M. Haermans, and I. M. Richardson. *Acta Materialia*, 51:4183–4196, 2003.

- [58] G. B. Olson and M. Cohen. *Acta Metallurgica*, 6A:4183–4196, 1975.
- [59] A. Ohta, O. Watanabe, K. Matsuoka, C. Shiga, S. Nishijima, Y. Maeda, N. Suzuki, and T. Kubo. *Welding in the World*, 43:38–42, 1999.
- [60] T. Ko and S. A. Cottrell. *Journal of the Iron and Steel Institute*, 172:307–313, 1952.
- [61] E. Swallow and H. K. D. H Bhadeshia. *Materials Science and Technology*, 12:121–125, 1996.
- [62] S. P. Timoshenko and J. N. Goodier. *Theory of Elasticity*. McGraw Hill International Book Company, London, 1982.
- [63] H. J. Bunge. *Mathematische Methoden der Texturanalyse. English*. Butterworth, London, 1982.
- [64] I. L. Dilamore and W. T. Roberts. *Metallurgical Reviews*, 10:271–380, 1965.
- [65] T. Tanaka. *International Metals Reviews*, 4:185–212, 1981.
- [66] D. Raabe. Overview of basic types of hot rolling textures of steels. *Steel Research International*, 74:327–337, 2003.
- [67] H. K. D. H. Bhadeshia, S. A. David, J. M. Vitek, and R. W. Reed. *Materials Science and Technology*, 7:686–698, 1991.
- [68] E.S. Davenport and E.C. Bain. *Trans. Met Soc. AIME*, 90:117–154, 1930.
- [69] S. Kundu and H. K. D. H. Bhadeshia. *Scripta Materialia*, 55:779–781, 2006.

- [70] M. X. Zhang and P. M. Kelly. *Materials Science and Engineering A*, A438–440:272–275, 2006.
- [71] D. P. Dunne and C. M. Wayman. *Acta Metallurgica*, 19:425–438, 1971.
- [72] H. M. Ledbetter and C. M. Wayman. *Materials Science and Engineering*, 7:151–157, 1971.
- [73] D. P. Dunne and C. M. Wayman. *Metallurgical Transactions*, 2:2327–2341, 1971.
- [74] V. Randle and O. Engler. *Introduction to Texture Analysis: Macrotecture, Microtexture and Orientation Mapping*. Gordon and Breach Science Publisher, 2000.
- [75] D. J. Dingley and M. M. Nowell. *Microchimica Acta*, 147:157–165, 2004.
- [76] F. J. Humphreys. *Scripta Materialia*, 51:771–776, 2004.
- [77] H. K. D. H. Bhadeshia and D. V. Edmonds. *Metallurgical Transactions A*, 10A:895–907, 1979.
- [78] R. Lagneborg. *Acta Metallurgica*, 12:823–843, 1964.
- [79] D. J. Dyson and B. Holmes. *Journal of the Iron and Steel Institute*, 208:469–474, 1970.
- [80] M. Humbert, B. Gardiola, C. Esling, G. Flemming, and K.E. Hensger. *Materials Science Forum*, 408:445–450, 2002.
- [81] A. Mukhopadhyay, I. C. Howard, and C. M. Sellars. *Materials Science and Technology*, 20:1123–1133, 2004.

- [82] A. Mukhopadhyay, R. L. Higginson, I. C. Howard, and C. M. Sellars. *Materials Science and Technology*, 23:29–37, 2007.
- [83] W. C. Liu, C. S. Man, D. Raabe, and J. G. Morris. *Scripta Materialia*, 53:1273–1277, 2005.
- [84] M. P. Phaniraj, B. B. Behera, and A. K. Lahiri. *Journal of Materials Processing Technology*, 170:323–335, 2005.
- [85] Y. D. Wang, R. Lin Peng, X. L. Wang, and R. L. McGreevy. *Acta Materialia*, 50:1717–1734, 2002.
- [86] B. Petit, N. Gey, M. Cherkaoui, B. Bolle, and M. Humbert. *International Journal of Plasticity*, 23:323–341, 2007.
- [87] P. M. Kelly. *Acta Metallurgica*, 13:635–646, 1965.
- [88] M. Murugananth. *Design of welding alloys creep and toughness*. PhD thesis, University of Cambridge, 2002.
- [89] Materials Algorithms Project (MAP), <http://www.msm.cam.ac.uk/map/>, University of Cambridge, Cambridge, UK.
- [90] G. Ghosh and G. B. Olson. *Acta Metallurgica et Materialia*, 42:3361–3370, 1994.
- [91] <http://www.thomas-sourmail.org/martensite.html>.
- [92] W. X. Wang, L. X. Huo, Y. F. Zhang, D. P. Wang, and H. Y. Jing. *Journal of Materials Science and Technology*, 18:527–531, 2002.
- [93] H. Lixing, W. Dongpo, W. Wenxian, and Z. Yufeng. *Welding in the World*, 48:34–39, 2004.

- [94] H. K. D. H. Bhadeshia and R. W. K. Honeycombe. *Steels: Microstructure and Properties, 3rd edition*. Butterworth-Heinemann, London, 2006.
- [95] M. Lord. *High strength steel welds*. PhD thesis, University of Cambridge, 1999.
- [96] H. R. Wenk. *Texture and Anisotropy*, pages 127–177. Cambridge University Press, 1998.
- [97] A. P. Hammersley. FIT2D: An introduction and overview. ESRF Internal Report ESRF97HA02T, ESRF, 1997.
- [98] A. P. Hammersley. FIT2D v9.129 reference manual v3.1. ESRF Internal Report ESRF98HA01T, ESRF, 1998.
- [99] A. P. Hammersley, S. O. Svensson, A. Thompson, H. Graafsma, Å. Kvik, and J. P. Moy. *Review of Scientific Instruments*, 66(SRI-94):2729–2733, 1995.
- [100] A. P. Hammersley, K. Brown, W. Burmeister, L. Claustre, A. Gonzalez, S. McSweeney, E. Mitchell, J. P. Moy, S. O. Svensson, and A. Thompson. *Journal of Synchrotron Radiation*, 4:67–77, 1997.
- [101] S. Grigull. *Textures and Microstructures*, 35:153–162, 2003.